NAVAL POSTGRADUATE SCHOOL

MONTEREY, CALIFORNIA

DISSERTATION

SCATTERING OF LOW-FREQUENCY SOUND BY COMPACT OBJECTS IN UNDERWATER WAVEGUIDES

by

Alexander B. Baynes

June 2018

Dissertation Supervisor: Oleg A. Godin

THIS PAGE INTENTIONALLY LEFT BLANK

REPORT DOCUMENTATION PAGE	*Form Approved OMB No. 0704-0188*

1. AGENCY USE ONLY *(Leave blank)*	**2. REPORT DATE** June 2018	**3. REPORT TYPE AND DATES COVERED** Dissertation

4. TITLE AND SUBTITLE SCATTERING OF LOW-FREQUENCY SOUND BY COMPACT OBJECTS IN UNDERWATER WAVEGUIDES	**5. FUNDING NUMBERS** N00014-17-WX-00773
6. AUTHOR(S) Alexander B. Baynes	
7. PERFORMING ORGANIZATION NAME(S) AND ADDRESS(ES) Naval Postgraduate School Monterey, CA 93943-5000	**8. PERFORMING ORGANIZATION REPORT NUMBER**
9. SPONSORING / MONITORING AGENCY NAME(S) AND ADDRESS(ES) Ocean Acoustics Program, ONR, Arlington, VA 22203	**10. SPONSORING / MONITORING AGENCY REPORT NUMBER**

11. SUPPLEMENTARY NOTES The views expressed in this thesis are those of the author and do not reflect the official policy or position of the Department of Defense or the U.S. Government.

12a. DISTRIBUTION / AVAILABILITY STATEMENT Approved for public release. Distribution is unlimited.	**12b. DISTRIBUTION CODE** A

13. ABSTRACT (maximum 200 words)

This dissertation considers the two-dimensional problem of the scattering of a monochromatic cylindrical wave by an infinite cylinder embedded in a homogeneous fluid. The exact solution is expressed as an infinite series of cylindrical functions with complex amplitudes determined by the acoustic boundary conditions at the surface of the cylinder. New closed-form uniform asymptotic solutions for soft, hard, impedance, fluid, and solid cylinders are derived for the scattered field when the radius of the cylinder is small compared to wavelength; i.e., the Rayleigh scattering regime. The scattered wave approximation is valid for arbitrary source and observation point positions outside the scatterer. The approximate solution is expressed as the sum of fields due to three linear image sources, which allows physical insight into the scattering physics and suggests analytic solutions to various multiple-scattering problems. When a target is located close to the ocean surface or another reflecting boundary, reflections of the incident and single-scattered waves from the boundary lead to multiple scattering from the target, with the target being insonified by virtual sources. The virtual source concept and the derived asymptotics are employed to develop an analytic and numerically efficient model for wave scattering by a target near an interface.

14. SUBJECT TERMS Rayleigh scattering, image source solutions, asymptotic theories, diffraction, multiple scattering	**15. NUMBER OF PAGES** 147
	16. PRICE CODE

17. SECURITY CLASSIFICATION OF REPORT Unclassified	**18. SECURITY CLASSIFICATION OF THIS PAGE** Unclassified	**19. SECURITY CLASSIFICATION OF ABSTRACT** Unclassified	**20. LIMITATION OF ABSTRACT** UU

NSN 7540-01-280-5500 Standard Form 298 (Rev. 2-89) Prescribed by ANSI Std. 239-18

THIS PAGE INTENTIONALLY LEFT BLANK

Approved for public release. Distribution is unlimited.

SCATTERING OF LOW-FREQUENCY SOUND BY COMPACT OBJECTS IN UNDERWATER WAVEGUIDES

Alexander B. Baynes
Lieutenant Commander, United States Navy
BS, Cornell University, 2004
MS, Naval Postgraduate School, 2010

Submitted in partial fulfillment of the
requirements for the degree of

DOCTOR OF PHILOSOPHY IN APPLIED PHYSICS

from the

NAVAL POSTGRADUATE SCHOOL
June 2018

Approved by:
Oleg A. Godin
Department of Physics
Dissertation Supervisor

Dragoslav Grbovic
Department of Physics

James H. Luscombe
Department of Physics

Clyde L. Scandrett
Undersea Warfare Academic Group

Kevin B. Smith
Department of Physics

Approved by: Kevin B. Smith, Chair, Department of Physics

Douglas Moses, Vice Provost of Academic Affairs

THIS PAGE INTENTIONALLY LEFT BLANK

ABSTRACT

This dissertation considers the two-dimensional problem of the scattering of a monochromatic cylindrical wave by an infinite cylinder embedded in a homogeneous fluid. The exact solution is expressed as an infinite series of cylindrical functions with complex amplitudes determined by the acoustic boundary conditions at the surface of the cylinder. New closed-form uniform asymptotic solutions for soft, hard, impedance, fluid, and solid cylinders are derived for the scattered field when the radius of the cylinder is small compared to wavelength; i.e., the Rayleigh scattering regime. The scattered wave approximation is valid for arbitrary source and observation point positions outside the scatterer. The approximate solution is expressed as the sum of fields due to three linear image sources, which allows physical insight into the scattering physics and suggests analytic solutions to various multiple-scattering problems. When a target is located close to the ocean surface or another reflecting boundary, reflections of the incident and single-scattered waves from the boundary lead to multiple scattering from the target, with the target being insonified by virtual sources. The virtual source concept and the derived asymptotics are employed to develop an analytic and numerically efficient model for wave scattering by a target near an interface.

THIS PAGE INTENTIONALLY LEFT BLANK

TABLE OF CONTENTS

THIS PAGE INTENTIONALLY LEFT BLANK

LIST OF FIGURES

LIST OF TABLES

THIS PAGE INTENTIONALLY LEFT BLANK

ACKNOWLEDGMENTS

This work was supported, in part, by the Office of Naval Research Ocean Acoustics Program [Award No. N00014-17WX00773].

THIS PAGE INTENTIONALLY LEFT BLANK

I. INTRODUCTION

This dissertation is a collection of four peer-reviewed journal articles in published [1], [2], review [3], and in preparation to be submitted status. Additionally, these results were presented at the 173rd and 175th Acoustical Society of America Meetings [4]–[6]. The focus of the study pertains to the acoustic wave scattering by objects within the Rayleigh scattering regime, i.e., when the scattering object's dimensions are small compared to wavelength.

Rayleigh scattering is a classical and widely studied problem in wave theory [7]–[9]. It is generally studied assuming plane incident waves [10]–[14]. However, knowledge of the full Green's functions becomes necessary for a multitude of scattering problems [15]–[18] for which the physical spacing between the scatters themselves or the scatterers' separation from a boundary or source is comparable to their size [15], [19]–[22]. In underwater acoustics, such problems often arise in scattering by multi-scatterer configurations [23] and when calculating the radiation and scattering by objects near the ocean surface [19], [24] or seafloor [25]–[27]. In general, for problems when the full Green's functions are necessary then numerical methods are used in the development of solutions. A lack of simple analytic and readily available solutions to such problems is the motivation for the current study. Compact analytic solutions can provide physical insights leading to new applications.

The exact solutions to the problems of monochromatic wave scattering by cylinders [14], [28], [29] and spheres [10], [14], [30], [31] are well known. They are given by infinite series involving the products of Bessel functions, and Bessel functions and Legendre polynomials, respectively. A recent development in the problem of acoustic diffraction of a spherical wave by a sphere approximated the exact resultant scattered field as a field due to image sources within the object [32], [33]. The distinct physics of low-frequency scattering allowed for a considerable reduction in the complexity in the mathematical description of the exact solution.

An image source solution to this problem was envisioned through the structure of the classical static solution by Rayleigh for the electric potential due to a point charge in the presence of a grounded conducting sphere [34]. The equivalent solution to this static problem consists of only two charges: the original charge and an image charge located within the sphere at the Kelvin Inversion point. The physical insight into the static solution led to the construction of a compact uniformly asymptotic solution for spherical wave scattering by a sphere [32], [33]. The solution is valid in the Rayleigh scattering regime for arbitrary source and receiver locations outside of the sphere.

In Chapter II, the method of matched asymptotic solutions that was developed for spherical targets is extended to wave scattering by an infinite cylinder with a radius that is small compared to the wavelength. Similarly, as for the sphere, the viability of an image source solution was anticipated due to known electrostatic [35] and magnetostatic [36] stationary limits involving cylinders. Rayleigh scattering of cylindrical waves by soft, hard, and impedance cylinders is considered and uniform asymptotic solutions are developed. The scattered field is expressed as the sum of fields due to image sources within the object. The derived uniform asymptotic solutions are valid for the Rayleigh scattering regime and describe the scattered field everywhere outside the cylinder for arbitrary positions of the sound source.

The techniques previously applied to the sphere and to the soft, hard, and impedance cylinder are applied to the more complex and realistic fluid and solid scatterers in Chapter III. Uniform asymptotic solutions for the scattered field are developed for the fluid and solid cylinder, and solutions are revisited for soft, hard, and impedance cylinders. The scattered field is expressed as the sum of fields due to a finite number of image sources located within the object, albeit with a different image source structure than previously derived. The uniform asymptotic solutions derived represent a simple, accurate, and uniformly valid approximation of the exact solution for arbitrary positions of the source and receiver outside of the cylinder.

In Chapter IV, the derived acoustic Green’s functions for cylindrical and spherical scatterers are employed in a theoretical analysis of an approach to underwater noise mitigation. The approach relies on a wave-diffraction based technique for passive

suppression of low-frequency noise rather than reflection or dissipation. The feasibility of underwater noise mitigation by placing a small compliant body near the source is evaluated. Analytic solutions for sound diffraction on cylinders and spheres streamlines the analysis.

The 2-D scattering problem of cylindrical wave diffraction by an infinite cylinder near an interface is considered in Chapter V. This problem is of interest in its own right, but also because it can be viewed as a 2-D model for the scattering of a spherical wave by a sphere near a plane interface. In either case, no exact analytic solution is available. When an object is located close to an interface, reflections of the incident and single-scattered waves from the boundary lead to multiple scattering from the object. In general, this problem is solved either by neglecting the multiple scattering or through various numerical methods [19], [22], [37]. Here, an analytic and geometric approach is developed utilizing the previously derived acoustic Green's functions coupled with the method of images in iteration. The approach provides a numerically efficient and physically intuitive solution into a multiple-scattering problem. The solution is valid in the Rayleigh scattering regime and for arbitrary positions of the source and receiver relative to the cylinder and the interface.

Lastly, Chapter VI is a summary of the findings of the dissertation research.

THIS PAGE INTENTIONALLY LEFT BLANK

II. RAYLEIGH SCATTERING OF A CYLINDRICAL SOUND WAVE BY AN INFINITE CYLINDER

This chapter was previously published as [1]: Alexander B. Baynes and Oleg A. Godin, "Rayleigh scattering of a cylindrical sound wave by an infinite cylinder," *The Journal of Acoustical Society of America*, vol. 142, no. 6, pp. 3613–3623, 2017.

A. INTRODUCTION

Scattering of waves due to objects that are small relative to wavelength, commonly referred to as Rayleigh scattering, is a classical and widely studied subject in wave theory. Commonly, within the Rayleigh regime, scattering is investigated for plane incident waves, and general asymptotic solutions have been obtained specifically for low frequency and far field regimes [10]–[14]. However, knowledge of the full Green's functions is necessary for many problems of current interest for which the physical spacing between the scatterers themselves or the scatterers' separation from a source or boundary is comparable to their size. In underwater acoustics, such problems can arise in dense multi-scatterer configurations [23], radiation by finite sources [38]–[41], target classification [42]–[44], source localization [45], scattering suppression [46], [47], and when calculating the radiation and scattering of sound due to objects located near the ocean surface [19], [24] or the seafloor [25]–[27]. No simple analytic solutions are readily available for such problems, and numerical methods have to be used. This is the motivation for the present study. Compact analytic solutions can provide physical insights leading to new applications. For instance, the feasibility of underwater noise mitigation by placing a small compliant body near the source was tested. The approach relies on wave diffraction rather than dissipation or reflection. The analysis was streamlined using analytic solutions for sound diffraction on simple shapes [2].

The exact solution of scattering of a monochromatic cylindrical wave by a soft and hard cylinder is given by an infinite series that involves the products of Bessel functions

[14]. Recently, an analytical approach was developed to derive simple asymptotic solutions for a spherical sound wave scattered by a small sphere representing soft, impedance, hard, and homogenous fluid targets [32], [33]. The technique results in approximating the scattered wave as a sum of fields due to "image sources." The viability of the image source method was anticipated from known stationary limits for simple geometries such as the classical electrostatic problem involving a grounded sphere and a point charge with the elementary solution obtained by Kelvin [34].

In this chapter, we extend the analytical method of matched asymptotic expansions developed for spherical targets and apply it to cylindrical wave scattering by an infinitely long circular cylinder with a radius small compared to the wavelength. Rayleigh scattering by soft, hard, and impedance cylinders is considered with the goal of developing a simple, accurate, and uniformly valid approximation of the exact solution for arbitrary positions of the source and receiver outside of the cylinder. The developed 2-D Green's functions hold everywhere outside of the cylinder, have a similar structure to the static limits in the electrostatic [35] and magnetostatic [36] solutions, and are represented by the sums of "image sources" within the scatterer. The asymptotic Green's functions allow a clear physical interpretation and lead to a computationally efficient approach to solve more complicated problems for the scattering of sound in underwater waveguides. For instance, representation of the scattered wave as the field due to several linear sources immediately allows computation of the acoustic pressure in a waveguide as a superposition of local normal modes [48].

This chapter is organized in the following manner. In Section II.B, the theoretical background of cylindrical wave scattering is presented with the exact solution. In Section II.C, a uniform asymptotic solution for the scattered wave is developed in the Rayleigh regime by matching two local asymptotic solutions. Accuracy of the uniform asymptotic solution is quantified and analyzed in Section II.D. In Section II.E, the asymptotic image solution and the properties of the scattered wave that the solution reveals are utilized to study the performance of plane wave beamforming and matched field processing techniques in bearing estimation by mounted receivers. Lastly, Section II.F is a summary of our findings.

B. THEORETICAL BACKGROUND

In this scattering problem, monochromatic incident cylindrical waves of frequency ω are considered, emanating from an infinite line source. The cylindrical waves are incident upon and diffracted by an infinite circular cylinder of constant radius *a*. The axis of the cylinder is parallel to the linear source. The cylinder and source are embedded in a homogenous fluid with density ρ and sound speed *c*. Scattering by acoustically soft, hard, and impedance cylinders is considered. The scattering problem described is effectively a two-dimensional problem due to the acoustic complex pressure field being independent of the *z*-coordinate along the cylinder axis. The scattering geometry is represented using the polar coordinate system consisting of the coordinates (r,θ). The origin of the coordinate system is located at the center of the cylindrical scattering body. Cartesian coordinates are defined by the usual relationships $x = r\cos\theta$ and $y = r\sin\theta$.

Acoustic pressure in an incident cylindrical wave emanating from an infinite acoustic line source is classically and compactly expressed as [14]

$$p_{in} = H_0^{(1)}\left(kR\left(b\right)\right),\ R\left(x_0\right) = \sqrt{\left(x - x_0\right)^2 + y^2}\ . \tag{2.1}$$

Time dependence exp(–iωt) is assumed and suppressed. Let *p* be the acoustic pressure, which is a sum of the incident and scattered waves: $p = p_{in} + p_{sc}$; $k = \omega / c$ is the acoustic wave number, $b > a$ is the distance from the source to the center of the scatterer, $R\left(x_0\right)$ is the distance between the field observation point $\left(x, y\right)$ and any point x_0 along the line connecting the origin and the source (Figure 1). Additionally, $H_0^{(1)}\left(q\right)$ is the Hankel function of the first kind of 0th order. Hankel functions are the linear combination [49] $H_n^{(1)}\left(q\right) = J_n\left(q\right) + iY_n\left(q\right)$ of the Bessel function $J_n\left(q\right)$ and the Neumann function $Y_n\left(q\right)$. For large arguments, Hankel functions have the following asymptotic behavior [49]:

$$H_n^{(1)}\left(q\right) \sim \sqrt{2/\pi q}\exp\left(iq - in\pi/2 - i\pi/4\right),\ \left|q\right| >> 1,\ -\pi < \arg q < 2\pi, \tag{2.2}$$

and represent outgoing waves.

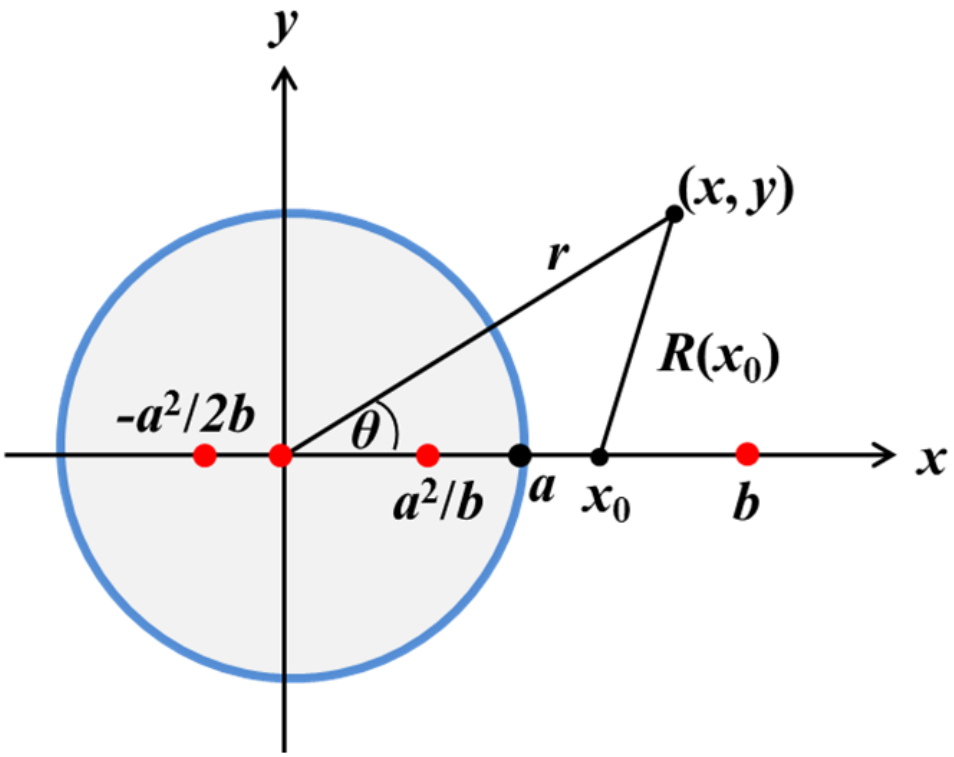

Figure 1. Two-dimensional cross-section of the geometry of the cylindrical scattering problem. Depicted is the acoustic pressure line source located at coordinates (b, 0) outside an infinite cylindrical scatterer of radius a and axis at (0, 0). The field observation point is located at (x, y). Additionally, shown are the coordinates of three image acoustic line sources located within the cylinder at coordinates (a^2/b, 0), (0, 0), and ($-a^2/2b$, 0). The distance R is formally defined in Eq. (2.1) and employed from Eq. (2.28) onward.

The scattered field satisfies the two-dimensional homogeneous Helmholtz equation,

$$\nabla^2 p_{sc} + k^2 p_{sc} = 0, \quad r > a\,. \tag{2.3}$$

Boundary conditions on the surface of the cylinder depend on the type of the scatterer. For the soft cylinder, i.e., a cylinder with a pressure release surface, the boundary condition is the Dirichlet boundary condition for the total acoustic pressure [33]. In terms of the incident and scattered waves,

$$p_{sc} = -p_{in}, \quad r = a\,. \tag{2.4}$$

At the acoustically hard surface, the particle velocity normal to the cylinder's surface is zero. The hard cylinder is described by imposing a Neumann boundary condition [33], which can be expressed as

$$\frac{\partial p_{sc}}{\partial r} = -\frac{\partial p_{in}}{\partial r}, \quad r = a\,. \tag{2.5}$$

The surface of the impedance cylinder is neither perfectly hard nor soft, but has intermediate acoustic properties. The boundary condition on the impedance surface is [33]

$$p_{sc} + \frac{\zeta}{k}\frac{\partial p_{sc}}{\partial r} = -p_{in} - \frac{\zeta}{k}\frac{\partial p_{in}}{\partial r}, \quad r = a\,, \tag{2.6}$$

where ζ is a dimensionless impedance. In this context, the limiting cases of acoustically soft and hard surfaces are recovered at $\zeta \to 0$ and $|\zeta| \to \infty$, respectively.

The exact solution of the problem of cylindrical wave scattering by an infinite cylinder is known, and the expressions for the incident and scattered fields valid outside of the cylinder can be written in terms of infinite sums of cylindrical harmonics as a function of only r and θ [14]

$$p_{in} = \sum_{n=0}^{\infty} \varepsilon_n H_n^{(1)}\left(kr_>\right) J_n\left(kr_<\right) \cos n\theta, \quad r_> = \max\left(r,b\right), \quad r_< = \min\left(r,b\right), \tag{2.7}$$

$$p_{sc} = -\sum_{n=0}^{\infty} \varepsilon_n A_n H_n^{(1)}\left(kb\right) H_n^{(1)}\left(kr\right) \cos n\theta, \quad r \geq a\,, \tag{2.8}$$

where ε_n is the Neumann symbol ($\varepsilon_0 = 1;\ \varepsilon_n = 2$ for $n \geq 1$). The value of representing the incident field by the summation in Eq. (2.7) vice the equivalent form of Eq. (2.1) is the consequent simplification of finding the coefficients A_n for the scattered field. The coefficients are determined through substitution of Eqs. (2.7) and (2.8) into the boundary conditions, Eqs. (2.4)–(2.6). After substitution, solving for the A_n coefficients is simply a matter of equating coefficients of like factors of order n using the property of linear independence of the family of $\cos n\theta$ trigonometric functions. The resulting boundary specific A_n coefficients for the soft (S), hard (H), and impedance (I) surface cases are

$$A_n^{(S)} = J_n\left(ka\right) \Big/ H_n^{(1)}\left(ka\right), \tag{2.9}$$

$$A_n^{(H)} = J_n'\left(ka\right) \Big/ H_n^{(1)\prime}\left(ka\right), \tag{2.10}$$

$$A_n^{(I)} = \left[J_n\left(ka\right) + \zeta J_n'\left(ka\right)\right] \Big/ \left[H_n^{(1)}\left(ka\right) + \zeta H_n^{(1)\prime}\left(ka\right)\right], \tag{2.11}$$

where the coefficients have been labeled case specifically and the prime denotes the derivative of the original function with respect to its argument. Substitution of Eqs. (2.9)–(2.11) into Eq. (2.8) gives the exact solution for scattering (diffraction) of a cylindrical wave by acoustically soft, hard, and impedance cylinders, respectively.

C. DERIVATION OF THE ASYMPTOTIC SOLUTIONS OF THE SCATTERED WAVE

In development of the asymptotic solution, we consider only the scattering within the Rayleigh regime, i.e., when

$$ka << 1. \tag{2.12}$$

1. Small Argument Approximation and Recursion Relationships for Bessel Functions

Below, we will repeatedly use the small argument expressions [49]

$$J_n(q) = \frac{1}{n!}\left(\frac{q}{2}\right)^n \left[1 + O\left(q^2\right)\right], \quad n = 1,\ 2,\ 3, \ldots, \tag{2.13}$$

$$H_n^{(1)}(q) = -\frac{i(n-1)!}{\pi}\left(\frac{2}{q}\right)^n \left[1 + O\left(\kappa^2(q)\right)\right], \quad n = 1,\ 2,\ 3, \ldots, \tag{2.14}$$

for Bessel and Hankel functions. Here and below, the notation $\kappa^2(q) = q^2\left(1 + |\ln q|\right)$ is used for brevity. Additionally, Bessel and Hankel approximations for the 0[th] order terms are

$$J_0(q) = 1 - q^2/4 + O\left(q^4\right), \tag{2.15}$$

$$H_0^{(1)}(q) = 1 + \left(\ln(q/2) + \gamma\right)2i/\pi + O\left(\kappa^2(q)\right), \tag{2.16}$$

where $\gamma = 0.5772157...$ is Euler's constant. [49] Equations (2.10)–(2.11), which represent the coefficients for the hard and impedance cases, respectively, require small argument limits of derivatives of Bessel and Hankel functions. The following relationships [49]

$$\begin{gathered} \chi_0'(q) = -\chi_1(q),\ 2\chi_n'(q) = \chi_{n-1}(q) - \chi_{n+1}(q), \\ \chi_n'(q) = -\chi_{n+1}(q) + \chi_n(q)n/q, \end{gathered} \tag{2.17}$$

for derivatives of Bessel functions prove useful. Here, χ denotes J, Y, $H^{(1)}$ or any linear combination of these functions of the same order *n*.

2. A_n Coefficients in the Rayleigh Regime

Using Eqs. (2.13)–(2.17), the A_n coefficients for the soft and hard cylinders, Eqs. (2.9)–(2.10), simplify and become

$$A_0^{(S)} = \left[1+\frac{2i}{\pi}\left(\ln\left(\frac{ka}{2}\right)+\gamma\right)\right]^{-1}\left[1+O\left(k^2a^2\right)\right], \tag{2.18}$$

$$A_0^{(H)} = i\pi\left(ka/2\right)^2\left[1+O\left(\kappa^2\left(ka\right)\right)\right], \tag{2.19}$$

$$A_n^{(S)} = -A_n^{(H)} = i\pi\left[n!(n-1)!\right]^{-1}\left(ka/2\right)^{2n}\left[1+O\left(\kappa^2\left(ka\right)\right)\right],\ n=1,\ 2,.... \tag{2.20}$$

In order to derive the approximate coefficients for the impedance cylinder, we impose the following restriction on the solution:

$$ka << \left|\zeta\right|. \tag{2.21}$$

In view of Eq. (2.12), Eq. (2.21) is not a strong additional assumption. Using condition (2.21), the derivative relationships defined in (2.17), and substitution of Eqs. (2.13)–(2.16) into Eq. (2.11), after simplification yields the approximate coefficients for the impedance cylinder:

$$\begin{aligned} A_0^{(I)} &= \frac{i\pi ka\left(\zeta ka/2-1\right)}{2\zeta - i\pi ka\left(1+\left(\ln\left(ka/2\right)+\gamma\right)2i/\pi\right)}\left[1+O\left(\kappa^2\left(ka\right)\right)\right], \\ A_n^{(I)} &= J_n'(ka)\Big/H_n^{(1)\prime}(ka)\left[1+O\left(ka/n\zeta\right)\right],\ \ n=1,\ 2,.... \end{aligned} \tag{2.22}$$

Note that, under condition (2.21), only the $A_0^{(I)}$ and $A_0^{(H)}$ coefficients differ for the impedance and hard cylinders. The effect of the surface impedance on the scattered wave is solely contained in the $A_0^{(I)}$ term. Identical results were found for the small sphere [33]. Consequently, the scattering problem for the impedance cylinder can be readily solved if the hard cylinder solution is known. All that is needed for a complete solution is computation and replacement of the 0th order coefficient into the hard cylinder solution.

Substitution of the approximate coefficients defined in Eqs. (2.18)–(2.20), and (2.22) into (2.8) solves the cylindrical scattering problem approximately in the Rayleigh regime over the entire domain of $r, b \geq a$ in terms of an infinite sum for the soft, hard, and impedance cylinder. In analysis of the coefficients, the A_0 coefficients are unique with respect to proportionality of the order of ka. For the soft, impedance, and hard scatterers

the 0^{th} order coefficients are proportional to $1/\ln ka$, ka, and k^2a^2, respectively. At $n = 0$, both the impedance and hard coefficients are small unlike the soft coefficient. For $n \geq 1$, the coefficients are all similarly proportional to $(ka)^{2n}$ and so, within the Rayleigh regime, the amplitude of the terms in the infinite sum rapidly decrease with increasing order *n*. In view of this, the relative importance of the first two terms for the three cases is drastically different. For the soft and impedance cylinders, the first term is dominant and the overall solution behaves more like a monopole source at the origin and is relatively angle independent. However, for the hard cylinder the first two terms are equally proportioned with respect to *ka*, and so the approximation will behave more like the summation of a monopole and dipole source at the origin resulting in more significant angle dependence.

The coefficients for the soft and hard cylinders in the limit of small *ka* are related simply by $A_n^{(S)} = -A_n^{(H)}$ for $n \geq 1$ to a factor of $1 + O\left(\kappa^2 (ka)\right)$. In view of this property it is more convenient to use the compact expression

$$A_n = A_1 \left[(n-1)!\right]^{-2} (ka/2)^{2n-2} \Big/ n\left[1 + O\left(\kappa^2 (ka)\right)\right], \quad n = 1,\ 2, \ldots, \tag{2.23}$$

where the effect of the boundary condition is encapsulated within the respective A_1 case specific coefficient.

3. Inner Asymptotic: Sound Source and Receiver Are Close to the Scatterer

Consider the inner domain of the asymptotic as the region for which the sound source and the receiver are both located geometrically close to the scatterer. More quantitatively, the source and receiver are located within a fraction of a wavelength from the center of the cylinder, i.e.,

$$kb << 1, \quad kr << 1. \tag{2.24}$$

Restrictions in this form allow use of the small argument approximations presented in Section II.C.1. Starting from Eq. (2.8) for the exact scattered field, using Eq. (2.23) for the A_n coefficients and the small argument approximation (2.14) for the respective Hankel functions as a result of condition (2.24), this yields

$$p_{sc} = -A_0 H_0^{(1)}(kb) H_0^{(1)}(kr) + \frac{8A_1}{\pi^2 k^2 a^2} S\left(\frac{a^2}{br}, \theta\right)\left[1 + O\left(\kappa^2(kb) + \kappa^2(kr)\right)\right], \quad (2.25)$$

where

$$S(\alpha, \beta) = \sum_{n=1}^{\infty} \frac{\alpha^n}{n} \cos n\beta . \quad (2.26)$$

The scattered field in Eq. (2.8) is now simplified and reduced to two terms: the wave due to a line source at the origin and a field proportional to a geometric sum. The sum $S(\alpha, \beta)$ is independent of sound frequency and only dependent on the geometric parameters *a*, *b*, *r*, and θ. Note that $0 < \alpha < 1$ and $0 \le \beta \le 2\pi$ for the scattered wave. Because $\sum_{n=1}^{\infty} \alpha^n$ is a convergent series, and since $\left|\cos(n\beta)/n\right| \le 1$, the infinite series in (2.26) is absolutely convergent. The sum in Eq. (2.26) can be evaluated in a closed form by using the exponential form of the cosine function and separating the total sum into the sum of two independent series. Using the power series representation of $-\ln(1-x) = \sum_{n=1}^{\infty} x^n/n$, for $|x| < 1$, the sum is written as

$$S(\alpha, \beta) = -0.5 \ln\left(1 - 2\alpha \cos\beta + \alpha^2\right), \ 0 < \alpha < 1. \quad (2.27)$$

Recognizing that $\sqrt{1 - 2\alpha\cos\beta + \alpha^2} = R(x_0)/r$ when $\beta = \theta$ and $x_0 = a^2/b$, ultimately the sum can be evaluated exactly as

$$S(a^2/br, \theta) = -\ln\left[R(a^2/b)/r\right]. \quad (2.28)$$

Substitution of Eq. (2.28) into the approximate scattered field in Eq. (2.25) yields a compact expression for the scattered field. However, the second term in the expression with coefficient A_1 satisfies the two-dimensional Laplace equation, $\nabla^2 p = 0$, and not the Helmholtz equation (2.3). The scattered acoustic pressure field, however, can be expressed in terms of cylindrical functions that explicitly satisfy the Helmholtz equation using the relationship in Eq. (2.16) between logarithms and Hankel functions for small arguments. Within the accuracy of Eq. (2.25), the exact expression for the sum in Eq. (2.28) can be represented approximately in terms of two acoustic image line sources. Ultimately, the scattered field is

$$p_{sc} = \left\{ \left(-A_0 H_0^{(1)}(kb) - \frac{4i}{\pi} \frac{A_1}{k^2 a^2} \right) H_0^{(1)}(kr) + \frac{4i}{\pi} \frac{A_1}{k^2 a^2} H_0^{(1)}\left(kR\left(\frac{a^2}{b} \right) \right) \right\} \times \left[1 + O\left(\kappa^2 (kb) + \kappa^2 (kr) \right) \right]. \tag{2.29}$$

For arbitrary *a*, *b*, and *r* values for which conditions (2.12) and (2.24) hold, Eq. (2.29) represents an inner local asymptotic solution of the scattered acoustic field. The asymptotic reproduces the scattered wave field up to the factor $1 + O\left(\kappa^2 (kb) + \kappa^2 (kr) \right)$ and exactly satisfies the Helmholtz equation. The solution is dependent only on the A_0 and A_1 coefficients specific to the soft, hard, and impedance boundary conditions. For all three cases, the scattered wave is composed of the simple sum of fields due to two image line sources located at the center of the scatterer and at the point $\left(a^2/b, 0 \right)$. The latter point shares the same coordinates to the Kelvin inversion point, which arises in the well-known solution first obtained by Kelvin for the classical electrostatic problem involving a grounded sphere and a point charge [34].

Equation (2.29) is valid in the low frequency limit for which $k \to 0$ while geometric parameters *a*, *b*, and *r* remain fixed. In the stationary limit for the soft and hard cylinders the resulting pressure fields reduce to

$$\lim_{k \to 0} p^{(S)} = 2i\pi^{-1} \left[\ln\left(R(b) \right) - \ln\left(R\left(a^2/b \right) \right) - \ln\left(b/a \right) \right], \tag{2.30}$$

$$\lim_{k \to 0} p_{sc}^{(H)} = 2i\pi^{-1} \left[\ln\left(R\left(a^2/b \right) \right) - \ln r \right]. \tag{2.31}$$

In the stationary limit, both fields represented in Eqs. (2.30) and (2.31) are exact solutions to Laplace's equation. The acoustically soft cylinder has a direct electrostatic analog for which there is an infinite electric line charge running parallel to a grounded infinite perfectly conducting cylinder. In the stationary limit the total acoustic pressure $p^{(S)}$ exactly corresponds to the electrostatic potential of such an analog problem. Through inspection, the stationary limit in Eq. (2.30) corresponds exactly to the known electrostatic solution [35]. Similarly, the hard cylinder stationary limit for pressure represented in Eq. (2.31) has both a magnetostatic analog and a fluid mechanics interpretation. The pressure in this case corresponds to the scalar magnetic field potential resulting from an infinite magnetic line charge that is running parallel to a grounded infinite perfectly conducting cylinder. The

stationary limit Eq. (2.31) is consistent with the known exact magnetostatic solution [36]. In the fluid mechanics context, the pressure corresponds to the fluid velocity potential of a mass injection source in the presence of an impenetrable circular cylinder. Like in the soft cylinder case, Eq. (2.31) is consistent with the known exact solution [50].

4. Outer Asymptotic: Sound Source or Receiver (or Both) Is Far from the Scatterer

To develop the outer local asymptotic, we will assume that the distance to the center of the scatterer from the sound source or receiver (or both) is large compared to the cylinder radius *a*. This assumption is expressed compactly as follows:

$$\alpha \equiv a^2/br << 1. \tag{2.32}$$

The small scatterer condition (2.12) still holds, however, conditions (2.24) are no longer imposed.

In view of Eq. (2.20), the coefficients A_n in the exact solution for the scattered field are proportional to $(ka)^{2n}$ for $n \geq 1$. For small *ka*, the A_n coefficients rapidly decrease with increasing order *n* and the scattered field as represented by the series Eq. (2.8) is expected to converge rapidly. However, the values of the Hankel functions in the products $A_n H_n^{(1)}(kb) H_n^{(1)}(kr)$ in Eq. (2.8) may increase with *n*. Through inspection of limiting cases, using Eqs. (2.2) and (2.14), the value of each term in the series for $n \geq 1$ is proportional to a factor of $\left(a^2/br\right)^n = \alpha^n$. Under condition (2.32), α is necessarily small, and only a few first terms contribute appreciably to the series in Eq. (2.8). The $n = 3$ term in Eq. (2.8) is of second order in the parameter α relative to the term with $n = 1$. For the outer local asymptotic, the first three terms for the scattered field in Eq. (2.8) are sufficient, under condition (2.32), to provide requisite second-order accuracy in α. The scattered field then can be approximately expressed as,

$$\begin{aligned} p_{sc} = \Big\{ & -A_0 H_0^{(1)}(kb) H_0^{(1)}(kr) - 2A_1 H_1^{(1)}(kb) H_1^{(1)}(kr)\cos\theta \\ & -2A_2 H_2^{(1)}(kb) H_2^{(1)}(kr)\cos 2\theta \Big\} \times \left[1 + O\left(\alpha^2 + k^2 a^2\right)\right]. \end{aligned} \tag{2.33}$$

The outer local asymptotic, however, needs to be expressed in terms of fields due to line sources in order to match the inner and outer solutions. Replacement of both the

$H_1^{(1)}(kr)\cos\theta$ and $H_2^{(1)}(kr)\cos 2\theta$ terms in Eq. (2.33) is then necessary. Consider an alternative representation of the scattered field that can be constructed to the same accuracy as in Eq. (2.33):

$$\psi = B_0 H_0^{(1)}(kr) + B_1 H_0^{(1)}\left(kR\left(a^2/b\right)\right) + B_2 H_0^{(1)}\left(kR\left(\beta a^2/b\right)\right). \tag{2.34}$$

Equation (2.34) represents the scattered wave as the field due to three acoustic image line sources with unknown amplitudes. Equation (2.34) contains the image line sources located at $(0,0)$ and $\left(a^2/b,0\right)$, which were previously encountered in the static limit and in the inner asymptotic solution, and allows for an additional image line source. The additional image source is required to develop a solution to the accuracy desired. To satisfy the physical requirement that the acoustic field has no singularities except at the actual sound source location, the additional image source needs to be located inside the scatterer. This is ensured by the condition $-1<\beta<1$ since $a^2/b \le a$.

Through inspection it was found that the third image source location is not unique, with different choices of β resulting in different values of the source amplitudes B_0, B_1, and B_2 in Eq. (2.34). Consideration is necessary in selecting a β value that does not complicate the problem. For example, when $\beta=-1$, an artificial and nonphysical singularity arises in the domain of interest when $b=a$, specifically, at the point $(x,\mathrm{y})=(-a,0)$. The value $\beta=-1/2$ is chosen in the development below, resulting in a third image line source located at $\left(-a^2/2b,0\right)$ (Figure 1). This selection conveniently simplifies the algebra.

Calculation of the unknown amplitudes B_0, B_1, and B_2 in Eq. (2.34) is accomplished using Graf's Addition Theorem for Bessel functions (see [49], p. 363) using the identity

$$\begin{aligned} H_0^{(1)}\left(kR\left(\mu a^2/b\right)\right) &= H_0^{(1)}(kr)\,J_0\left(\mu k a^2/b\right) + 2H_1^{(1)}(kr)\,J_1\left(\mu k a^2/b\right)\cos\theta \\ &\quad + 2H_2^{(1)}(kr)\,J_2\left(\mu k a^2/b\right)\cos 2\theta + O\left(\alpha^3 + \left(ka^2/b\right)^3/\sqrt{kr}\right). \end{aligned} \tag{2.35}$$

Using the linear independence of the cylindrical harmonics, substitution of Eq. (2.35) into Eq. (2.34) with $\mu=1$ and $\mu=-1/2$, and then equating ψ and p_{sc}, yields three algebraic equations for three unknowns and importantly does not reduce the original accuracy of the

approximation in Eq. (2.33). Solving the system of equations for the B_n coefficients in terms of A_n coefficients yields

$$B_0 = -A_0 H_0^{(1)}(kb) - B_1 J_0\left(ka^2/b\right) - B_2 J_0\left(ka^2/2b\right), \tag{2.36}$$

$$B_1 = -\frac{A_1 H_1^{(1)}(kb) J_2\left(ka^2/2b\right) + A_2 H_2^{(1)}(kb) J_1\left(ka^2/2b\right)}{J_1\left(ka^2/b\right) J_2\left(ka^2/2b\right) + J_2\left(ka^2/b\right) J_1\left(ka^2/2b\right)}, \tag{2.37}$$

$$B_2 = \frac{A_1 H_1^{(1)}(kb) J_2\left(ka^2/b\right) - A_2 H_2^{(1)}(kb) J_1\left(ka^2/b\right)}{J_1\left(ka^2/2b\right) J_2\left(ka^2/b\right) + J_2\left(ka^2/2b\right) J_1\left(ka^2/b\right)}. \tag{2.38}$$

Substitution of the derived coefficients, Eqs. (2.36)–(2.38), and $\beta = -1/2$ into Eq. (2.34) exactly reproduces the quantity in braces in Eq. (2.33), resulting in an expression for the outer local asymptotic solution for the scattered acoustic pressure and approximates the exact field to a factor of $1 + O\left(\alpha^2 + k^2 a^2\right)$. The outer local asymptotic reduces the scattered pressure field to the sum of fields due to three line sources located within the cylinder at coordinates $(0,0)$, $\left(a^2/b, 0\right)$, and $\left(-a^2/2b, 0\right)$ in terms of the Cartesian coordinates (x, y) for a source located at $(b, 0)$.

5. Uniform Asymptotic of the Scattered Wave

In the Rayleigh scattering regime (2.12), the inequality Eq. (2.32) is met when either of the inequalities in Eq. (2.24) is violated. Moreover, the inequalities in Eqs. (2.24) and (2.32) can hold simultaneously. Thus, the inner and outer asymptotic solutions obtained above have an overlapping domain of validity and together allow one to calculate p_{sc} at every point outside the scatterer. The inner local asymptotic solution (2.29) approximates the exact field to a factor of $1 + O\left(\kappa^2(kb) + \kappa^2(kr)\right)$ and the outer local asymptotic solution (2.34), with $\beta = -1/2$ and using coefficients (2.36)–(2.38), approximates the exact field to a factor of $1 + O\left(\alpha^2 + k^2 a^2\right)$. By bridging these separate solutions by way of a single expression that subsumes both the inner and outer local asymptotic solutions, a single closed-form solution can be developed that is valid over the entire domain outside of the cylinder for arbitrary locations of the source and receiver.

Let

$$P = B_0 H_0^{(1)}(kr) + B_1 H_0^{(1)}\left(kR\left(a^2/b\right)\right) + B_2 H_0^{(1)}\left(kR\left(-a^2/2b\right)\right), \tag{2.39}$$

with B_n coefficients given by Eqs. (2.36)–(2.38). Equation (2.39) is an exact solution of the Helmholtz equation (2.3) everywhere outside the scatterer and coincides with the outer asymptotic solution. Using Eqs. (2.13)–(2.16) and (2.36)–(2.38) it can be shown that, under conditions (2.24), Eq. (2.39) for P subsumes the inner local asymptotic solution Eq. (2.29) to within the accuracy of the latter. Under condition (2.24), the amplitude B_2 of the image source with coordinates $\left(-a^2/2b, 0\right)$ tends to zero, while B_0 and B_1 tend to the amplitudes of the respective image sources in Eq. (2.29), thus reducing Eq. (2.39) to the inner local solution. As a result, Eq. (2.39) represents the uniform asymptotic solution; it approximates the scattered acoustic pressure field due to an incident cylindrical wave and is valid over the entire domain outside the cylinder.

The B_n coefficients (2.36)–(2.38) for the image line sources are relatively complex expressions composed of special functions and the first three A_n coefficients for the specific soft, hard, and impedance surfaces as defined exactly in Eqs. (2.9)–(2.11) and approximately in Eqs. (2.18)–(2.20), and (2.22). Equations (2.36)–(2.38) can be readily simplified by taking into account that $ka^2/b \le ka << 1$ and using the approximate form of the A_n coefficients. However, without much extra computational burden, the exact expressions for A_n and B_n produce significantly more accurate results over a broader range of ka values. An additional motivation for using the exact coefficients A_n and B_n arises in the soft cylinder case. With the exact coefficients, the uniform asymptotic solution retains the property of the exact solution that, as the source approaches the surface of the cylinder ($b \to a$), for arbitrary values of k and a that $P = -p_{in}$. Physically, when a line source approaches a pressure-release boundary the total acoustic pressure field vanishes. Satisfying this physical condition exactly is not only a desired physical behavior for the uniform asymptotic solution, but it also constrains the error of the asymptotic solution. As for the hard and impedance cylinder, numerical simulations show that approximate coefficients A_n and B_n can be used. However, using the exact coefficients in

Eqs. (2.10) and (2.11) yields superior numerical accuracy, and extends the domain of validity with respect to *ka* with little additional computation.

The limiting behavior of the asymptotic solution was verified in the static limit in II.C.3. Another limit previously considered in the literature is the plane wave scattering limit. Plane wave scattering can be viewed as a limiting case of cylindrical wave scattering when the source is located far from the center of the cylinder. Using the large argument limit in Eq. (2.2), consider $e^{-ikx} = \lim_{b\to\infty}\left[\sqrt{\pi kb/2}\,\mathrm{e}^{i\pi/4}\,e^{-ikb}\,p_{in}\right]$ as a representation of an incident plane wave in terms of the incident cylindrical wave Eq. (2.1). Then, the scattered field due to an incident plane wave can be calculated as $P_{pw} = \lim_{b\to\infty}\left[\sqrt{\pi kb/2}\,\mathrm{e}^{i\pi/4}\,e^{-ikb}P\right]$ in terms of the scattered field *P* due to an incident cylindrical wave. When $b\to\infty$, the three image sources in the uniform asymptotic solution Eq. (2.39) merge, and Eq. (2.39) reduces to the outer local asymptotic solution Eq. (2.33). Substitution of the uniform asymptotic solution Eq. (2.39) for *P* gives the plane wave scattering solution

$$P_{pw} = -A_0 H_0^{(1)}(kr) + 2iA_1 H_1^{(1)}(kr)\cos\theta + 2A_2 H_2^{(1)}(kr)\cos 2\theta\,. \qquad (2.40)$$

Equation (2.40) coincides with the first three terms of the infinite series in [14] that gives an exact solution of the problem. P_{pw} provides a uniformly valid asymptotic solution for plane wave scattering by an infinite cylinder with $ka << 1$. An inspection shows that Eq. (2.40) is consistent with the classical results [12] due to Rayleigh which are valid under the additional assumption $kr >> 1$.

D. NUMERICAL SIMULATIONS

The accuracy of the uniform asymptotic solution (2.39) depends on the dimensionless parameters *kb*, *kr*, and θ for fixed values of *ka*. Asymptotic accuracy was numerically quantified through the use of MATLAB (MathWorks, Natick, MA) by comparing it to the exact solution (2.8) over various subsets of the overall domain. As shown in Figure 2 the uniform asymptotic solution is highly accurate for $ka << 1$, however, it also, surprisingly, remains applicable for all $ka \le 1$ for both the hard and soft scatterers. The asymptotic solution is systematically more accurate for the soft cylinder than the hard one. Figure 2 illustrates the rapid decrease of the relative error with the dimensionless

radius ka of the cylinder. The uniform asymptotic error is proportional to k^2a^2 when $\alpha = O(1)$ for both hard and soft cylinders which is seen in the similarly sloped lines. The asymptotic error for $\alpha << 1$ is roughly proportional to k^3a^3 for the hard cylinder and k^4a^4 for the soft cylinder. In agreement with theoretical estimates, the second order accuracy is achieved throughout with significant further improvements in accuracy when the source or receiver (or both) are located far from a small scatterer.

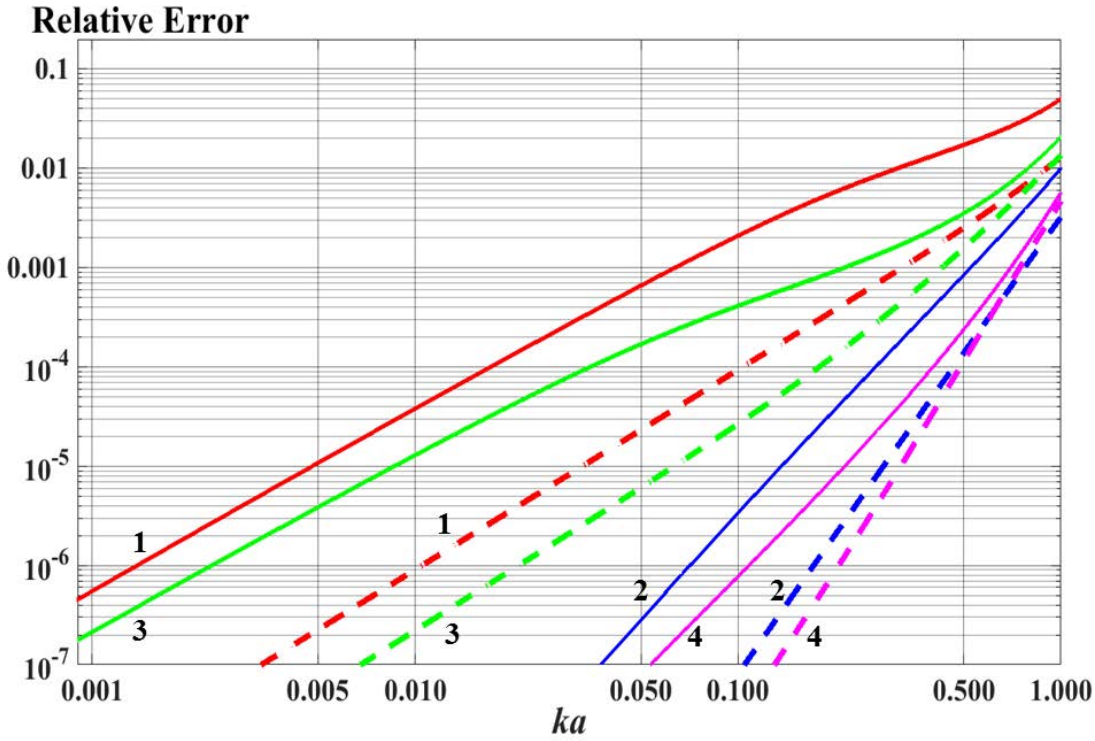

Figure 2. Accuracy of the uniform asymptotic of the scattered field. Relative error $|1\text{-}P/p_{sc}|$ between the uniform asymptotic and the exact field is plotted as a function of ka for acoustically hard (solid lines) and soft (dashed lines) cylinders. The relative error is shown for the angle $\theta = \pi/4$ and the following sets of the other geometric parameters: $b = r = 1.5a$ (1), $b = 1.5a$, $r = 10^3a$ (2), $b = 10a$, $r = 1.5a$ (3), and $b = 10a$, $r = 10^3a$ (4).

Figure 3 and Figure 4 further illustrate accuracy of the uniform asymptotic solution through the analysis of relative amplitude error ($\delta A/A$) and phase error ($\delta\varphi$). The uniform asymptotic solution is an accurate approximation of the scattered wave not only for $ka << 1$

but for all values of $ka \le 1$, over a broad range of θ and α values. Both figures illustrate nonlinear dependence of the errors on ka and also demonstrate overall greater accuracy for the soft cylinder in both amplitude and phase. There are two main reasons for the greater accuracy in the soft cylinder case. First, the A_0 coefficient is much larger for the soft cylinder than for the impedance and hard cylinders. The $n = 0$ term in the series (2.8), which is reproduced exactly in the uniform asymptotic solution, plays a much bigger role in the soft scatterer case and dominates the scattered field when $\alpha << 1$. Second, as Figure 3 illustrates, the errors for all intermediate values $0 < a < b$ are suppressed by the fact that the asymptotic solution becomes exact in the limit $a \to b$.

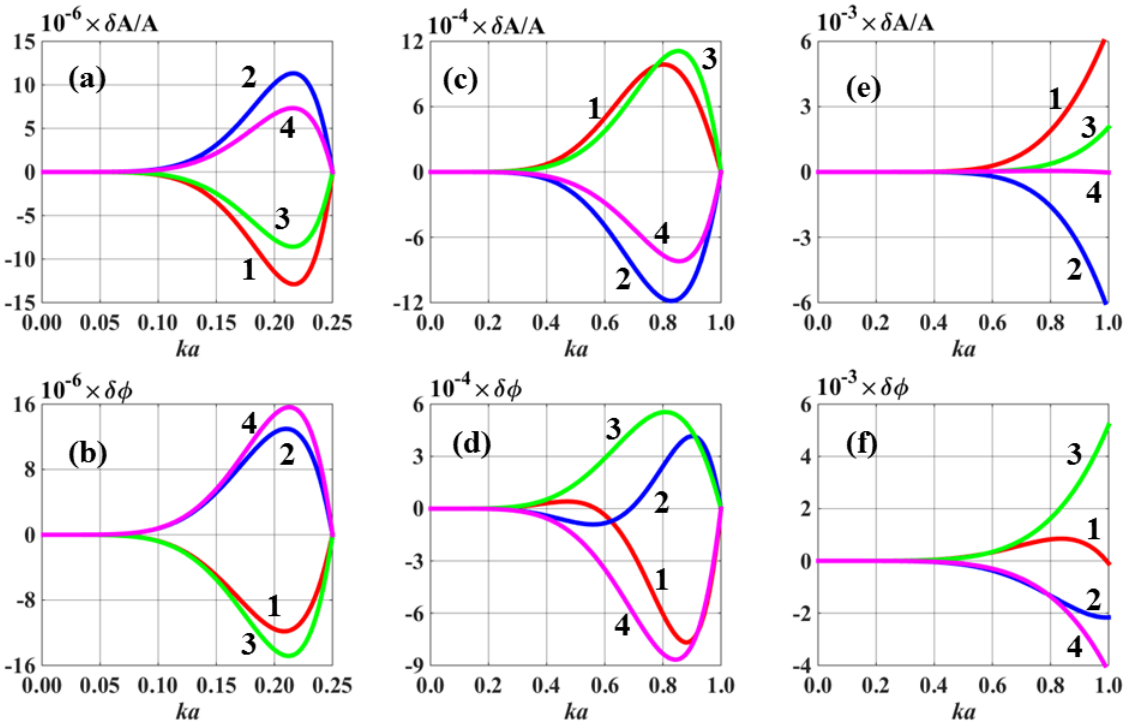

Figure 3. Accuracy of the amplitude and phase of the uniform asymptotic of the scattered field due to a soft cylinder. Plots (a), (c), (e) show relative amplitude error ($\delta A/A$) and plots (b), (d), (f) show phase error ($\delta\varphi$), all as a function of the dimensionless radius ka of the cylinder. The following dimensionless parameters were used to characterize the source and receiver positions: kb =0.25, kr =1 (a), (b), kb = 1, kr = 20 (c), (d), kb = 20, kr = 10 (e), (f) for the following values of the angles θ = 0 (1), $\pi/3$ (2), $2\pi/3$ (3), and π (4).

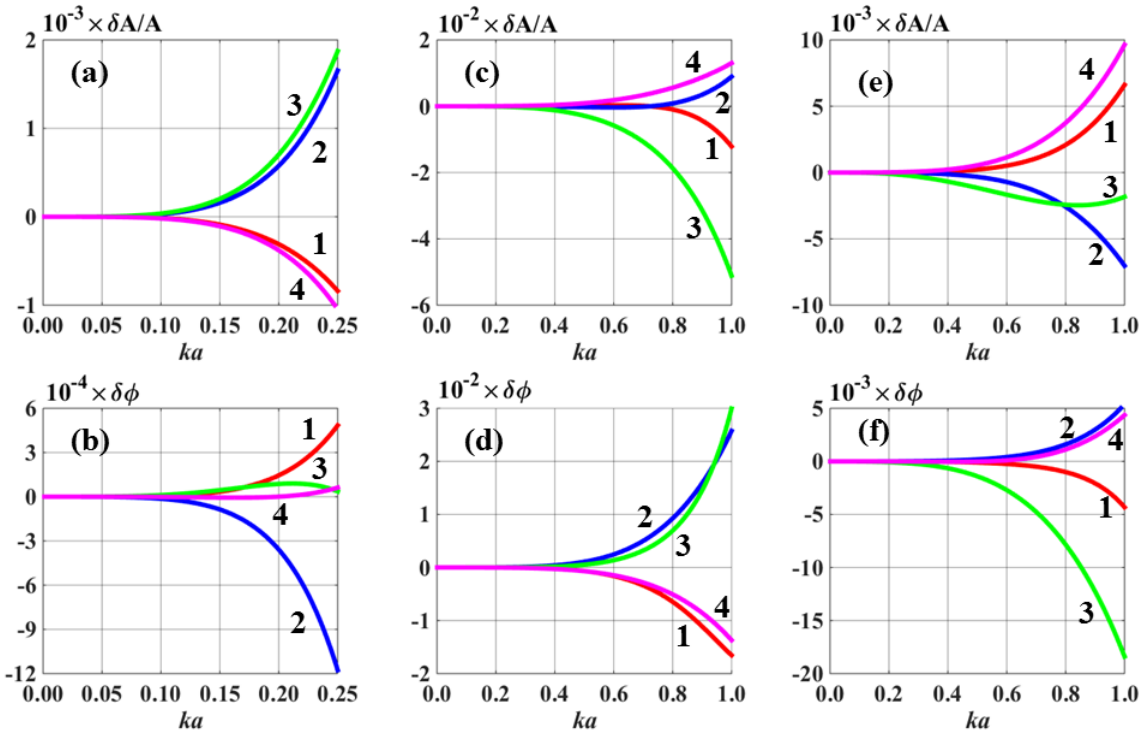

Figure 4. Accuracy of the amplitude and phase of the uniform asymptotic for the scattered field due to a hard cylinder. Plots (a), (c), (e) show relative amplitude error ($\delta A/A$) and plots (b), (d), (f) show phase error ($\delta\varphi$), all as a function of the dimensionless radius ka of the cylinder. The following dimensionless parameters were used to characterize the source and receiver positions: kb = 0.25, kr =1 (a), (b), kb = 1, kr =20 (c), (d), kb =20, kr =10 (e), (f) for the following values of the angles θ = 0 (1), $\pi/3$ (2), $2\pi/3$ (3), and π (4).

E. BEARING ESTIMATION WITH MOUNTED RECEIVERS

The utility of the uniform asymptotic solution and physical insight into scattering that it provides are illustrated in this section. We consider a simple 2-D problem of bearing estimation of a compact underwater sound source using two hydrophones mounted on a cylindrical body. The body is modelled as an acoustically hard infinite cylinder of radius a. The two hydrophones are located at points $(r,\theta)=(a,\pi)$ and $(a,0)$, with total acoustic pressure measurements denoted as $P_1 = p_{sc,1} + p_{in,1}$ and $P_2 = p_{sc,2} + p_{in,2}$, respectively, and the phase difference between the measurements as $\Delta\phi = \phi_1 - \phi_2$.

The radius of the hard cylinder is chosen to be that of the Remote Environmental Monitoring Units (REMUS) 100 Autonomous Underwater Vehicle (AUV). A REMUS 100 is used in our model due to its non-tapered profile with a large length to diameter (*L*/*D*) ratio of 8.4 with a length of 160 cm and radius of 9.5 cm [51]. The AUV is in seawater with a constant sound speed c = 1500 m/s in the presence of a monochromatic acoustic source of cylindrical waves at a distance b from the center of the cylinder emitting at the frequency f = 250 Hz. Based on the parameters chosen, the wavelength λ = 6.0 m and ka = 0.0995. The source will be restricted to the upper half-plane, $\theta = [0, \pi]$, for simplicity, due to the symmetry of the problem.

In this section, the angle θ characterizes the position of the sound source rather than the receiver and it has a different geometric meaning than in Sections II.B-D. However, for the receiver at $(a, 0)$ θ still is the angle between azimuthal directions from the cylinder axis to the source and to the receiver. Hence, the previously derived solutions can be used unchanged when calculating P_2. For the calculation of the acoustic pressure field P_1 at the receiver at (a, π), $\pi - \theta$ should be substituted for θ in the previously derived equations.

Bearing estimation for this model is inherently difficult. Geometrically, for the frequency chosen, it is a small array in the sense that there are only two array elements and the element spacing is small compared to the wavelength. Both factors contribute to relatively small measured differences in amplitude and phase between the array elements, and realistically these small difference quantities are subject to distortion by noise. Additionally, the acoustic field is strongly distorted in the presence of the cylinder, especially in the proximity of the cylinder, and in this model the receivers are placed on the surface of the cylinder. Since the source strength is unknown, the information available for bearing estimation is contained in the relative change of the sum and difference of the complex fields at the receivers. From Eqs. (2.7), (2.8), and (2.20), it follows that the effect of bearing variation on the relative change in the sum is of order $1 + O\left(\kappa^2 (ka)\right)$ with and without the cylinder since $p_{in,1} + p_{in,2} = 2H_0^{(1)}(kb) + O\left(k^2 a^2\right)$ and

$P_1 + P_2 = 2H_0^{(1)}(kb) + O\left(\kappa^2(ka)\right)$, provided $b >> a$. Hence, the sum of the measured pressures is essentially unaffected by bearing variations. When $b >> a$, the relative change in the difference is $2 + O\left(k^2a^2\right)$ since, according to Eqs. (2.7), (2.8), and (2.20), $p_{in,1} - p_{in,2} = -2kaH_1^{(1)}(kb)\cos\theta + O\left(k^3a^3\right)$ and $P_1 - P_2 = -4kaH_1^{(1)}(kb)\cos\theta + O\left(k^3a^3\right)$, in the free space and in the presence of the cylinder, respectively. These physical considerations indicate that the cylinder itself helps to increase bearing resolution over the free space solution.

Noise was added to the model to evaluate bearing estimation in a more realistic setting of noisy measurements. Additive and incoherent Gaussian noise with a magnitude of N percent of the incident field pressure p_{in} at the center of the cylinder was introduced to each receiver signal in the form $\tilde{P}_i = P_i + \left|H_0^{(1)}(kb)\right|\left(X_i + iY_i\right)N/100$. Here X_i and Y_i are independent Gaussian random variables with zero mean and unit variance. N was chosen to be 3 for all simulated measurements. For the bearing inverse solutions that follow, 50 samples per angle, over 91 equally spaced angles in the upper half-plane were averaged. An effective signal-to-noise ratio (SNR) was calculated since the bearing information is contained in the small difference of complex amplitudes (or phases) of two measured fields. The effective SNR was calculated as

$$SNR_{dB}^{EFF} = 20\log_{10}\left[\frac{100}{\sqrt{2}N}\right] + 20\log_{10}\left|\frac{\sqrt{2}kaH_1^{(1)}(kb)}{H_0^{(1)}(kb)}\right|. \qquad (2.41)$$

All of the resulting models and numerical analysis were built and quantified through MATLAB.

1. Plane Wave Beamforming Solution

For a simple two element array in free space, the measured phase difference between elements $\Delta\phi \approx 2ka\cos\theta$ in the far field of the cylindrical wave source. Then, the inverse problem is easily solved and the estimated bearing is $\hat{\theta} = \cos^{-1}\left(\Delta\phi/2ka\right)$. When the receivers are mounted on the hard cylinder, the scattered wave greatly influences the complex field and, as shown above, the resulting measured phase difference doubles. For

all angles the measured phase difference is approximately $\Delta\phi_{CYL} \approx 4ka\cos\theta \approx 2\Delta\phi_{FS}$. Thus, the effect of the cylinder is similar to doubling the array element separation. With this understanding, the plane wave beamforming model can still be used for mounted receivers. Figure 5 shows the results of bearing estimation with plane wave beamforming for three source distances that represent near and intermediate source ranges of interest.

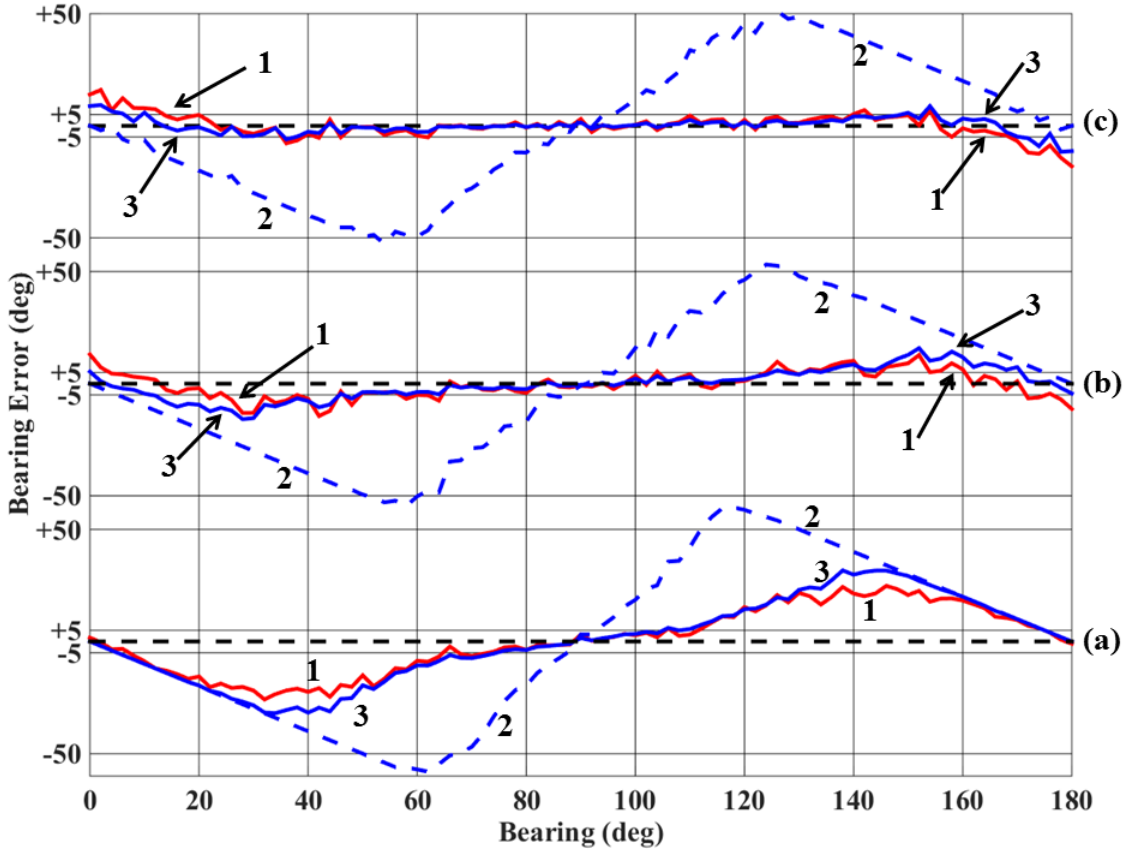

Figure 5. Plane wave beamforming bearing estimation for mounted receivers at various source ranges. Bearing solutions are shown for the free space (curves labeled 1), in the presence of the hard cylinder without corrections due to scattering (2), and in the presence of the hard cylinder with scattered wave taken into account (3) for a cylindrical wave source at a range of $b = 3a$ (a), $b = 10a$ (b), and $b = 100a$ (c).

2. Matched Field Processing Solution

A simple matched field processing technique was employed using knowledge of the scattered field due to a hard cylinder, Eq. (2.39), in which the scattered field is approximately represented as the sum of three acoustic image line sources. Aside from noise, the measured field at each receiver is then due to four line sources. Figure 2 and Figure 4 indicate that, for ka =0.0995 considered, the relative asymptotic error is small, and use of the uniform asymptotic makes a negligible contribution to error in the bearing determination. Bearing was found by minimizing the following cost function

$$f(b,\theta) = \left| P_1 / P_2 - \tilde{P}_1 / \tilde{P}_2 \right|^2 ,$$

with respect to b and θ. Here P_i is the total field modeled for a given source position as a sum of fields of 4 line sources, and $\tilde{P}_i$ represents the measured complex field at each receiver. The measured field was calculated using the exact expression Eq. (2.8) for the scattered wave and includes additive noise. Figure 6 shows the matched field processing solution for three source distances that represent near and intermediate source ranges of interest.

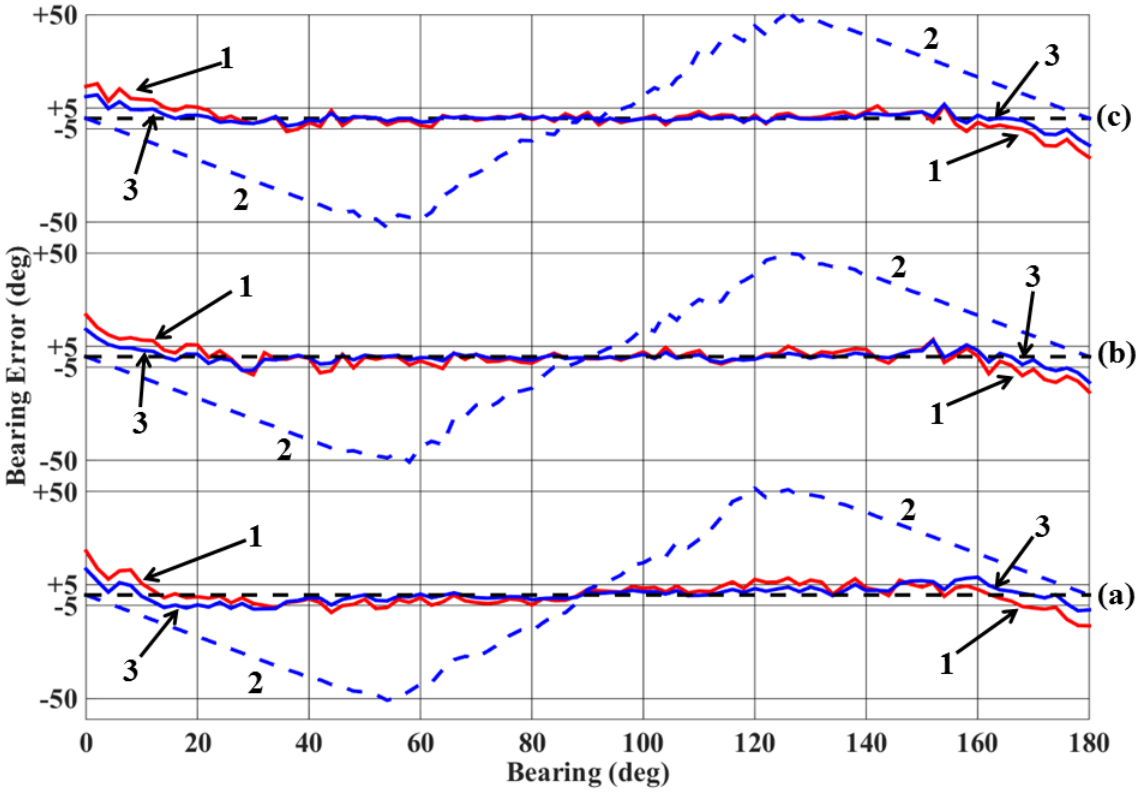

Figure 6. Matched field processing bearing estimation for mounted receivers at various source ranges. Bearing solutions are shown for the free space (curves labeled 1), in the presence of the hard cylinder without corrections due to scattering (2), and in the presence of the hard cylinder with scattered wave taken into account (3) for a cylindrical wave source at a range of $b = 3a$ (a), $b = 10a$ (b), and $b = 100a$ (c).

3. Analysis of Results

Results of bearing estimation using plane-wave beamforming are shown in Figure 5. As to be expected, the bearing error gets smaller as the source gets further away from the scatterer. The figure also illustrates the significance of a physical understanding of the scattering process for an efficient use of mounted receivers. As Figure 5 clearly shows, scattering theory-based modification of the plane-wave allows for recovery of the bearing estimation using mounted receivers with the same accuracy as if the cylinder was not present.

Figure 6 illustrates results of bearing estimation using matched field processing. This method proves to be superior to the plane-wave beamforming method over a wide range of source distances. Much like in the case of plane-wave beamforming, account for and accurate description of the scattered wave are necessary to recover bearing estimates using mounted receivers. With the scattered field described by the uniform asymptotic Eq. (2.39), accuracy of bearing estimation using mounted receivers appears to be systematically better than in the absence of the cylinder.

To further quantify the bearing errors depicted in Figure 5 and Figure 6, the Root Mean Square Error (RMSE) was computed over all angles using the following standard definition, $RMSE = \sqrt{\sum_{i=1}^{n}\left(\hat{\theta}_i - \theta_i\right)^2 \Big/ n}$, where θ_i is the true source bearing, $\hat{\theta}_i$ is the average estimated source bearing over the 50 samples, and *n* is the number of source angles. Results of this calculation over the complete data sets represented in Figure 5 and Figure 6 are given in Table 1. Results in the absence of the cylinder are marked "Free Space." For mounted receivers, processing results with and without accounting for the field distortion by the cylinder are marked "Cylinder-Uncorrected" and "Cylinder-Corrected," respectively.

Table 1 indicates that no adequate results can be obtained (assuming $ka \ll 1$) with mounted hydrophones unless the scattered wave field is properly taken into account. Both the plane-wave beamforming and matched field processing require *a priori* knowledge about the physics of the scattered wave due to a cylinder to make meaningful bearing estimates. The implementation of the matched field processing technique with the uniform asymptotic Eq. (2.39) gave superior results when compared with plane wave beamforming, even at relatively large source ranges. Furthermore, when the matched field processing method is employed, mounted hydrophones perform better than hydrophones in the free space. We attribute the gain in accuracy primarily to the effective SNR being roughly 6 dB higher as a result of the larger measured phase difference. A similar conclusion that scattering by an AUV's body improves source localization with hydrophones mounted on the AUV, was previously made [45] in a high-frequency regime and in a geometry different from the one we consider.

Table 1. Root mean square error (RMSE) in degrees for plane wave beamforming (PW) and matched field processing (MFP) bearing estimation at near and intermediate source ranges.

	$b = 3a$			$b = 10a$			$b = 100a$		
	RMSE		Eff.	RMSE		Eff.	RMSE		Eff.
	PW	MFP	SNR_{dB}	PW	MFP	SNR_{dB}	PW	MFP	SNR_{dB}
Free Space	14.5	5.7	15.6	5.9	5.5	11.7	5.3	5.5	10.4
Cylinder-Uncorrected	35.1	30.5	21.6	31.4	29.5	17.8	30.3	29.9	16.5
Cylinder-Corrected	18.1	3.9	21.6	6.7	3.3	17.8	3.6	3.3	16.5

Data collected is averaged over 50 samples per angle for noise, over 91 equally spaced angles.

F. CONCLUSION

Scattering of cylindrical waves by acoustically soft and hard cylinders within a homogenous medium has well known solutions in terms of infinite sums. The Green's function solutions take the form of the summation of both the incident cylindrical wave (2.1) and the resulting scattered (diffracted) wave (2.8). In this chapter, uniform asymptotic solutions (2.39) within the Rayleigh regime have been found for acoustically soft, hard, and impedance cylinders. The solutions are valid over the entire domain outside the cylinder to second order accuracy or greater with respect to *ka*, the dimensionless radius of the cylinder. The validity of the uniform asymptotic solutions and analytic estimates of their accuracy have been confirmed numerically by comparing the asymptotic and exact solutions. Being derived assuming $ka << 1$, the asymptotic solutions have proved to approximate the scattered wave field for *ka* values as large as 1.

The uniform asymptotic solutions of the scattered wave satisfy the Helmholtz equation exactly and have a rather simple and intuitive form as the field due to three image line sources. The asymptotic solutions Eq. (2.39) for the soft, hard, and impedance cylinders differ only by amplitudes of the image sources. The image sources are located within the cylinder. In Eq. (2.39) positions of the image sources are independent of sound frequency and the boundary conditions on the surface of the cylinder. Positions of two

image sources, at the center of the cylinder $(0,0)$ and at the point $\left(a^2/b,0\right)$, are determined uniquely and coincide with locations of image charges in corresponding electrostatic [35] and magnetostatic [36] problems. A third image source is necessary to ensure second-order accuracy of the asymptotic solutions for hard and impedance cylinders, and the position $\left(-a^2/2b,0\right)$ for the third line source was chosen in deriving Eq. (2.39).

A similar uniform asymptotic solution was developed for spherical acoustic wave scattering by a small sphere in Refs. [32] and [33]. In comparison to those findings, the waves scattered by a soft cylinder and a soft sphere are both reduced to fields due to discrete line and point sources, respectively. However, for the hard and impedance sphere, asymptotic solutions of the scattered field were found to be the superposition of fields due to a monopole source at the center of the sphere and dipoles linearly distributed along a line connecting the center of the sphere and the Kelvin inversion point $\left(a^2/b,0\right)$. In the case of the infinite cylinder, uniform asymptotic solutions for the hard and impedance boundary conditions prove to be much simpler than for the sphere and are given by the superposition of fields due to three line sources. These asymptotic solutions were found to be of acceptable error up to and including $ka \le 1$ which was not the case for the sphere.

The problem of bearing estimation using hydrophones mounted on a hard cylinder was considered as an example of application of the uniform asymptotic solutions. We illustrated how physical properties of the scattered wave, which are revealed by the asymptotic solutions, and the efficient representation of the acoustic field in terms of image sources, can be employed to improve the solution of inverse problems that involve low-frequency scattering by a cylinder. The improvements include an extension of plane wave beamforming to mounted receivers.

The physically intuitive form and mathematically simple representation of the scattered wave as a field due to a few image sources suggest a possible path forward in a number of low-frequency diffraction and scattering problems, where multiple scattering by simple shapes is encountered and analytical solutions are not readily available. Further research is required to establish whether efficient analytical or semi-analytical solutions of

such problems can be obtained in terms of image sources. Another avenue of further research is an extension of the theory developed in this chapter to Rayleigh scattering of cylindrical waves by homogeneous or radially inhomogeneous fluid or fluid-solid cylinders.

THIS PAGE INTENTIONALLY LEFT BLANK

III. SCATTERING OF LOW-FREQUENCY SOUND BY FLUID AND SOLID CYLINDERS

This chapter was previously submitted on January 16, 2018 and is currently under review as of May 23, 2018. The article is under review as [3]: Alexander B. Baynes and Oleg A. Godin, "Scattering of low frequency sound by fluid and solid cylinders," *Journal of Sound and Vibration*.

A. INTRODUCTION

Most typically sound scattering by circular cylinders has been studied for plane incident waves. The exact solution of the problem of a plane wave scattered by an infinite cylinder was obtained by Lowan et al. for fluid [28] and Faran for solid [29] targets. The solutions are given in terms of an infinite series of the products of Bessel functions. In a multitude of problems, the plane wave solution is not sufficient and the full Green's function of the problem, rather than the plane-wave and far-field approximations, becomes necessary [23], [38], [41], [44], [27]. The acoustic field due to a linear source parallel to the axis of a cylinder may be viewed as a two-dimensional (2-D) Green's function. The Green's function describes scattering of an incident cylindrical wave by the cylinder. A recent example of application of 2-D Green's functions is development of a diffraction-based technique for passive suppression of radiation of low-frequency noise in underwater waveguides [2]. In addition to situations where a sound source is located in the near field of the scatterer, knowledge of the Green's function is required when the separation distance from the scatterer to an interface or other obstacles is comparable to the linear dimensions of the scatterer itself [15], [19]–[22].

Wave scattering by objects that are small relative to the wavelength is commonly referred to as Rayleigh scattering. Rayleigh scattering is studied in various branches of wave physics [7]–[9] and is of particular practical interest in acoustics [52]–[54], especially in underwater acoustics [55]–[57]. The distinct physics of low-frequency scattering allows

for a considerable reduction in complexity in the mathematical description of the Green's function. Derivation of simple and accurate closed-form approximations of the 2-D Green's function at scattering from a circular cylinder within the Rayleigh regime is the goal of this work.

In this chapter, we consider Rayleigh scattering of a cylindrical wave by a fluid or solid cylindrical obstacle. Recently an analytic approach was developed to approximate the acoustic Green's function in the Rayleigh regime. The approach utilized the method of matched asymptotic expansions to establish uniform asymptotic solutions for the diffraction of a monochromatic spherical sound wave by small soft, hard, impedance, and homogeneous fluid spherical targets [32], [33]. The method was also applied to establish solutions for monochromatic cylindrical wave scattering by infinite soft, hard, and impedance cylindrical targets [1]. These solutions offer a mathematically simple and intuitive representation of the scattered field as the field due to "image sources" located within the object.

Image source solutions were anticipated based on classical elementary solutions to problems in electrostatics and magnetostatics involving spheres and cylinders in the presence of point and line charges, respectively [35], [36], [58]–[60]. Of the static solutions, the best-known is Lord Kelvin's solution [34] for the electric field of a point charge in the presence of a grounded perfectly electrically conducting sphere. Here, we extend the asymptotic solutions for scattering of cylindrical acoustic waves, which were previously established for the soft, impedance, and hard cylinders, to the more realistic cases of fluid and solid cylindrical obstacles. Soft and hard boundary conditions correspond to pressure release and acoustically rigid surfaces, respectively, and the impedance boundary condition represents a linear combination of both soft and hard boundary conditions for modeling of more complex material scatterers (see Eqs. (4)–(6) from [1]). Importantly, none of this accounts for wave propagation within the target and as a result only provide first-order approximations to the scattering physics that are described by real fluid and solid material targets. The new uniform asymptotic solutions for fluid and solid scatterers are valid in the Rayleigh regime and describe the scattered field everywhere outside of the cylinder for arbitrary positions of the sound source.

Image source solutions provide physical insights into scattering problems and are extremely easy to implement. They offer a promising way forward to simplify the complex mathematics that arises in inverse problems [2] as well as in multiple-scattering problems where the exact Green's function is not readily available [15]–[18].

This chapter is organized as follows. In Section III.B, the known exact solution to the problem of cylindrical wave scattering by an infinite cylinder is presented. We establish a uniform asymptotic solution for the scattered wave specific to the Rayleigh scattering regime in Section III.C. In Section III.D, the accuracy of the uniform asymptotic solution is numerically confirmed. Resonance scattering of sound by infinite cylinders is investigated in Section III.E. In Section III.F, the asymptotic solution is utilized to explore scalar and vector energy characteristics of the acoustic field in the vicinity of a target. Finally, Section III.G is a summary of our conclusions.

B. THEORETICAL BACKGROUND

In this scattering problem, an incident monochromatic cylindrical wave of frequency ω emanating from an infinite line source is scattered by inviscid fluid and elastic solid cylinders of radius *a*. A cylindrical coordinate system (r,θ,z) is determined where the center of the infinite cylinder coincides with the *z*-axis. The source runs parallel to the axis of the cylinder and both are embedded in a homogenous fluid with sound speed *c*, density ρ, and acoustic wavenumber $k=\omega/c$, where *c*, ρ, and *k* correspond to ambient values for the surrounding fluid outside of the scatterer. Since the pressure is independent of the *z*-coordinate, the complete description of the scattering problem can be equivalently expressed as a two-dimensional problem using the polar coordinate system consisting of the coordinates (r,θ). Cartesian coordinates are defined by $x=r\cos\theta$ and $y=r\sin\theta$ with the origin of the coordinate system coinciding with the center of the cylinder. The linear sound source is located at $r = b$, $\theta = 0$.

The acoustic pressure in the incident cylindrical wave can be compactly expressed as

$$p_{in}=H_0^{(1)}\left(kR(b)\right),\ R(x_0)=\sqrt{(x-x_0)^2+y^2}\ , \tag{3.1}$$

where the $\exp(-i\omega t)$ time dependence is assumed and suppressed. The total acoustic pressure *p* is the sum of the incident (p_{in}) and scattered (p_{sc}) pressure fields, $b > a$ is the distance from the linear source to the center of the cylinder, $R(x_0)$ is the distance between points $(x_0, 0)$ and (x, y), and $H_0^{(1)}(q)$ is the Hankel function of the first kind of 0th order (see Figure 7). The Hankel functions of the first kind of order *n*, $H_n^{(1)}(q) = J_n(q) + iY_n(q)$, are the linear combinations of the Bessel function $J_n(q)$ and the Neumann function $Y_n(q)$ [49]. The Hankel functions have the convenient large argument asymptotic form [49],

$$H_n^{(1)}(q) \sim \sqrt{2/\pi q}\exp(iq - in\pi/2 - i\pi/4),\ |q| >> 1,\ -\pi < \arg q < 2\pi, \qquad (3.2)$$

representing outgoing plane waves.

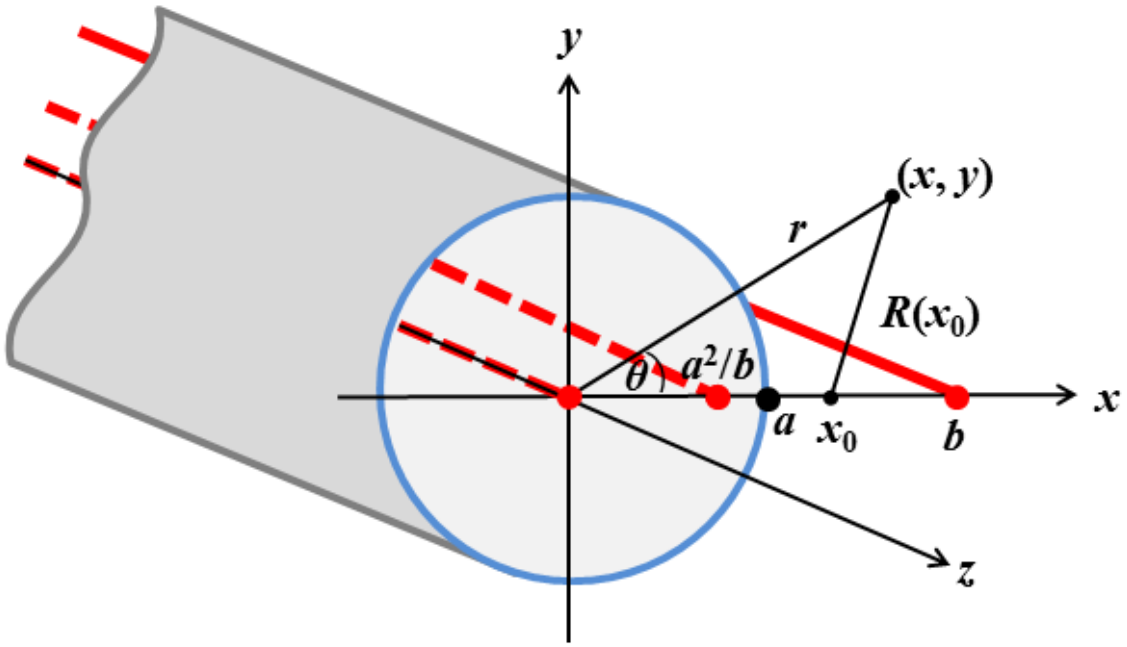

Figure 7. Geometry for the cylindrical scattering problem. Depicted is an infinite cylindrical scatterer of radius a with axis at (0, 0, z) running parallel to an acoustic line source (solid line) located at coordinates (b, 0, z), with field observation point located at (x, y, z). Additionally shown are two image acoustic line sources (dashed line) located within the cylinder at coordinates (0, 0, z) and (a^2/b, 0, z). The distance R is formally defined in Eq. (3.1) and employed from Eq. (3.35) onward.

Outside of the cylinder, the acoustic pressure p_{sc} in the scattered wave satisfies the two-dimensional homogeneous Helmholtz equation,

$$\nabla^2 p_{sc} + k^2 p_{sc} = 0, \quad r > a\,. \tag{3.3}$$

Both the incident and scattered fields can be expressed in terms of cylindrical functions [14],

$$p_{in} = \sum_{n=0}^{\infty} \varepsilon_n H_n^{(1)}\left(kr_>\right) J_n\left(kr_<\right) \cos n\theta, \quad r_> = \max\left(r,b\right), \quad r_< = \min\left(r,b\right), \tag{3.4}$$

$$p_{sc} = -\sum_{n=0}^{\infty} \varepsilon_n A_n H_n^{(1)}\left(kb\right) H_n^{(1)}\left(kr\right) \cos n\theta, \quad r \geq a\,. \tag{3.5}$$

Symmetry of the problem dictates that an incident cylindrical wave with $\cos n\theta$ azimuthal dependence generates a scattered cylindrical wave and a wave field inside the target with the same azimuthal dependence. We will refer to wave field components with $\cos n\theta$

azimuthal dependence as partial waves. In Eq. (3.5), ε_n is the Neumann symbol ($\varepsilon_0 = 1$; $\varepsilon_n = 2$ for $n \geq 1$) and the A_n coefficients describe amplitudes of individual partial waves that are determined by the boundary conditions at the surface of the cylinder, $r = a$.

1. Fluid Cylinder

For the fluid scatterer, let p_F be the total pressure within the cylinder $r < a$, composed of a homogenous inviscid fluid with mass density $\rho_F = M_F \rho$, sound speed $c_1 = sc$, and acoustic wave number $k_1 = \omega / c_1$. M_F and s are dimensionless material parameters. The subscript "*F*" denotes quantities for the fluid scatterer to differentiate from the elastic solid (subscript "*ES*") results to come.

The acoustic (compressional) wave within the scatterer satisfies the two-dimensional homogeneous Helmholtz equation,

$$\nabla^2 p_F + k_1^{\,2} p_F = 0, \quad r < a \ . \tag{3.6}$$

The compressional wave within the cylinder then can be expressed in terms of cylindrical harmonics,

$$p_F = \sum_{n=0}^{\infty} \varepsilon_n D_n^{(F)} H_n^{(1)}(kb) J_n(k_1 r) \cos n\theta, \quad r \leq a \,, \tag{3.7}$$

where the $D_n^{(F)}$ coefficients represent undetermined complex amplitudes of partial waves. Here the superscript "*F*" denotes quantities corresponding to the fluid scatterer. The boundary conditions for the fluid-fluid interface are [61],

$$p_F = p_{in} + p_{sc}^{(F)}, \quad \frac{\partial p_F}{\partial r} = M_F \left(\frac{\partial p_{in}}{\partial r} + \frac{\partial p_{sc}^{(F)}}{\partial r} \right), \quad r = a \,. \tag{3.8}$$

Substitution of Eqs. (3.4), (3.5), and (3.7) into (3.8), with the Wronskian $H_n^{(1)\prime}(ka) J_n(ka) - H_n^{(1)}(ka) J_n'(ka) = 2\mathrm{i}/\pi ka$ from [49] yields,

$$A_n^{(F)} = \frac{M_F s J_n'(ka) J_n(k_1 a) - J_n(ka) J_n'(k_1 a)}{M_F s H_n^{(1)\prime}(ka) J_n(k_1 a) - H_n^{(1)}(ka) J_n'(k_1 a)}, \tag{3.9}$$

$$D_n^{(F)} = \frac{2\mathrm{i} M_F s / (\pi ka)}{M_F s H_n^{(1)\prime}(ka) J_n(k_1 a) - H_n^{(1)}(ka) J_n'(k_1 a)}. \tag{3.10}$$

Here and below the prime denotes the derivative of the function with respect to its argument. Equations (3.9) and (3.10) are independent of the incident wave type. To check the validity of the solution, let $M_F = s = 1$, i.e., there is no contrast in acoustic parameters across the boundary $r = a$. Then the coefficients reduce to $A_n^{(F)} = 0$ and $D_n^{(F)} = 1$ in Eqs. (3.9) and (3.10), respectively. Hence, there is no scattered field ($p_{sc}^{(F)} = 0$) and the field within the scatterer is exactly the incident field ($p_F = p_{in}$), both of which are expected for a homogenous field. Additionally, in the limit $M_F \to 0$, the soft cylinder scattered amplitudes: $A_n^{(S)} = J_n(ka) \big/ H_n^{(1)}(ka)$ [33] are recovered, and in the limit $M_F \to \infty$, the hard cylinder scattered amplitudes: $A_n^{(H)} = J_n'(ka) \big/ H_n^{(1)\prime}(ka)$ [33] are also reproduced. The soft (*S*) boundary condition describes a cylinder with a pressure release surface at $r = a$, and the hard (*H*) boundary condition describes a cylinder where the particle velocity normal to the cylinder's surface is zero at $r = a$. Substitution of Eq. (3.9) into (3.5) gives the exact solution for scattering (diffraction) of a cylindrical wave by a homogenous inviscid fluid cylinder.

2. Solid (Elastic) Cylinder

Let the scatterer at $r \le a$ be composed of an isotropic elastic solid with mass density $\rho_{ES} = M_{ES}\rho$ and Lamé elastic constants λ and μ. Here, the subscript "*ES*" (and later superscript) pertain to quantities associated with the solid scatterer. The waves inside the elastic medium satisfy the following equation of motion for the displacement (**u**) [62],

$$(\lambda + 2\mu)\nabla(\nabla \cdot \mathbf{u}) - \mu\nabla \times (\nabla \times \mathbf{u}) = \rho_{ES}\, \partial^2 \mathbf{u} \big/ \partial t^2 , \tag{3.11}$$

where the Lamé parameters are related to the Young's modulus E and the Poisson ratio σ by the following equations,

$$\lambda = \frac{\sigma E}{(1+\sigma)(1-2\sigma)}, \quad \mu = \frac{E}{2(1+\sigma)}. \tag{3.12}$$

An approach to a solution to Eq. (3.11) and ultimately the developed scattered amplitudes for the scattered wave was shown in the classical paper by Faran [29] for plane wave scattering by elastic solid cylinders. Inside the solid, two waves propagate: longitudinal

compressional waves and transverse shear waves with sound speeds $c_1 = s_1 c$ and $c_2 = s_2 c$, and wave numbers $k_1 = \omega/c_1$ and $k_2 = \omega/c_2$, respectively. In our problem due to cylindrical wave incidence, to develop the scattered field coefficients ($A_n^{(ES)}$), the scattered, compressional, and shear waves are expressed in terms of cylindrical functions to most conveniently satisfy the boundary conditions [29] at the fluid-solid interface ($r = a$): (I) normal stress component of the solid is equal to pressure in the fluid; (II) radial (normal) component of particle displacement in the solid and fluid must be equal; (III) solid shearing stress (tangential) components vanish at the surface. The steps to develop the coefficients are shown in detail in Appendix A for completeness and because the form of the coefficients presented are different than that of Faran [29]. The resulting equations for the $A_n^{(ES)}$ coefficients for the scattered wave in Eq. (3.5) are

$$A_n^{(ES)} = \frac{J_n(ka) - \eta_n J_n'(ka)}{H_n^{(1)}(ka) - \eta_n H_n^{(1)\prime}(ka)}, \tag{3.13}$$

where

$$\eta_n = \frac{1}{\rho c^2 ka} \times \begin{cases} \dfrac{2\mu J_n'(k_1 a) + (2\mu + \lambda) k_1 a J_n(k_1 a)}{J_n'(k_1 a)}, & n = 0 \\ \dfrac{\left[\lambda J_n(k_1 a) - 2\mu J_n''(k_1 a)\right] k_1^2 a^2 \Gamma_n + 2\mu n\left(k_2 a J_n'(k_2 a) - J_n(k_2 a)\right)}{k_1 a J_n'(k_1 a)\Gamma_n - n J_n(k_2 a)}, & n > 0 \end{cases}$$

and

$$\Gamma_n = \frac{n^2 J_n(k_2 a) - k_2 a J_n'(k_2 a) + (k_2 a)^2 J_n''(k_2 a)}{2n\left[k_1 a J_n'(k_1 a) - J_n(k_1 a)\right]}.$$

Inspection of Eq. (3.13) shows that when $c_2 = 0$, $k_2 \to \infty$, and $\mu = 0$, the scattering amplitudes reduce to that of Eq. (3.9), hence, the scattering amplitudes for an inviscid fluid are reproduced.

C. DERIVATION OF THE ASYMPTOTIC SOLUTIONS FOR THE SCATTERED WAVE

In the derivation of the scattered wave asymptotic solution, we consider only the scattering problem within the Rayleigh regime throughout. For the fluid, this corresponds to

$$ka << 1, \quad k_1 a << 1, \tag{3.14}$$

and for the solid, when,

$$ka << 1, \quad k_1 a << 1, \quad k_2 a << 1. \tag{3.15}$$

To derive a uniform asymptotic solution for the scattered field that is valid everywhere outside the cylinder $(r, b \geq a)$, we first simplify the A_n coefficients in the Rayleigh regime, then develop an inner asymptotic solution (when the sound source and receiver are close to the scatterer) and an outer asymptotic solution (when the sound source and receiver, or both, are far from the scatterer), and lastly through the technique of matched asymptotic expansions bridge the two local asymptotic solutions to form a uniform solution.

1. Small Argument Approximation and Recursion Relationships for Bessel Functions

Small argument expressions for Bessel and Hankel functions of the first kind and their derivatives [49],

$$J_0(q) = 1 - q^2/4 + O(q^4), \quad J_0'(q) = -J_1(q), \tag{3.16}$$

$$\begin{aligned} J_n(q) &= \frac{1}{n!}\left(\frac{q}{2}\right)^n \left(1 - \frac{1}{n+1}\left(\frac{q}{2}\right)^2\right) + O\left(q^{n+4}\right), \quad n = 1,\ 2,\ 3,..., \\ J_n'(q) &= \frac{1}{2}\frac{1}{(n-1)!}\left(\frac{q}{2}\right)^{n-1} \left(1 - \frac{n+2}{n(n+1)}\left(\frac{q}{2}\right)^2\right) + O\left(q^{n+3}\right), \quad n = 1,\ 2,\ 3,..., \end{aligned} \tag{3.17}$$

$$H_0^{(1)}(q) = 1 + \left(\ln(q/2) + \gamma\right)2i/\pi + O\left(\kappa^2(q)\right), \quad H_0^{(1)\prime}(q) = -H_1^{(1)}(q), \tag{3.18}$$

$$\begin{aligned} H_n^{(1)}(q) &= -\frac{i(n-1)!}{\pi}\left(\frac{2}{q}\right)^n \left[1 + O\left(\kappa^2(q)\right)\right], \quad n = 1,\ 2,\ 3,..., \\ H_n^{(1)\prime}(q) &= \frac{in!}{2\pi}\left(\frac{2}{q}\right)^{n+1} \left[1 + O\left(\kappa^2(q)\right)\right], \quad n = 1,\ 2,\ 3,..., \end{aligned} \tag{3.19}$$

will be used in the asymptotic solution's derivation. Here and below, for brevity, the notation $\kappa^2(q) = q^2\left(1+\left|\ln q\right|\right)$ is adopted and $\gamma = 0.5772157...$ is Euler's constant. Higher-order terms in Eqs. (3.16)–(3.19) are required for analysis of certain special cases that are discussed in Section III.C.2 and Appendix B.

2. Scattered Amplitudes in the Rayleigh Regime

a. $A_n^{(F)}$ *Coefficients for Fluid Scatterer*

Under condition (3.14), substitution of Eqs. (3.16) and (3.18) into (3.9) yields

$$A_0^{(F)} = \frac{i\pi}{4}k^2a^2\left(\frac{M_F s^2 - 1}{M_F s^2}\right)\left[1 - \frac{i\pi}{4}\frac{k^2a^2}{M_F s^2}\left(1 + \frac{2i}{\pi}\left(\ln\left(\frac{ka}{2}\right) + \gamma\right)\right)\right]^{-1} \times \left[1 + O\left(k_1^2a^2 + \kappa^2(ka)\right)\right], \tag{3.20}$$

when $M_F s^2 \neq 1$. Under the additional constraint

$$M_F s^2 >> k^2a^2, \tag{3.21}$$

Eq. (3.20) simplifies to

$$A_0^{(F)} = \frac{i\pi}{4}k^2a^2\chi^{(F)}\left[1 + O\left(k_1^2a^2 + \kappa^2(ka)\right)\right], \qquad \chi^{(F)} \equiv \frac{M_F s^2 - 1}{M_F s^2} = \frac{\rho_F c_1^2 - \rho c^2}{\rho_F c_1^2}, \tag{3.22}$$

where $\chi^{(F)}$ is a measure of the relative difference in compressibility of the outer and inner fluids [33]. When $n \geq 1$, substitution of Eqs. (3.17) and (3.19) into (3.9) yields

$$A_n^{(F)} = -i\pi\frac{1}{n!(n-1)!}\left(\frac{ka}{2}\right)^{2n}\left[\frac{M_F - 1}{M_F + 1}\right] \times \left[1 + O\left(k_1^2a^2 + \kappa^2(ka)\right)\right],\ n = 1,\ 2,... \tag{3.23}$$

when $M_F \neq 1$. Equations (3.22) and (3.23) agree with [52]. Note the degenerate cases that arise when $M_F s^2 = 1$ or $M_F = 1$, which affect the $A_0^{(F)}$ and $A_{n\geq 1}^{(F)}$ coefficients, respectively. These specific cases and their implications for the scattered field are discussed in Appendix B.1.

b. $A_n^{(ES)}$ ***Coefficients for Solid Scatterer***

Under condition (3.15), substitution of Eqs. (3.16) and (3.18) into (3.13) yields

$$A_0^{(ES)} = \frac{i\pi}{4}k^2a^2\left(\frac{M_{ES}\left(s_1^2-s_2^2\right)-1}{M_{ES}\left(s_1^2-s_2^2\right)}\right)\times$$
$$\left[1-\frac{i\pi}{4}\frac{k^2a^2}{M_{ES}\left(s_1^2-s_2^2\right)}\left(1+\frac{2i}{\pi}\left(\ln\left(\frac{ka}{2}\right)+\gamma\right)\right)\right]^{-1}\left[1+O\left(k_1^2a^2+\kappa^2\left(ka\right)\right)\right], \tag{3.24}$$

when $M_{ES}\left(s_1^2-s_2^2\right)\neq 1$. Under the additional constraint

$$M_{ES}\left(s_1^2-s_2^2\right) >> k^2a^2, \tag{3.25}$$

Eq. (3.24) simplifies to

$$A_0^{(ES)} = \frac{i\pi}{4}k^2a^2\chi^{(ES)}\left[1+O\left(k_1^2a^2+\kappa^2\left(ka\right)\right)\right],$$
$$\chi^{(ES)} \equiv \frac{M_{ES}\left(s_1^2-s_2^2\right)-1}{M_{ES}\left(s_1^2-s_2^2\right)} = \frac{\rho_{ES}\left(c_1^2-c_2^2\right)-\rho c^2}{\rho_{ES}\left(c_1^2-c_2^2\right)}. \tag{3.26}$$

Inspection of Eqs. (3.24) and (3.26) show that the leading order term for the solid and fluid differ only in the quantities $M_{ES}\left(s_1^2-s_2^2\right)$ and $M_F s^2$, respectively.

When $n\geq 1$, substitution of Eqs. (3.17) and (3.19) into (3.13), yields

$$A_n^{(ES)} = -i\pi\frac{1}{n!(n-1)!}\left(\frac{ka}{2}\right)^{2n}\frac{4M_{ES}n(n-1)-\left(M_{ES}-1\right)\left(k_2a\right)^2}{4M_{ES}n(n-1)-\left(M_{ES}+1\right)\left(k_2a\right)^2}, \quad n\geq 1, \tag{3.27}$$

when $M_{ES}\neq 1$.

Allowing $c_2 = 0$ then $s_2 = 0$ and $k_2 \to \infty$, while other parameters remain fixed, then Eqs. (3.24), (3.26), and (3.27) reduce exactly to the fluid coefficients represented in Eqs. (3.20), (3.22), and (3.23), respectively. Consider another special case, where

$$k_2^2a^2 << M_{ES}. \tag{3.28}$$

This is a rather weak assumption in light of (3.15) and various known material solid densities relative to, e.g., water or air. Then Eq. (3.27) reduces to the following two equations,

$$A_1^{(ES)} = A_1^{(F)} = -\frac{i\pi}{4}k^2a^2\left[\frac{M_{ES}-1}{M_{ES}+1}\right] \times\left[1+O\left(\left(k_1^2+k_2^2\right)a^2+\kappa^2\left(ka\right)\right)\right], \tag{3.29}$$

$$A_n^{(ES)} = -i\pi\frac{1}{n!(n-1)!}\left(\frac{ka}{2}\right)^{2n}\left[1+O\left(k_2^2a^2/M_{ES}\right)\right] = A_n^{(H)}\left[1+O\left(k_2^2a^2/M_{ES}\right)\right],\ \ n\geq 2. \tag{3.30}$$

Here, $A_n^{(H)}$ are the coefficients for the acoustically hard cylinder case, which was analyzed in [1]. In the Rayleigh regime, consequently, under condition (3.28) the scattering problem for an elastic cylinder can be readily solved by replacing only the first two terms of the hard cylinder solution if already computed, which was investigated in [1].

Inspection of Eq. (3.29) shows that for $n=1$ the leading order term for solid and fluid differ only in the density ratios M_{ES} and M_F, respectively. And, additionally, through inspection of Eq. (3.30), for $n\geq 2$, the respective leading order term for the fluid coefficients are reproduced if the factor $\left(M_F-1\right)/\left(M_F+1\right)$ is multiplied through.

Note the degenerate cases that arise when $M_{ES}\left(s_1^2-s_2^2\right)=1$ or $M_{ES}=1$, which affect the $A_0^{(ES)}$ and $A_1^{(ES)}$ coefficients, respectively. Again, these specific cases and their implications for the scattered field are discussed in Appendix B.2. For the remainder of the manuscript, non-degenerate cases are assumed.

c. Rayleigh Coefficient Properties

The problem of cylindrical wave scattering (diffraction) by a fluid and solid cylinder is approximately solved in terms of an infinite sum over the entire domain for which $r,b\geq a$ through direct substitution of the derived coefficients in the Rayleigh approximation into (3.5). Both the fluid and solid cylinder A_0 and A_1 coefficients are of the same order in ka, namely, $A_0=A_1=O\left(k^2a^2\right)$, when $M_Fs^2=O(1)$ and $M_{ES}\left(s_1^2-s_2^2\right)=O(1)$, assuming non-degenerate cases, and so make equally dominant contributions to the scattered partial field. This result was also found in [1] for the hard

cylinder, unlike for the soft cylinder where the A_0 partial wave contribution to the scattered field was dominant.

For terms $n \geq 1$, the coefficients which represent scattered amplitudes of individual partial waves similarly share $(ka)^{2n}$ proportionality. Under the condition $ka << 1$, in the Rayleigh regime, the corresponding contribution by individual partial waves to the scattered field rapidly decreases in magnitude with respect to *n* in the infinite series for the scattered field (3.5).

However, unlike the soft and hard cylinders in [1], the fluid and solid A_0 coefficients have a complicated frequency dependence that can be seen in (3.20) and (3.24) by inspection of the denominator. Allowing for $M_F s^2 << 1$ and $M_{ES}\left(s_1^2 - s_2^2\right) << 1$ for a highly compressible fluid and solid scatterer, respectively, the relative magnitude of the A_0 corresponding partial wave contribution to the scattered field becomes dominant. The complex frequency dependence of the $A_0^{(F)}$ and $A_0^{(ES)}$ terms is further explored later in Section III.E.

3. Inner Asymptotic Solution

The inner asymptotic solution is defined as a solution, which describes Rayleigh scattering when

$$kb << 1, \quad kr << 1. \tag{3.31}$$

Development of the inner asymptotic solution is slightly different for the fluid and solid targets due to Eqs. (3.23) and (3.30) for the A_n coefficients being applicable at $n \geq 1$ and $n \geq 2$, respectively. Starting from Eq. (3.5) for the exact scattered field and using the small argument approximations (3.19) of the Hankel functions and the A_n coefficients in (3.23) and (3.30) under conditions (3.14), (3.15), and (3.31), we obtain

$$\begin{aligned} p_{sc}^{(F)} = -A_0^{(F)} H_0^{(1)}(kb) H_0^{(1)}(kr) + \frac{8}{\pi^2} \frac{A_1^{(F)}}{k^2 a^2} \sum_{n=1}^{\infty} \frac{1}{n} \left(\frac{a^2}{br}\right)^n \cos n\theta \times \\ \left[1 + O\left(\kappa^2(kb) + \kappa^2(kr)\right)\right], \end{aligned} \tag{3.32}$$

$$p_{sc}^{(ES)} = -A_0^{(ES)} H_0^{(1)}(kb) H_0^{(1)}(kr) - 2A_1^{(ES)} H_1^{(1)}(kb) H_1^{(1)}(kr)\cos\theta$$
$$-\frac{2i}{\pi}\sum_{n=2}^{\infty}\frac{1}{n}\left(\frac{a^2}{br}\right)^n \cos n\theta\left[1+O\left(\kappa^2(kb)+\kappa^2(kr)+k_2^2a^2/M\right)\right]. \tag{3.33}$$

Similarly, using (3.17) and (3.19), and the incident fields from Eqs. (3.1) and (3.4), under the same conditions, an incident field due to a line source located on the *x*-axis can be approximated as

$$p_{in} = H_0^{(1)}(kr_>)J_0(kr_<) - \frac{2i}{\pi}\sum_{n=1}^{\infty}\frac{1}{n}\left(\frac{r_<}{r_>}\right)^n \cos n\theta\left[1+O\left(\kappa^2(kr_>)\right)\right]. \tag{3.34}$$

Due to the structure of the incident and scattered fields, the infinite sums in Eqs. (3.32) and (3.33) are the same as in (3.34) if $r_> = r$ and $r_< = a^2/b$. Equation (3.34), using these values, where now $p_{in} = H_0^{(1)}\left(kR\left(a^2/b\right)\right)$, then allows direct replacement of the infinite series in (3.32) and (3.33) in terms of two sources, within the same order of accuracy,

$$p_{sc}^{(F)} = \left[\left\{-A_0^{(F)}H_0^{(1)}(kb) - \frac{4i}{\pi}\frac{A_1^{(F)}}{k^2a^2}J_0\left(k\frac{a^2}{b}\right)\right\}H_0^{(1)}(kr)\right.$$
$$\left.+\frac{4i}{\pi}\frac{A_1^{(F)}}{k^2a^2}H_0^{(1)}\left(kR\left(\frac{a^2}{b}\right)\right)\right]\times\left[1+O\left(\kappa^2(kb)+\kappa^2(kr)\right)\right], \tag{3.35}$$

$$p_{sc}^{(ES)} = \left[\left\{-A_0^{(ES)}H_0^{(1)}(kb) - J_0\left(k\frac{a^2}{b}\right)\right\}H_0^{(1)}(kr) + H_0^{(1)}\left(kR\left(\frac{a^2}{b}\right)\right)\right.$$
$$\left.-\left\{2A_1^{(ES)}H_1^{(1)}(kb) + 2J_1\left(k\frac{a^2}{b}\right)\right\}H_1^{(1)}(kr)\cos\theta\right] \tag{3.36}$$
$$\times\left[1+O\left(\kappa^2(kb)+\kappa^2(kr)+k_2^2a^2/M_{ES}\right)\right].$$

Equations (3.35) and (3.36) represent inner local asymptotic solutions for the scattered field which hold for arbitrary values of *a*, *b*, *r*, and θ under conditions (3.14), (3.15), and (3.31).

The inner asymptotic solutions satisfy the Helmholtz equation (3.3) exactly and approximates the exact scattered field in Eq. (3.5) within factors of $1+O\left(\kappa^2(kb)+\kappa^2(kr)\right)$ and $1+O\left(\kappa^2(kb)+\kappa^2(kr)+k_2^2a^2/M_{ES}\right)$. Both solutions depend only on the A_0 and A_1 coefficients and are composed of simple image sources, however,

their structure is different. The scattered wave due to a fluid cylinder reduces to the sum of two image line sources located at the origin and at the point $\left(a^2/b, 0\right)$. The coordinates of the latter share the same location as the Kelvin inversion point originating from the classical problem in electrostatics pertaining to the electrostatic potential due to a point charge in the presence of a grounded sphere [34]. Geometrically, the Kelvin inversion point has the property that $R(b) = (b/a)R\left(a^2/b\right)$ for every point on the surface of the cylinder, $r = a$. The fluid inner asymptotic solution (3.35) shares the same physical structure as previously found for soft, hard, and impedance cylindrical scatterers. The difference between different types of scatterers is encapsulated only in the values of the respective A_0 and A_1 scattering amplitudes. In the limits of $M_F = 0$ and $M_F \to \infty$, which represent the acoustically soft and hard boundary conditions, respectively, Eq. (3.35) reduces to the results derived in [1].

For the solid cylinder, due to the recursion relationship starting at $n = 2$ (vice $n = 1$) the scattered field inner asymptotic solution (3.36) reduces to the sum of 3 simple image sources: two line sources, with different complex amplitudes but at the same points as for the fluid and with the introduction of an additional dipole source located at the origin.

Equations (3.35) and (3.36) can further be evaluated in the limiting case of vanishing frequency, for which the wave number $k \to 0$ while the geometric $(a,\ b,\ r,\ \theta)$ and material parameters $(M,\ M_F,\ M_{ES},\ \rho,\ \rho_F,\ \rho_{ES},\ s,\ s_1,\ s_2)$ remain fixed. The scattered field in the static limit reduces to

$$\lim_{k\to 0} p_{sc}^{(F)} = \frac{2i}{\pi}\left[\frac{\rho_F - \rho}{\rho_F + \rho}\right]\left\{\ln R\left(\frac{a^2}{b}\right) - \ln r\right\} = \left[\frac{\rho_F - \rho}{\rho_F + \rho}\right] p_{sc}^{(H)}, \tag{3.37}$$

$$\begin{aligned}\lim_{k\to 0} p_{sc}^{(ES)} &= \frac{2i}{\pi}\left\{\ln R\left(\frac{a^2}{b}\right) - \ln r + \frac{a^2}{br}\left[1 - \frac{\rho_{ES} - \rho}{\rho_{ES} + \rho}\right]\cos\theta\right\} \\ &= p_{sc}^{(H)} + \frac{2i}{\pi}\frac{a^2}{br}\left[1 - \frac{\rho_{ES} - \rho}{\rho_{ES} + \rho}\right]\cos\theta,\end{aligned} \tag{3.38}$$

for the fluid and solid, respectively. The resulting stationary limits are exact solutions to Laplace's equation. In the static limit for a fluid, the solution is a scaled result of the

expression found for the hard cylinder [1]. And for the solid, the static solution has the same monopole terms as for the hard cylinder with added dipole directivity [1]. In both Eqs. (3.37) and (3.38), as ρ_F and ρ_{ES} tend to infinity, the stationary limit for the hard cylinder $p_{sc}^{(H)}$ is reproduced exactly.

The scattering by a fluid cylinder in acoustics has a direct electrostatic analog in the problem of an infinite electric line charge, embedded within a dielectric, running parallel to an uncharged dielectric cylinder with a different dielectric constant. In the stationary limit, the acoustic scattered field $p_{sc}^{(F)}$ exactly corresponds to the electrostatic potential of such an analog problem where the densities of the two fluids correspond to the respective dielectric constants. The stationary limit for fluid represented in (3.37), through inspection, reproduces the known electrostatic solution [58] exactly. In addition, taking the limit as $M_F = \rho_F / \rho \to \infty$ yields the static limit for the problem of a magnetic line charge outside a parallel grounded perfect electric conductor as shown in [1], [36], where in this case the pressure corresponds to the scalar magnetic field potential. From a fluid mechanics perspective, the pressure in Eq. (3.38) corresponds to the fluid velocity potential of a mass injection source in the presence of an elastic circular cylinder. The solution is composed of the static impenetrable cylinder solution [1], [50], containing a source and sink of equal magnitudes, as well as an additional dipole (source-sink pair), which describes the effect of the cylinder deformation on the fluid flow.

4. Outer Asymptotic Solution

The outer local asymptotic solution is developed under the imposed geometric condition that

$$\alpha \equiv a^2 / br << 1, \tag{3.39}$$

which corresponds to the source or receiver (or both) located a distance from the center of the scatterer that is large relative to *a*, the radius of the cylindrical scatterer. Within the domain of the outer local asymptotic solution, conditions (3.14) and (3.15) still are assumed to hold, however, condition (3.31) is no longer assumed. The exact scattered field (3.5) is composed of an infinite sum of $A_n H_n^{(1)}(kb) H_n^{(1)}(kr)$ products, and within the Rayleigh

regime from Eqs. (3.23), (3.29), and (3.30), the *n*th term is proportional to $(ka)^{2n} H_n^{(1)}(kb) H_n^{(1)}(kr)$ for $n \geq 1$, where $ka << 1$. The Hankel functions with arguments *kb* and *kr* are not necessarily small, however, through inspection of their limiting forms as a result of Eqs. (3.2) and (3.19), the upper bound of the *n*th term is proportional to a factor $\left(a^2/br\right)^n = \alpha^n$. Under condition (3.39), α is necessarily small, and so terms in the series (3.5) are proportional to α^n and decrease rapidly with increasing *n*. Through inspection, only the first three terms in the infinite series in (3.5) need to be retained to ensure second-order accuracy in α and *ka* since the $n = 3$ term differs from the $n = 1$ term by a factor $O\left(\alpha^2\right)$. Ultimately, within the Rayleigh regime under condition (3.39), the approximate scattered field is

$$\begin{aligned} p_{sc} = \Big\{ & -A_0 H_0^{(1)}(kb) H_0^{(1)}(kr) - 2A_1 H_1^{(1)}(kb) H_1^{(1)}(kr)\cos\theta \\ & -2A_2 H_2^{(1)}(kb) H_2^{(1)}(kr)\cos 2\theta \Big\} \times \left[1 + O\left(\alpha^2 + k^2 a^2\right)\right], \end{aligned} \tag{3.40}$$

and depends only on the first three A_n coefficients. The outer local asymptotic solution approximates the exact scattered field in Eq. (3.5) to a factor of $1 + O\left(\alpha^2 + k^2 a^2\right)$ and is an exact solution to the Helmholtz equation (3.3). This same result was found for the soft, hard, and impedance cylinders in [1].

5. Uniform Asymptotic Solution

The local asymptotic solutions obtained above have distinct domains of validity as explicitly expressed in conditions (3.31) and (3.39). However, the two domains of validity overlap and condition (3.39) is met when either of the inequalities in (3.31) is violated. Together, the local asymptotic solutions allow the computation of the scattered field at every point outside the scatterer within the Rayleigh regime. The inner local asymptotic solutions represented by Eqs. (3.35) and (3.36) approximate the exact scattered field to a factor of $1 + O\left(\kappa^2(kb) + \kappa^2(kr)\right)$ and $1 + O\left(\kappa^2(kb) + \kappa^2(kr) + k_2^2 a^2 / M_{ES}\right)$ for the fluid and solid scatterers, respectively. The outer asymptotic solution in (3.40) approximates the exact scattered field to a factor of $1 + O\left(\alpha^2 + k^2 a^2\right)$.

We wish to represent the scattered field everywhere outside the cylinder in one single and concise expression, subsuming the two local asymptotic solutions, while preserving overall second-order accuracy. As a result of the structure of the known inner solution in the solid target case (3.36) and the required number of terms from the outer solution in (3.40), assume an overall uniform asymptotic solution for the scattered wave as

$$P = B_0 H_0^{(1)}\left(kr\right) + B_1 H_0^{(1)}\left(kR\left(a^2/b\right)\right) + B_2 H_1^{(1)}\left(kr\right)\cos\theta\,. \tag{3.41}$$

The solution is the sum of a total of three terms: two image line sources and one dipole source. The B_i coefficients are constants and are unknown at this point. The proposed solution satisfies the Helmholtz equation exactly.

Using Graf's Addition Theorem [49],

$$H_0^{(1)}\left(kR\left(x_0\right)\right) = \sum_{m=-\infty}^{\infty} J_m\left(kx_0\right) H_m^{(1)}\left(kr\right)\cos m\theta\,, \tag{3.42}$$

we may write any line source not located at the origin in terms of a series of linear independent partial waves with amplitudes $J_m\left(kx_0\right)$. Using Eq. (3.42) with $x_0 = a^2/b$, under condition $ka << 1$, yields

$$\begin{aligned} H_0^{(1)}\left(kR\left(a^2/b\right)\right) &= J_0\left(ka^2/b\right) H_0^{(1)}\left(kr\right) + 2J_1\left(ka^2/b\right) H_1^{(1)}\left(kr\right)\cos\theta \\ &\quad + 2J_2\left(ka^2/b\right) H_2^{(1)}\left(kr\right)\cos 2\theta + O\left(\alpha^3 + \left(ka^2/b\right)^3 \Big/ \sqrt{kr}\right), \end{aligned} \tag{3.43}$$

which is an approximate expression for the image line source at the Kelvin point. Using Eq. (3.43), we can substitute the approximate partial wave representation of $H_0^{(1)}\left(kR\left(a^2/b\right)\right)$ into the uniform asymptotic (3.41) and set $P = p_{sc}$ from (3.40) without reducing the original accuracy of the approximation in (3.40). Linear independence of the partial waves leads to a system of 3 linear algebraic equations with 3 unknowns. The system of equations allows for the B_i coefficients to be exactly solved in terms of the known A_n coefficients without compromise of requisite second-order accuracy of the approximate solution. The coefficients are

$$B_0 = -A_0 H_0^{(1)}(kb) + A_2 \frac{H_2^{(1)}(kb)}{J_2\left(ka^2/b\right)} J_0\left(ka^2/b\right), \quad B_1 = -A_2 \frac{H_2^{(1)}(kb)}{J_2\left(ka^2/b\right)},$$
$$B_2 = -2A_1 H_1^{(1)}(kb) + 2A_2 \frac{H_2^{(1)}(kb)}{J_2\left(ka^2/b\right)} J_1\left(ka^2/b\right). \tag{3.44}$$

Substitution of the B_i coefficients into (3.41) allows exact replication of the expression within braces, the outer local asymptotic, in Eq. (3.40). Through inspection, under condition (3.31) for the fluid target, the amplitude of the B_2 coefficient tends to zero, while the terms B_0 and B_1 tend to the scattering amplitudes of the respective sources in Eq. (3.35). For the solid target, B_0, B_1, and B_2 tend to the scattering amplitudes of the respective sources in Eq. (3.36). Consequently, for both the fluid and solid under condition (3.31), P (3.41) reduces to the inner local asymptotic. Thus, Eq. (3.41) represents a second-order approximation of the scattered field (3.5) valid over the entire domain outside of the scatterer, $r, b \geq a$, and is a uniform asymptotic solution. The B_i scattering amplitudes are readily simplified in the Rayleigh regime through substitution of the derived approximate A_n coefficients and through the fact that $ka^2/b \leq ka << 1$. However, it was shown numerically that, for little extra computation, superior results over a wider range of ka values are acquired by using the exact A_n expressions for the B_i coefficients. The uniform asymptotic solution exactly reproduces the first three terms in the infinite series, and their respective angular independence, yielding a very accurate approximation of the scattered field.

An analysis shows that P represents a superior uniform asymptotic solution than those previously derived in [1] for soft, hard, and impedance cylinders. Numerical accuracy of the new uniform asymptotic solutions for the scattered field due to soft and hard cylinders is discussed in Appendix C.

Classically, sound scattering by cylinders has been usually studied for plane incident waves (see Lowan, et al. for fluids [28] and Faran for solids [29]). For comparison with those results, the asymptotic solution in (3.41) can be readily evaluated in the plane wave limit. Through use of Eq. (3.2) and allowing $b \to \infty$, we may write the equation for a plane wave in terms of a cylindrical wave Eq. (3.1):

$e^{-ikx} = \lim_{b\to\infty}\left[\sqrt{\pi kb/2}\,\mathrm{e}^{i\pi/4}\,e^{-ikb}\,p_{in}\right]$. It follows that the approximate scattered wave due to an incident plane wave is then $P_{pw} = \lim_{b\to\infty}\left[\sqrt{\pi kb/2}\,\mathrm{e}^{i\pi/4}\,e^{-ikb}P\right]$, where substitution of (3.41) yields

$$P_{pw} = -A_0 H_0^{(1)}(kr) + 2iA_1 H_1^{(1)}(kr)\cos\theta + 2A_2 H_2^{(1)}(kr)\cos 2\theta\,. \qquad (3.45)$$

Equation (3.45) represents an approximate solution and is composed of only the first three terms of an infinite solution. It could have been also obtained from the outer asymptotic solution, Eq. (3.40). For plane wave incidence, the scattered field due to a small cylinder can be represented by only 3 terms and approximates the exact solution to a factor of $1+O\left(k^2a^2\right)$. It is valid over the entire domain, $r \geq a$, including on the surface of the target.

D. NUMERICAL SIMULATIONS

The accuracy of the uniform asymptotic solution (3.41) over representative subsets of the domain, $r, b \geq a$, was numerically evaluated through the use of MATLAB (MathWorks, Natick, MA) by comparing it to the exact solution (3.5) for specific values of the dimensionless parameters *kr*, *kb*, and θ. We used the exact A_n expressions for the B_i coefficients.

Relative error $|1\text{-}P/p_{sc}|$ is presented in Figure 8. The uniform asymptotic solution for fluid and solid are extremely accurate for $ka \ll 1$, as predicted based on their derivation, however, the solution additionally remains relevant for all $ka \leq 1$ for both target types. This was also true for the soft and hard scatterers as shown in [1], and is illustrated in Appendix C. However, there are material specific limitations inherent in the derivation for fluid and solid, i.e., conditions (3.14) and (3.15) should not be violated and $k_2a,\ k_1a,\ ka \leq 1$ due to the small argument approximations made in the derivation.

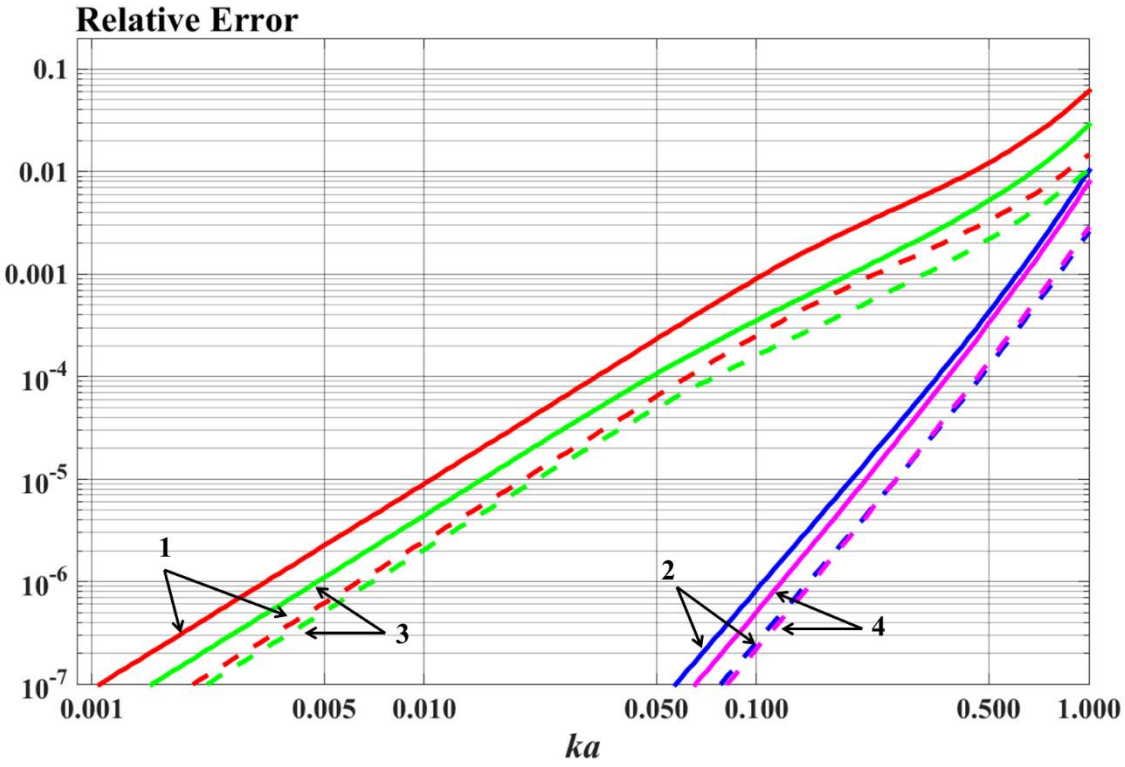

Figure 8. Accuracy of the uniform asymptotic solution for the scattered field due to fluid and solid cylinders. Relative error $|1-P/p_{sc}|$ between the uniform asymptotic solution and the exact field is plotted as a function of ka for exact A_n coefficients for fluid (dashed lines) and for solid (solid lines) cylinders. Material parameters for the fluid are $M_F = 2$, $s = 1.5$ and elastic solid cylinder (aluminum) are $M_{ES} = 2.76$, $s_1 = 4.23$, and $s_2 = 2.03$. The relative error is shown for the angle $\theta = \pi/4$ and the following sets of the other geometric parameters: $b = r = 1.5a$ (1), $b = 1.5a$, $r = 10^3 a$ (2), $b = 10a$, $r = 1.5a$ (3), and $b = 10a$, $r = 10^3 a$ (4).

In reference to Figure 8, and other materials over domains that do not explicitly violate $k_2 a,\ k_1 a,\ ka \le 1$, the uniform asymptotic error, for both fluid and solid cylinders, is proportional to k^2a^2 when $\alpha = O(1)$ and k^4a^4 when $\alpha << 1$, which can be seen by the similarly sloped lines for both limiting domains of interest. Thus, overall second-order accuracy agrees with theoretical estimates, and additional significant gains in accuracy are achieved for the solution when the source or receiver (or both) are located at a distance from the scatterer that is large relative to its radial size, a.

To further analyze and quantify the accuracy of the uniform asymptotic solution, the relative amplitude error ($\delta A/A$) and phase error ($\delta\varphi$) are presented in Figure 9 and Figure 10. The figures further illustrate that the uniform asymptotic solution is an accurate approximation for fluid and solid for all values of $ka \le 1$ for a wide range of θ and α values. Note that neither the relative amplitude error or phase error exceed 0.01 and 0.05 for fluid and solid, respectively, for the entire range of the parameters considered, including *ka* values as large as 1. Figure 9 and Figure 10, additionally, show nonlinear dependence of the represented errors on the parameter *ka*.

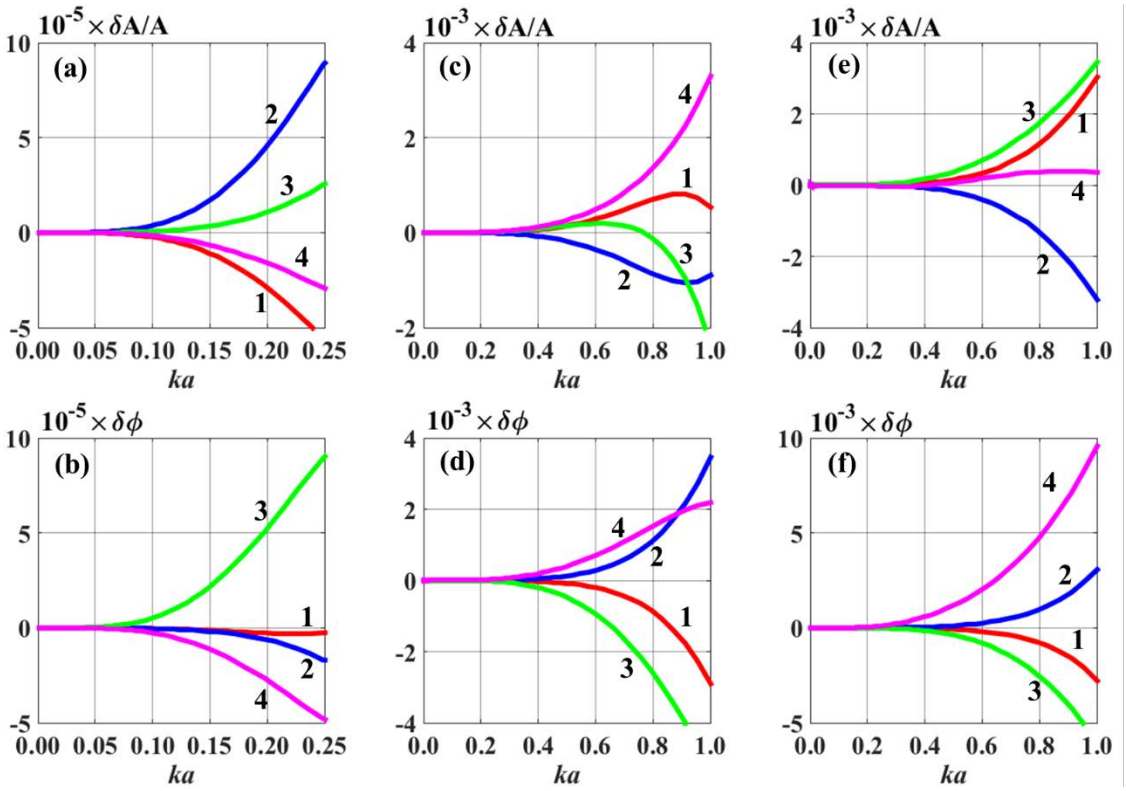

Figure 9. Relative amplitude error ($\delta A/A$) and phase error ($\delta\varphi$) of the uniform asymptotic solutions for the scattered field due to a fluid cylinder. Plots (a), (c), (e) show $\delta A/A$ and plots (b), (d), (f) show $\delta\varphi$, all as a function of the dimensionless radius of the cylinder *ka*. Material parameters of the fluid scatterer are $M_F = 2$, $s = 1.5$. To characterize various source and receiver positions the following dimensionless parameters were used: $kb = 0.25$, $kr = 1$ (a), (b), $kb = 1$, $kr = 20$ (c), (d), $kb = 20$, $kr = 10$ (e), (f) for the following values of the angles $\theta = 0$ (1), $\pi/3$ (2), $2\pi/3$ (3), and π (4).

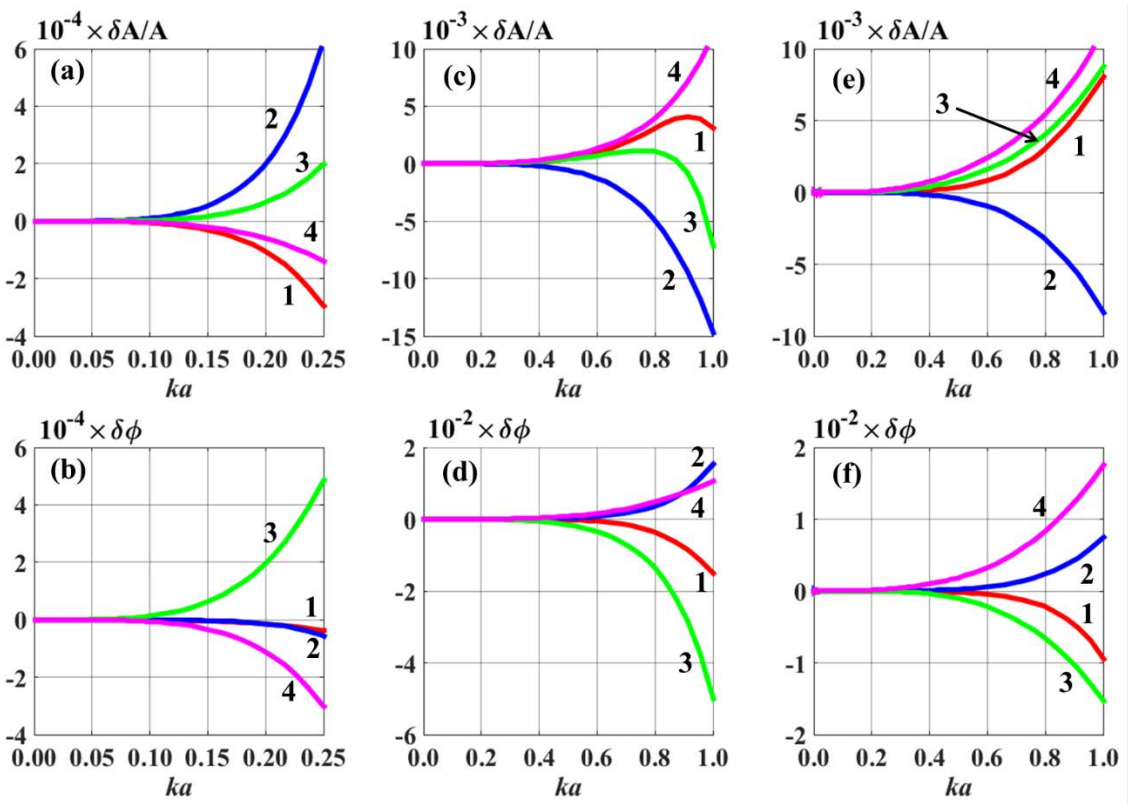

Figure 10. Relative amplitude error ($\delta A/A$) and phase error ($\delta\varphi$) of the uniform asymptotic solutions for the scattered field due to elastic solid cylinder. Plots (a), (c), (e) show $\delta A/A$ and plots (b), (d), (f) show $\delta\varphi$, all as a function of the dimensionless radius of the cylinder ka. Material parameters of the aluminum scatterer are $M_{ES} = 2.76$, $s_1 = 4.23$, $s_2 = 2.03$. To characterize various source and receiver positions the following dimensionless parameters were used: $kb = 0.25$, $kr = 1$ (a), (b), $kb = 1$, $kr = 20$ (c), (d), $kb = 20$, $kr = 10$ (e), (f) for the following values of the angles $\theta = 0$ (1), $\pi/3$ (2), $2\pi/3$ (3), and π (4).

E. RESONANCE SCATTERING OF SOUND BY AN INFINITE CYLINDER

From Section III.C.5, it follows that Rayleigh scattering by an infinite cylinder is controlled by only the first three coefficients: A_0, A_1, and A_2. For the soft and hard cylinder these coefficients depend only on the dimensionless parameter ka [1]. For the fluid and solid cylinder, the coefficients additionally depend on the dimensionless parameters M_F and s, and M_{ES}, s_1, and s_2, respectively. Recall that A_0, $A_1 = O\left(k^2a^2\right)$ and $A_2 = O\left(k^4a^4\right)$ under conditions (3.21) and (3.25) for the fluid and solid targets, respectively. Under these

conditions, the scattering amplitudes of the partial waves are small and steadily decrease with frequency as is the case for the soft and hard targets.

However, in contrast to the soft and hard targets, resonant enhancement of sound scattering from fluid and solid cylinders can occur at certain frequencies within the Rayleigh regime when the inequalities (3.21) and (3.25) do not hold. Here we consider a special case within the Rayleigh regime for fluid and solid cylinders. At resonance, the scattering amplitude A_0 becomes large relative to the other scattering amplitudes, including A_1 and A_2, and the respective partial wave with the A_0 scattering amplitude dominates the total scattered field.

According to Eq. (3.20), the resonance exists for the fluid cylinder when the inequality (3.21) is violated, the quantity $M_F s^2$ is much smaller than unity, and has a certain value of the order $O\left(\kappa^2 (ka)\right)$. These conditions describe a fluid target with a much larger compressibility than that of the surrounding fluid. For instance, this situation can arise for a sufficiently soft fluid target such as an air-filled cylinder in water, where the compressibility is $M_F s^2 \approx O\left(10^{-5}\right) << 1$. Similarly, according to Eq. (3.24), the resonance exists for the solid cylinder when the inequality (3.25) is violated, the quantity $M_{ES}\left(s_1^2 - s_2^2\right)$ is much smaller than unity, and has a certain value of the order $O\left(\kappa^2 (ka)\right)$.

As a function of sound frequency or *ka*, the absolute value of the A_0 scattering amplitude has strong peaks when $k^2 a^2 \left(\ln(ka/2) + \gamma\right) = -2M_F s^2$ and $k^2 a^2 \left(\ln(ka/2) + \gamma\right) = -2M_{ES}\left(s_1^2 - s_2^2\right)$ for the fluid and solid targets, respectively. These equations determine the resonance frequencies for the fluid and solid infinite cylinders. At resonance, the scattering amplitude is $A_0 = 1 + O\left(\kappa^2 (ka)\right)$ and is much larger than $A_1 = O\left(k^2 a^2\right)$ and the values for the respective soft and hard target scattering amplitudes $A_0^{(S)} = O\left(\left|\ln(ka/2)\right|^{-2}\right)$ and $A_0^{(H)}, A_1^{(S)}, A_1^{(H)} = O\left(k^2 a^2\right)$ from [1]. In the vicinity of resonance, the scattered field is dominated by the first term in Eq. (3.41). At resonance, the

total scattered field is then primarily due to a line source located at the origin. Since the scattering amplitudes A_n are independent of the incident wave field, the resonance conditions are, of course, exactly the same as in the case of incident plane waves. For plane incident waves, resonant scattering is dominated by the first term in Eq. (3.45) at the same frequency as for cylindrical incident waves.

In the Rayleigh regime, the resonant scattering is very similar for the fluid and solid targets, and we will focus on the fluid scatterer in the remainder of Section III.E. Dependence of the scattered field amplitude on M and s for a fluid cylindrical scatterer is illustrated in Figure 11 for two regions of interest: $kb, kr = O(ka)$ [Figure 11(a,b)] and $kb >> 1$ [Figure 11(c,d)], where the latter represents the plane wave scattering limit. In all cases, resonant peaks occur when $k^2a^2\left(\ln(ka/2)+\gamma\right) \approx -2M_F s^2$, as predicted from the scattering amplitude $A_0^{(F)}$. When $s = O(1)$, the scattered field due to the fluid cylinder reduces to that due to the soft cylinder when $M_F << -k^2a^2\left(\ln(ka/2)+\gamma\right)/2s^2$, and that due to the hard cylinder when $M_F >> 1$. From [1], since $A_0^{(S)} = O\left(\left|\ln ka/2\right|^{-2}\right)$ and $A_0^{(H)} = O\left(k^2a^2\right)$ the scattered field magnitude is much larger in the soft target limit compared to that of the hard target limit, as seen in Figure 11. Additionally, we see that the scattered field amplitude around resonance is larger than in the soft target limit which was predicted above.

Figure 11(a,b) when the scatterer and receiver are in the near field of the source, exhibit deep minima for all curves when $M_F \approx 1$, as a result of the $\left|A_1^{(F)}\right|$ minimum for that respective value as seen in Eq. (3.23). Figure 11(c,d), when the scatterer and the receiver are in the far field of the source, exhibit *s*- and *θ*-dependent minima ("anti-resonances") which occur when the partial waves with $A_0^{(F)}$ and $A_1^{(F)}$ scattering amplitudes are of similar magnitude, and interfere destructively due to a phase difference of π. Analogous results were seen for the fluid sphere [33].

Resonant scattering in the Rayleigh regime is known to exist for the fluid [33] and solid [63] sphere. The equations that govern the resonant frequencies are $k^2a^2 = 3M_F s^2$ and $k^2a^2 = 3M_{ES}\left(s_1^2 - 4s_2^2/3\right)$ for the fluid and solid spheres, respectively. Hence, a cylinder and a sphere with the same radius resonate at different frequencies. Additionally, the correspondence between the material parameters of fluid and solid scatterers proves to depend on the problem geometry. The correspondences between the fluid and solid parameters are $M_F s^2 \to M_{ES}\left(s_1^2 - s_2^2\right)$ and $M_F s^2 \to M_{ES}\left(s_1^2 - 4s_2^2/3\right)$ for the cylinder and sphere, respectively.

Perhaps the most striking difference between the resonances in the spherical and cylindrical problems is that the frequency dependence of the scattering amplitude by a fluid sphere exhibits a narrower and much higher peak at resonance than for a cylinder of the same radius and material parameters. This can be seen by comparing Figure 11 to that of Figure 6 from [33]. We can explain and quantify this by comparing the ratios of the amplitude of the scattered field at resonance to that in the soft and hard target limits. For the sphere, $\left|A_{0,res}/A_0^{(S)}\right| = O\left((ka)^{-1}\right)$ and $\left|A_{0,res}/A_0^{(H)}\right| = O\left((ka)^{-3}\right)$ [33], and for the cylinder, $\left|A_{0,res}/A_0^{(S)}\right| = O\left(\left|\ln(ka/2)\right|^2\right)$ and $\left|A_{0,res}/A_0^{(H)}\right| = O\left((ka)^{-2}\right)$. Since $ka << 1$ in the Rayleigh regime, the ratios are significantly larger for the sphere than for the cylinder.

Scattering of a cylindrical wave by an infinite cylinder can be viewed as a 2-D model for the scattering of a spherical wave by a sphere. In light of the findings listed above, modeling resonant scattering by 3-D targets using 2-D numerical models will not accurately describe the scattering physics since the resonant scattering properties do not translate correctly.

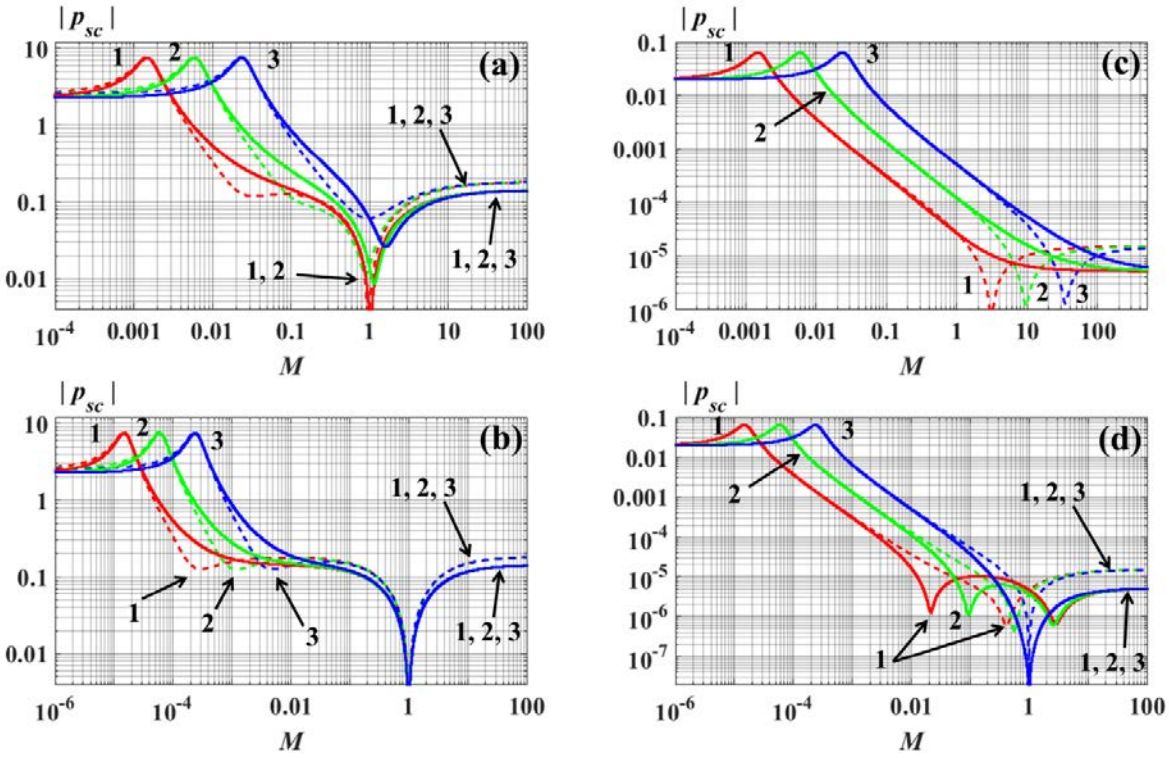

Figure 11. Amplitude dependence of the scattered field on the material parameters of a fluid cylinder. The scattered field amplitude is shown as a function of the density ratio M for various values of the sound speed ratio s, where s = 0.4 (1), 0.2 (2), and 0.1 (3) in (a) and (c); s = 4 (1), 2 (2), and 1 (3) in (b) and (d). In all plots, ka = 0.01; $kb = kr$ = 0.02 in (a) and (b); kb = 20 and kr = 5 in (c) and (d). The angle θ takes the values of 0 (dashed lines) or π (solid lines).

F. ENERGY CHARACTERISTICS OF SCATTERING

In this section, we illustrate the utility of the uniform asymptotic solution and the physical insight into scattering that it provides. Using the uniform asymptotic we compute and present energy quantities for the total acoustic field in proximity of the scatterer where we expect the total field to be greatly distorted. We consider the scattering due to fluid, solid, soft, and hard targets for comparison.

The approximate total field as a result of scattering due to an infinite cylinder is compactly expressed as a simple sum of the fields due to four linear sources (real and image) through the superposition of the exact incident (3.1) and approximate scattered (3.41) fields,

$$p = H_0^{(1)}\left(kR\left(b\right)\right) + B_0 H_0^{(1)}\left(kr\right) + B_1 H_0^{(1)}\left(kR\left(a^2/b\right)\right) + B_2 H_1^{(1)}\left(kr\right)\cos\theta, \quad r \geq a. \tag{3.46}$$

Equation (3.46) for the total field allows convenient analytic development of expressions for the time-averaged energy density (U) [61],

$$U = \frac{pp^*}{4\rho c^2} + \frac{\rho \mathbf{v}\cdot\mathbf{v}^*}{4}, \tag{3.47}$$

and the time-averaged power-flux density (**J**) [61],

$$\mathbf{J} = \frac{1}{2}\mathrm{Re}\left[p^*\mathbf{v}\right], \tag{3.48}$$

valid over the entire domain, $r, b \geq a$. The asterisk represents complex conjugation, and the particle velocity (**v**) can be computed through the use of the linearized Euler equation,

$$\mathbf{v} = \left(-\mathrm{i}/\omega\rho\right)\nabla p. \tag{3.49}$$

Together, U and **J** allow a clear visual realization of the magnitude and direction for the acoustic energy transport from the source to infinity in the presence of various types of scatterers. The direction of energy transport from the source is depicted through the energy streamline. Energy streamlines represent the paths along which cycle-averaged wave energy is transmitted from a source to infinity. In the fluid that surrounds the scatterer, an energy streamline is a line tangent to which at every point is parallel to **J** at that point [64].

The model parameters used will describe Rayleigh scattering by an underwater cylindrical target of radius a = 9.5 cm with axis at $x = y = 0$. The target is submerged in seawater with constant sound speed c = 1500 ms^{-1} and density ρ = 1025 kgm^{-3}. A line source is parallel to the target's axis and emits monochromatic cylindrical waves at frequency f = 250 Hz. The cylindrical wave source is located at $x \equiv b = 10a$, $y = 0$. For these parameters, ka = 0.0995, which is well within the Rayleigh regime (see Figure 8, Figure 9, Figure 10, Figure 26, and Figure 27). Hence, the asymptotic error is small and use of the uniform asymptotic solution leads to a negligible contribution to error when calculating the energy characteristics in Eqs. (3.47) and (3.48). Energy density plots are

normalized using the calculated energy density of the incident wave, p_{in}, at the center of cylinder. Neither U nor **J** are shown within the target.

Figure 12 presents the energy characteristics of scattering due to an aluminum solid cylinder (Figure 12(c,f)) alongside the limiting cases of no target (Figure 12(a,d)) and of the acoustically hard cylinder (Figure 12(b,e)) for comparison. Figure 12(a,d) depicts clearly that for this scattering problem the wave front is a cylinder and not approximately a plane. Thereby, plane-wave approximations would be insufficient. Both the hard and solid targets greatly distort the field in the vicinity of the cylinder. From the energy density plots, both share very similar azimuthal locations for the total acoustic field maxima and minima. The magnitude of the distortion is larger for the hard cylinder compared to that due to the solid one, according to the energy density figures. The power-flux streamlines show that energy is able to propagate through the solid material unlike that for the hard cylinder. As a result, the solid cylinder has a lesser effect on the energy characteristics of the total acoustic field in the vicinity of the cylinder.

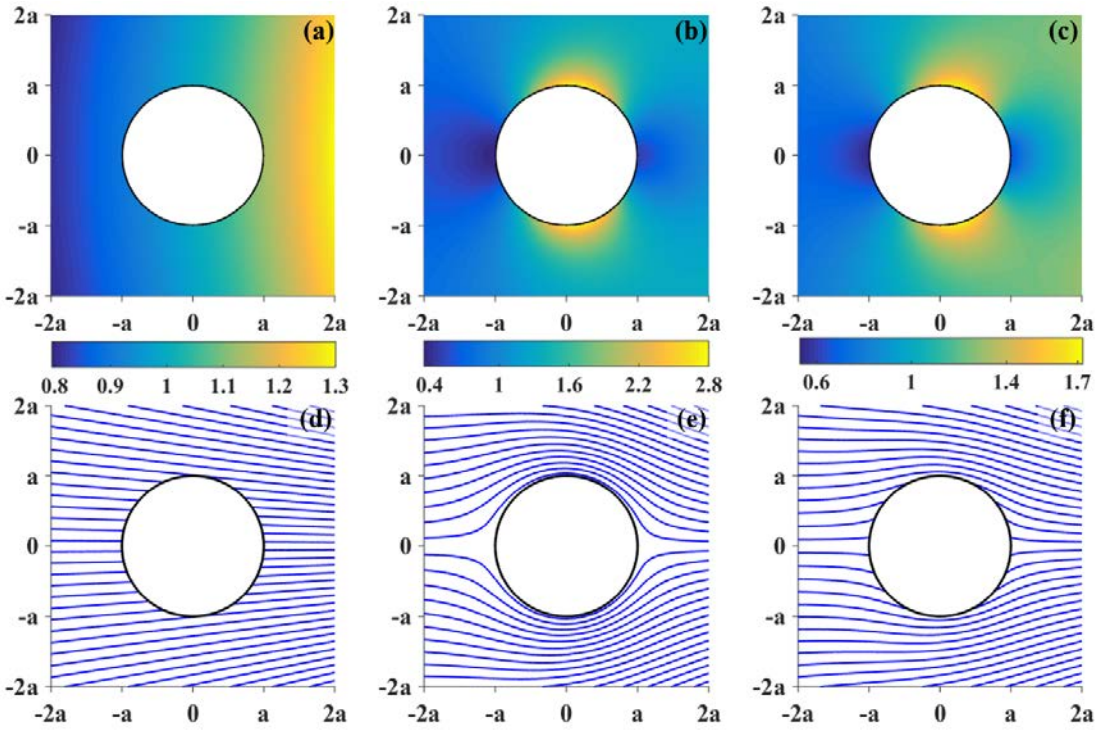

Figure 12. Energy characteristics of the total acoustic field at scattering from a solid cylinder. Energy density (a), (b), (c) and power-flux streamlines (d), (e), (f) are shown for no target (a), (d), hard target (b), (e), and aluminum solid (c), (f). The cylindrical wave source is located at $x = 10a$, $y = 0$.

In proximity of the target, the total acoustic field is significantly distorted due to the scatterer itself. Additionally, from this qualitative analysis for the energy characteristics, knowledge of the target type proves to be equally important in making predictions. For example, acoustic sensors, whether pressure or vector, are typically located in the proximity of a body. Hence, an aluminum solid cylindrical body with mounted sensors would measure distorted field values unless corrected to compensate for the specific body's effect. Bearing determination through the matched field processing technique was previously explored assuming that sensors are mounted on a hard cylinder, and the scattering compensation was found absolutely necessary for the bearing estimation to be achievable at low frequencies [1].

Figure 13 illustrates the energy characteristics of scattering for a fluid cylinder. Fluids with relative compressibilities of either $M_F s^2 = 0.125$ (Figure 13(b,e)) or

$M_F s^2 = 4.5$ (Figure 13(c,f)) are shown in comparison to the limiting case of the acoustically soft cylinder (Figure 13(a,d)). All three types of scatterers shown in the figures greatly distort the field in the vicinity of the cylinder when compared to the limiting case of no target (Figure 12(a,d)). However, in comparison of the plots for *U*, the maxima for the soft target are an order of magnitude larger than for all other targets considered in Figure 12 and Figure 13. This could have been expected given the discussion of the effect on the scattered field magnitude in the soft target limit in Section III.E. The fluid with a relative compressibility of $M_F s^2 = 0.125$ (Figure 13(b,e)) has energy characteristics that are very different from the soft limiting case. However, when the dimensionless parameters take the values of air the plots for the soft case are closely reproduced (not shown).

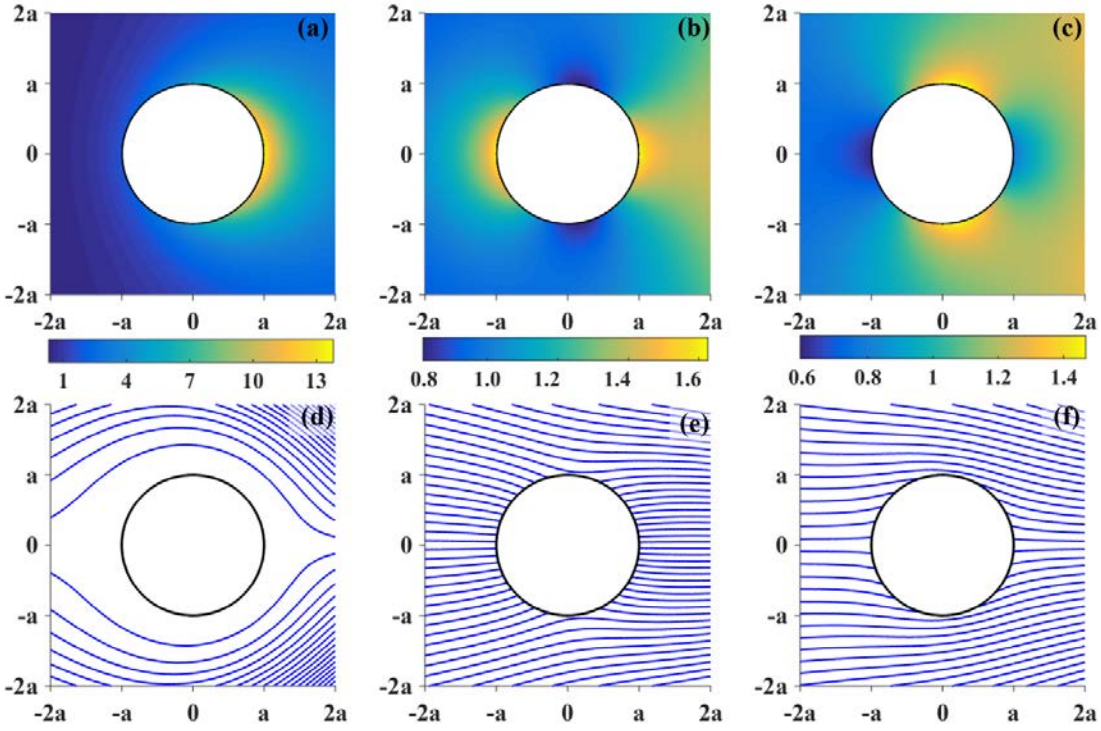

Figure 13. Energy characteristics of the total acoustic field at scattering from a fluid cylinder. Energy density (a), (b), (c) and power-flux streamlines (d), (e), (f) are shown for the soft target (a), (d) and two fluid cylinders: M_F = 0.5, s = 0.5 (b), (e) and M_F = 2, s = 1.5 (c), (f). The cylindrical wave source is located at $x = 10a$, $y = 0$.

Both fluids like the solid allow energy to propagate through the target. This is seen from the energy streamlines not being tangent to the curve defining the surface of the scatterer. The streamlines intersect the surface unlike for the soft and hard targets. Interestingly, the relative compressibility of the fluid has a significant effect on the azimuthal locations of the maximum and minimum in the energy density plots. This relative compressibility azimuthal dependence is not very apparent in the energy streamline plots. The fluid with relative compressibility of $M_F s^2 = 4.5$ has energy characteristic plots that are qualitatively very similar to that of the solid. For the case of similar densities and compressional wave speeds (not shown), the energy characteristics plots for fluid and solid are hardly distinguishable. Also not shown in Figure 12 and Figure 13 is that, although all of the targets significantly distort the total field in vicinity of the scatterer, in the Rayleigh regime only the soft scatterer visibly affects the energy characteristics of the total monochromatic sound field in the far field of the scatterer.

G. CONCLUSION

The classic problem of cylindrical wave scattering by fluid and solid cylinders has well known solutions [28], [29]. The solutions are described in terms of an infinite sum of partial waves. The partial wave scattering amplitudes are determined by the boundary conditions at the surface of the cylinder. The total complex pressure field is represented by the sum of the incident cylindrical wave (3.1) and the scattered (diffracted) wave (3.5).

However, much simpler, closed-form solutions can be obtained in the important special case of Rayleigh scattering where the radius is small compared to the acoustic wavelength. In this chapter, uniform asymptotic solutions (3.41) for the scattered field have been derived through the method of matched asymptotic expansions for fluid and solid cylinders. Additionally, the new asymptotic solutions represent an improvement over recently developed solutions (see Appendix C) for acoustically soft, hard, and impedance cylinders.

The established solutions have second order accuracy or greater with respect to the dimensionless radius of the cylinder, *ka*, and are valid over the entire domain outside the cylinder, $r, b \geq a$. Accuracy of the uniform asymptotic solutions has been confirmed

numerically through comparison with the exact solution. Although the asymptotic solutions were derived assuming $k_2 a, k_1 a, ka << 1$, they have proved to be sufficiently accurate for *ka* values as large as 1, contingent upon that the condition that $k_2 a, k_1 a \leq 1$ is met.

The uniform asymptotic solutions are represented by the sum of acoustic fields due to three image sources located within the cylinder. The asymptotic solution in Eq. (3.41) represents solutions for fluid, solid, soft, hard, and impedance boundary conditions in one compact expression that exactly satisfies the Helmholtz equation. The locations of the sources are the same for all scattering targets and are independent of sound frequency. All target-specific information for the boundaries is solely contained in the complex scattering amplitudes of the three image sources. The uniform asymptotic solution is the field due to three linear sources, a monopole and a dipole source both located at the axis $x = y = 0$ of the cylinder and a monopole source located at $x = a^2/b$, $y = 0$. The locations of the acoustic image sources are the same as in the corresponding electrostatic and magnetostatic problems [36], [58].

For spherical acoustic wave scattering by a small fluid sphere, a similar uniform asymptotic solution was developed in [33]. For the fluid sphere, the asymptotic solution was composed of a monopole source at the center of the sphere $x = y = z = 0$ and dipoles linearly distributed along a line connecting the center of the sphere and the Kelvin inversion point $x = a^2/b$, $y = z = 0$. In comparison to these findings, the image source solution for the case of the fluid cylinder proves to be much simpler than for the fluid sphere. In addition, the error remains small for *ka* as large as 1. This was not the case for the sphere [33].

In the Rayleigh regime, resonance scattering exists for the fluid and solid infinite cylinder as it does for the small sphere [33], [63]. The resonance frequencies at scattering by a cylinder can be estimated accurately through inspection of the A_0 scattering amplitude of the asymptotic solutions. Resonance frequencies were numerically confirmed for various material and geometric parameters. A sphere and cylinder of the same radius and material parameters will resonate at different frequencies and the correspondence between material parameters of the fluid and solid target is similar but not the same in the 2-D and

3-D problems. Modeling spherical resonance scattering using 2-D cylindrical models will lead to inaccurate results. Resonance amplification of scattering is much larger for the sphere than for the cylinder. Away from resonance, in the far field, the scattered field amplitude is stronger for the cylinder than for the sphere. The opposite is true in the near field.

Evaluation of scalar and vector energy characteristics of the total field due to a low-frequency line source in the presence of fluid and solid cylinders was considered as an example of the utility of the uniform asymptotic solutions. Here, the pressure field and related quantities are necessarily calculated at many grid points, so the simple and general form of the uniform asymptotic solution leads to particularly important computational savings. The energy characteristics were evaluated for scattering by fluid and solid targets and compared to the free field as well as soft and hard target cases to provide insights into the total field distortion due to scattering by various objects.

The established uniform asymptotic solution as composed of only a few image sources suggest a mathematically convenient path forward in a number of scattering problems where analytic solutions are not readily available. One problem of particular practical interest is sound scattering by a target located close to the ocean surface or another reflecting boundary. For this type of problem, reflections of the incident and single-scattered waves from the boundary lead to multiple scattering from the target. Further research is required to establish whether a numerically efficient model for problems where multiple scattering by simple shapes is encountered can be obtained in terms of image sources.

IV. PASSIVE, BROADBAND SUPPRESSION OF RADIATION OF LOW-FREQUENCY SOUND

This chapter was previously published as [2]: Oleg A. Godin and Alexander B. Baynes, "Passive, broadband suppression of radiation of low-frequency sound," *The Journal of Acoustical Society of America*, vol. 143, no. 2, pp. EL67-73, 2018.

A. INTRODUCTION

Anthropogenic noise exceeds natural noise levels in several frequency bands important for marine life [65]–[67] and continues to increase with the global economic activity [68]. High levels of low-frequency underwater noise are associated, e.g., with commercial shipping [65], [67], harvesting renewable hydrokinetic energy [69], and off-shore construction activities, including pile driving [65], [70], [71]. Significant noise suppression is achieved by separating sound sources and receivers with air bubble curtains [70], [72] or surrounding the source with an array of encapsulated air bubbles [73], [74]. These approaches to noise abatement are based on resonance absorption of sound by bubbles and, with sufficiently large volume content of air in the bubble curtain, on sound reflection from the curtain due to impedance mismatch with water. Here we explore a complementary approach to underwater noise mitigation, which relies on wave diffraction rather than dissipation or reflection.

When an omnidirectional sound source in liquid approaches a boundary with a gas half-space within a fraction of wavelength, almost all acoustic energy is radiated into the gas, while sound radiation into the far field in the liquid is strongly suppressed [75]–[77]. This chapter investigates the feasibility of achieving a similar effect of radiation suppression by employing a small compliant object instead of the gas half-space. Using results of recent theoretical analyses of acoustic Green's functions in fluids with spherical and cylindrical scatterers [1], [33], we will show that broadband suppression of acoustic radiation can be achieved by placing a spherical or cylindrical object in the near field of the source, and will assess the requirements to material properties of the object. Unlike

absorption- and reflection-based noise suppression, the diffraction mechanism does not require surrounding the source with an acoustic barrier, which is important for potential applications such as abatement of noise due to ship propellers [67] or tidal energy-harvesting turbines [69].

B. POINT SOURCE IN AN UNBOUNDED FLUID

Consider the effect of a spherical obstacle on the acoustic field of a point source. A sphere of radius a is imbedded in a homogeneous fluid with sound speed c and mass density ρ. Introduce a spherical coordinate system with an origin at the center of the sphere. Cartesian coordinates (x, y, z) are related to the spherical coordinates r, θ, φ by $x = r\sin\theta\cos\varphi$, $y = r\sin\theta\sin\varphi$, and $z = r\cos\theta$. A monochromatic point source is located at $\mathbf{r}_0 = (0, 0, b)$; $b > a$ (Figure 14a). It is convenient to represent the acoustic pressure in the spherical wave radiated by the source and in the wave scattered (diffracted) by the sphere in terms of spherical harmonics [14]:

$$p_{in} = D\left|\mathbf{r}-\mathbf{r}_0\right|^{-1}\exp\left(ik\left|\mathbf{r}-\mathbf{r}_0\right|\right) = ikD\sum_{n=0}^{\infty}\varepsilon_n P_n\left(\cos\theta\right)h_n^{(1)}\left(kr_>\right)j_n\left(kr_<\right), \tag{4.1}$$

$$p_{sc} = -ikD\sum_{n=0}^{\infty}\varepsilon_n A_n P_n\left(\cos\theta\right)h_n^{(1)}\left(kb\right)h_n^{(1)}\left(kr\right), \quad r \ge a, \tag{4.2}$$

where $k = \omega/c$ is the acoustic wave number, $r_> = \max\left(r, b\right)$, $r_< = \min\left(r, b\right)$, $\varepsilon_n = 2n + 1$, P_n are Legendre polynomials, j_n are spherical Bessel functions, and $h_n^{(1)}$ are spherical Hankel functions of the first kind [49]. The constant D characterizes the strength of the sound source. Time dependence $\exp\left(-i\omega t\right)$ of the acoustic field is assumed and suppressed. The coefficients A_n in Eq. (4.2) describe amplitudes of spherical harmonics in the scattered wave and depend on the properties of the obstacle. For a "perfectly soft" sphere with pressure release boundary conditions at $r = a$ and a homogeneous fluid sphere, the amplitudes are [14], [33]

$$A_n^{(S)} = j_n\left(ka\right)\Big/h_n^{(1)}\left(ka\right), \tag{4.3}$$

$$A_n^{(F)} = \frac{Msj_n'\left(ka\right)j_n\left(ka/s\right) - j_n\left(ka\right)j_n'\left(ka/s\right)}{Msh_n^{(1)\prime}\left(ka\right)j_n\left(ka/s\right) - h_n^{(1)}\left(ka\right)j_n'\left(ka/s\right)}, \tag{4.4}$$

respectively. For brevity, we will refer to objects with pressure-release boundary as soft. In Eq. (4.4), M and s are the ratios of densities and sound speeds inside and outside the sphere. Here and below we assume that the membrane encapsulating the fluid inside the obstacle is sufficiently thin to have a negligible effect on its oscillations and sound diffraction.

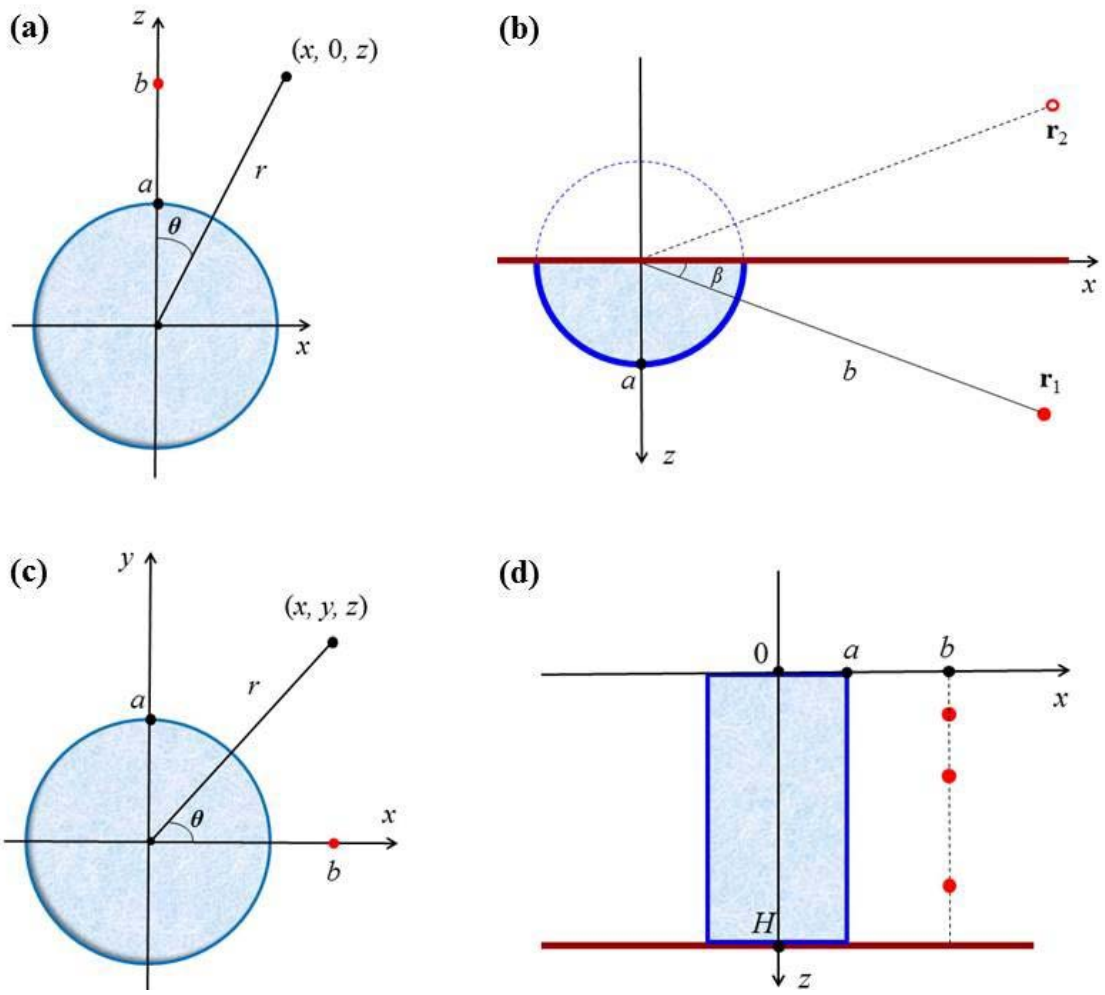

(a) Cross-section through the center of the sphere and sound source is shown in the problem of sound radiation by a point source in the presence of a spherical obstacle in unbounded homogeneous fluid. The origin of Cartesian coordinates (x, y, z) is at the center of the sphere. The sound source is located at the point (0, 0, b) outside the sphere. Radius of the sphere equals a. (b) Cross-section through the center of a hemispheric body and a point source by the plane $y = 0$, which is perpendicular to the rigid boundary $z = 0$, is shown in the problem of suppression of sound radiation by sources near a boundary. The sound source is located at the point $\mathbf{r}_1$. Image source at the point $\mathbf{r}_2$, which is symmetric to $\mathbf{r}_1$ with respect to the rigid boundary, is helpful in reducing the problem to that of sound scattering by a sphere. (c) Cross-section by a plane z = const. is shown in the problem of sound radiation by a linear sound source in the presence of an infinite circular cylinder of radius a. Axis of the cylinder is located at $x = y = 0$ and is parallel to the linear source located at $x = b$, $y = 0$. (d) Cross-section by a vertical plane through the axis of the cylinder and a vertical array of sound sources is shown in the problem of sound radiation suppression in a shallow-water waveguide using a cylindrical obstacle. Sea surface and seafloor are the planes $z = 0$ and $z = H$, respectively. Axis of the cylinder is located at $x = y = 0$, and its radius is a. Horizontal separation between the sound sources and the axis of the cylinder is b.

Figure 14. Geometry of four scenarios of sound radiation suppression by diffraction on a compliant body.

According to Eqs. (4.1) and (4.2), at $r > b$ the full field $p = p_{in} + p_{sc}$ is given by the series in Eq. (4.1) with $j_n(kr_<)$ replaced by

$$B_n = j_n\left(kb\right) - A_n h_n^{(1)}\left(kb\right). \tag{4.5}$$

With amplitudes of the spherical harmonics known, the acoustic power I radiated by the source can be calculated by integrating the radial component $\mathrm{Im}\left(p^* \partial p/\partial r\right)\big/2\omega\rho$ of the power flux density vector over a sphere $r = \text{const} > b$, which gives

$$I = \frac{2\pi}{\rho c}\left|D^2\right|\sum_{n=0}^{\infty}\varepsilon_n\left|B_n\right|^2. \tag{4.6}$$

Contributions to the power flux of the spherical harmonics of different orders n are additive, which reflects their orthogonality. Note that the ratio I/I_0, where I_0 is the radiated power in the absence of the obstacle, i.e., at $a = 0$, remains the same when any number of coherent or incoherent point sources are located at the same distance from the sphere.

The goal of noise mitigation is to minimize I. Diffraction on an obstacle suppresses sound radiation when the diffracted wave p_{sc} interferes destructively with the incident wave p_{in}. For the destructive interference to occur everywhere, the effective sources of the diffracted wave [33], which are located within the obstacle, need to be in the near field of the sound source. When $ka \le kb \ll 1$, Eqs. (4.3)–(4.5) can be simplified using small-argument expansions of the spherical Bessel functions [33]. For the soft sphere, we find $B_0 = \left(1 - a/b\right)e^{-ika}\left[1 + O\left(k^2b^2\right)\right]$, $B_n = B_0 O\left(k^n b^n\right)$, $n = 1, 2, \ldots,$ and $I/I_0 = \left(1 - a/b\right)^2\left[1 + O\left(k^2b^2\right)\right]$. When a/b is close to 1, strong suppression of sound radiation is predicted in a wide frequency band, where kb is small. This is expected since p is known to vanish everywhere, i.e., full cancellation of p_{in} is achieved [33] in the limit $b \to a > 0$ in the case of a soft obstacle. Predictions of the asymptotic theory are confirmed by calculations based on exact Eqs.(4.1)–(4.3), (4.5), and (4.6) (Figure 15a). The solution scales with sound frequency. Dependence on the frequency, radius of the sphere, and distance to the source is shown in Figure 15a in terms of dimensionless parameters ka and b/a. As b/a increases from its minimal value of 1, the radiated power increases and exceeds

I_0, when $kb \sim \pi$, due to constructive interference of p_{sc} and p_{in}. At large kb and $b/a > 1$, diffraction has little effect on the radiated power.

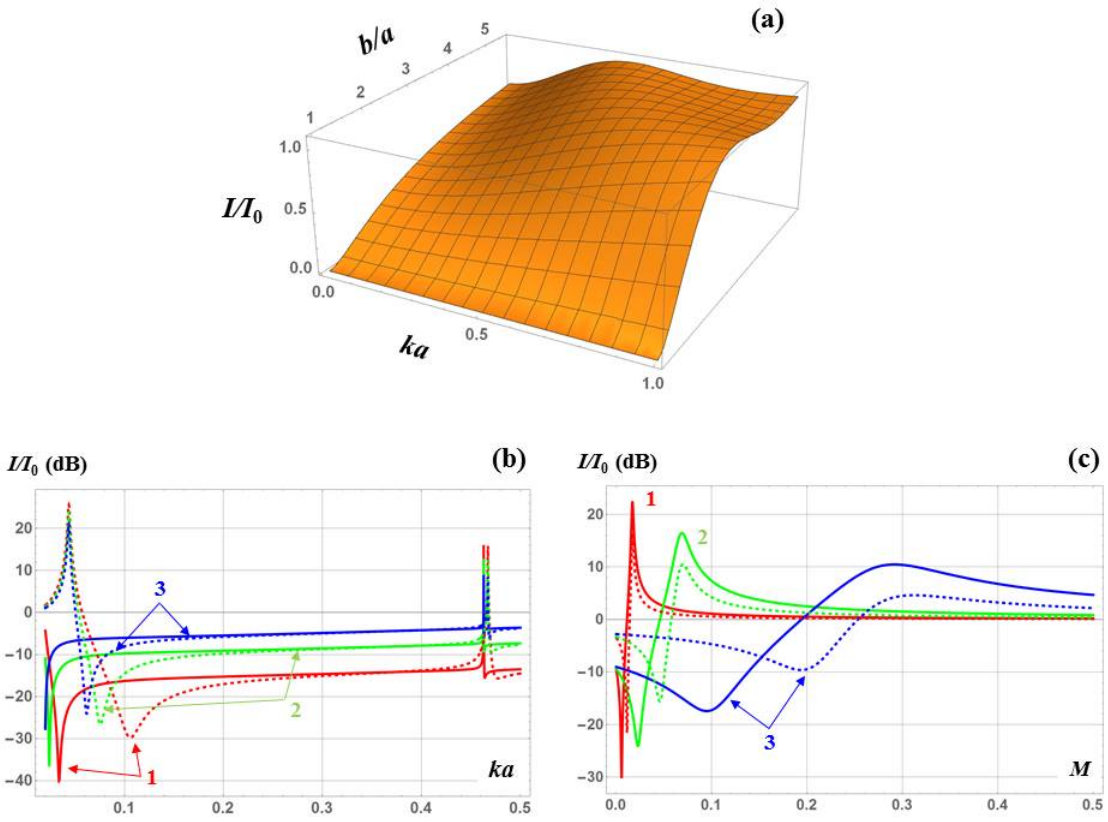

Figure 15. Noise mitigation by placing a small compliant sphere in the near field of a compact sound source. (a) Ratio I/I_0 of the acoustic power radiated by a point source with and without a perfectly soft sphere is shown as a function of the sphere radius a and the distance b from the source to the center of the sphere; k is acoustic wavenumber. (b) Ratio I/I_0 of the acoustic power radiated with and without a fluid sphere is shown as a function of dimensionless radius, ka, of the sphere for three distances b from the source to the center of the sphere: b/a = 1.2 (line 1), 1.5 (2), and 2.0 (3). The ratio M of fluid densities inside and outside the sphere is either 0.0013 (solid lines) or 0.013 (dashed lines). (c) Dependence of the radiated power on density of the fluid sphere is shown for two positions of the sphere: b/a = 1.5 (solid lines) or 3.0 (dashed lines) and three values of the dimensionless radius: ka = 0.05 (line 1), 0.1 (2), and 0.2 (3). The ratio of sound speeds inside and outside the fluid sphere s = 2/9 in all cases.

A soft obstacle is an idealization. For a fluid sphere, from Eqs. (4.4) and (4.5) we find that $B_n = O\left(k^n b^n\right),\ n = 1, 2, \ldots$ and

$$B_0 \approx 1 - \frac{\left(1 - Ms^2\right) k^2 a^3 / b}{k^2 a^2 \left(1 + ika\right) - 3Ms^2}, \tag{4.7}$$

when $kb \ll 1$ and $ka/s \ll 1$. These conditions ensure that the radius of the sphere is small compared to the acoustic wavelength in fluids inside and outside the sphere. As in the soft obstacle case, spherical harmonics with $n \geq 1$ give a small contribution of $O(k^2b^2)$ to the radiated power in Eq. (4.6). It follows from Eq. (4.7) that B_0 is close to unity and there is no radiation suppression unless $Ms^2 \ll 1$. The quantity Ms^2 has a meaning of the ratio of compressibilities of fluids outside and inside the sphere, and is small, e.g., for gas inclusions in a liquid. When $3Ms^2 \ll k^2a^2 \ll 1$, B_0 in Eq. (4.7) reduces to the previous result for a soft sphere. Wide-band noise suppression occurs in this regime as long as b/a is close to 1 (Figure 15b).

Beyond this frequency interval, frequency dependence of sound radiation in the presence of a fluid sphere is more complicated than for a soft one. A strong enhancement of radiation occurs at the resonant frequency of sound scattering by the sphere [14], [33] where $3Ms^2 = k^2a^2 \ll 1$ and $|B_0| \approx [1 + (kb)^{-2}]^{1/2}$. By minimizing $|B_0|$ with respect to Ms^2, from Eq. (4.7) we find that an 'anti-resonance" (a sharp drop in sound radiation) occurs at such frequency that

$$3Ms^2 = \left(1 - a/b\right) k^2 a^2. \tag{4.8}$$

This effect can be utilized when suppression of noise around a particular frequency, e. g., the blade passing frequency of a ship's propeller, is desired. The "anti-resonance" frequency is of the order of, but higher than, the resonance frequency. These findings are consistent with the back-of-the-envelope calculations and experimental results of Lee et al. [78], who studied a related problem of suppression of a ship's hull vibrations induced by propeller cavitation.

Figure 15, which presents calculations based on exact Eqs. (4.1)–(4.6), supports the above predictions of the asymptotic theory and illustrates sensitivity of the results to material parameters of the sphere. Position of the sphere relative to the source affects the

"anti-resonance" frequency and efficiency as well as radiation enhancement at resonance (Figure 15b). When $3Ms^2 \ll k^2a^2 \ll 1$ and $ka/s \ll 1$, efficiency of radiation suppression is a function of b/a and is insensitive to sound frequency and the small ratio of the compressibilities, Ms^2. Additional narrow peaks in Figure 15b occur around $ka = 0.46$, where the condition $ka/s \ll 1$ is violated and $j_1'(ka/s) = 0$ in Eq. (4.4). These peaks correspond to a resonance of non-spherically symmetric oscillations of the sphere. The width of the peak is proportional to M, and the peak, although undesirable, will have an insignificant effect on suppression of broadband noise if M is sufficiently small. When the "anti-resonance" is employed to suppress a given frequency, compressibility of the sphere can be chosen to optimize the noise mitigation (Figure 15c). As predicted by Eq. (4.8), the required compressibility depends on the radius of the sphere and the distance to the source. As much as 40 dB noise suppression, albeit in a narrow frequency band, can be achieved that way at low frequencies, where $ka \ll 1$ (Figure 15c). The numerical values $M = 0.0013$ and $s = 2/9$ of the density and sound speed ratios that are used in Figure 15b and Figure 15c correspond to an air bubble in water at normal conditions.

Efficient noise suppression requires that the quantity $1 - a/b$ is small. For a distributed noise source within a sphere of radius R, this requires $b - a \geq R$ and $1 - a/b \geq R/(a + R)$. Larger values of a broaden the frequency band of noise suppression and simultaneously improve performance in the case of finite sources. Figure 15b suggests using air-filled spheres with a radius as large as 0.075 of the acoustic wavelength in water.

C. POINT SOURCE NEAR A BOUNDARY

Noise sources are often located in the vicinity of boundaries, e.g., the ship's hull surface in the case of propeller noise. Use of diffraction for radiation suppression can be extended to such geometries. As a simple example, consider an omnidirectional source at point $\mathbf{r}_1 = b(\sin\beta, 0, \cos\beta)$, $0 \leq \beta \leq \pi/2$ in a fluid half-space $z > 0$ with a rigid boundary $z = 0$ (Figure 14b). Let a hemispherical obstacle $0 \leq r \leq a$, $z > 0$ be used for radiation suppression; $a \leq b$. Then the acoustic field at $z \geq 0$ will be the same as due to two identical point sources at $\mathbf{r}_1$ and $\mathbf{r}_2 = b(\sin\beta, 0, -\cos\beta)$ in an unbounded fluid with a spherical obstacle. For a small sphere ($ka \ll 1$), the terms with $n = 0$ and 1 are known to be dominant

in the series (4.2) in the far field [14], [33]. Using Eq. (45) in [33] for the field scattered by a sphere, for the far field in the problem with a hemisphere on a rigid plane we find

$$p = 2D\frac{e^{ik(r+b)}}{r}\Big[\cos\left(kb\cos\beta\cos\theta\right)e^{-ikb\left(1+\sin\beta\sin\theta\cos\varphi\right)} + \frac{iA_0}{kb} - \frac{3iA_1\left(1-ikb\right)}{k^2b^2}\sin\beta\sin\theta\cos\varphi\Big]. \tag{4.9}$$

Integration of the far-field power flux density $|p|^2/2\rho c$ over the hemisphere r = const, $0 \le \theta \le \pi/2$, $0 \le \varphi \le 2\pi$ and taking into account that $kb \ll 1$, gives

$$\frac{I}{I_0} = \left|1+\frac{iA_0}{kb}\right|^2 + 3\frac{\left|A_1^2\right|\sin^2\beta}{k^4b^4}. \tag{4.10}$$

A similar but simpler analysis in the case of a spherical obstacle in unbounded fluid gives the result that differs from Eq. (4.10) only by replacing $\sin\beta$ with 1. Thus, a hemispheric obstacle on a rigid surface provides at least as much radiation suppression as a sphere of the same material in unbounded fluid. For soft and, as long as $ka/s \ll 1$, fluid obstacles, the term with A_1 is a small correction to the first term in the right-hand side of Eq. (4.10). Then, all our findings regarding radiation suppression by a sphere in homogeneous fluid, including Eqs. (4.7) and (4.8), apply to the case of a hemisphere on a rigid plane.

D. SOUND SOURCES IN A WAVEGUIDE

Another problem, which admits a simple analysis, is sound radiation by a linear source in the presence of a circular cylinder with its axis parallel to the source. Let the source be located at $x = b$, $y = 0$, $-\infty < z < \infty$. Introduce cylindrical coordinates r, θ, z such that $x = r\cos\theta$ and $y = r\sin\theta$. The source radiates a cylindrical wave with acoustic pressure $p_{in} = H_0^{(1)}\left(kr\right)$, which is scattered (diffracted) by a homogeneous cylinder at $0 \le r \le a$, $-\infty < z < \infty$ (Figure 14c). Mathematically, this is a 2-D counterpart of the problem of a spherical wave diffraction on a sphere. In cylindrical coordinates, solution of the 2-D problem [1] will be given by the same Eqs. (4.1)–(4.6) as in the 3-D case, if spherical Bessel functions j_n and $h_n^{(1)}$ are replaced with Bessel functions J_n and $H_n^{(1)}$, $P_n(\cos\theta)$ is replaced with $-ik^{-1}\cos n\theta$, and $\varepsilon_n = 1$, when $n = 0$, and $\varepsilon_n = 2$, when $n = 1, 2, \ldots$. Then I in Eq. (4.6) has the meaning of radiated power per length $1/\pi k$ of the linear source. Asymptotic

analysis of the effect of a soft or fluid cylinder on low-frequency sound radiation by a linear source is similar to the analysis we outlined in the 3-D case and will not be reproduced here. Figure 3a shows the ratio of the power radiated by the linear source with and without a soft cylinder present. The calculations are based on the exact Eqs. (4.1)–(4.6). As in the 3-D case (Figure 15a), strong suppression of sound radiation is predicted in a wide frequency band when radius a of the cylinder is close to b. This is due to destructive interference of the incident and diffracted waves. Full cancellation occurs in the limit $b \to a > 0$. As kb increases and reaches values of about π, destructive interference gradually transforms into constructive, leading to enhancement of sound radiation. The enhancement and subsequent oscillations of I/I_0 with increasing kb are more pronounced for the cylinder than for the sphere. On the other hand, the cylinder gives stronger suppression of radiation at $ka \ll 1$ (cf. Figure 15a and Figure 16a).

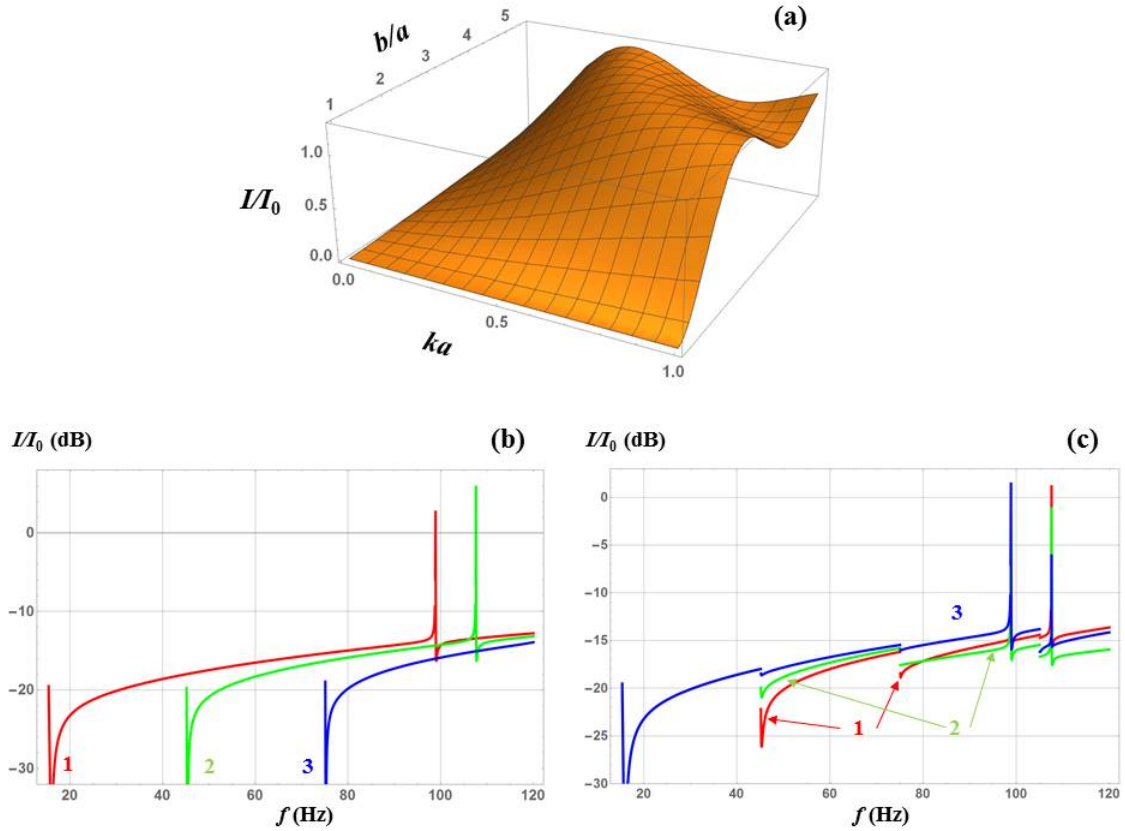

Figure 16. Noise mitigation using a compliant cylindrical object of small radius. (a) Ratio I/I_0 of the acoustic power radiated by a linear sound source with and without an infinite, perfectly soft circular cylinder of radius a in the near field. Axis of the cylinder is parallel to the linear source; b is the distance from the source to the axis of the cylinder; k is acoustic wavenumber. (b) The ratio I/I_0 of the acoustic power radiated with and without a fluid cylinder with a vertical axis in a shallow-water waveguide is shown as a function of sound frequency for the first three normal modes. Mode orders are indicated in the plot. (c) The ratio I/I_0 of the acoustic power radiated by a point source in the shallow-water waveguide with and without the fluid cylinder is shown as a function of sound frequency. The source depth is 0.25 (1), 0.5 (2), or 0.75 (3) of the water depth. The three curves differ only at frequencies above the cutoff frequency of the second mode. Water depth H = 25 m in the waveguide, the ratios of density and sound speed in the fluid cylinder to those in water are M = 0.0013 and s = 2/9, cylinder radius a = 1 m, horizontal separation of the cylinder axis from the source b = 1.3a; cutoff frequencies of the first four normal modes are 15, 45, 75 Hz, and 105 Hz, respectively.

Consider now sound radiation suppression in a waveguide. We model a shallow-water waveguide as a homogeneous fluid layer $0 < z < H$ between a pressure-release surface at $z = 0$ and rigid bottom at $z = H$. A homogeneous fluid cylinder occupies the entire vertical extent of the waveguide at $0 \le r \le a$. A sound source is located at distance b from the cylinder axis (Figure 14d). The source has negligible radial dimensions and an arbitrary vertical structure. For example, sound may be radiated by a vertical array of point sources or vibrations of a driven pile [70], [71].

It is convenient to represent acoustic pressure in the waveguide as a superposition of local normal modes [48]:

$$p = \sum_{m=1}^{\infty} \psi_m(r,\theta) P_m(z), \quad P_m = \left(\frac{2\rho}{H}\right)^{1/2} \sin\left(\frac{\pi z}{H}\left(m - \frac{1}{2}\right)\right). \tag{4.11}$$

Since shape functions $P_m(z)$ of the modes are the same inside and outside the cylinder, there is no coupling between modes of different orders m in our horizontally inhomogeneous waveguide [48], and the 2-D wave equations and boundary conditions for the complex amplitudes $\psi_m(r, \theta)$ of the modes are the same as in the previously considered problem of cylindrical wave diffraction on a cylinder. In the boundary value problem for ψ_m, the densities of fluid outside and inside the cylinder are the actual densities ρ and $M\rho$, while the sound speeds are the phase speeds $c\left(1 - f_m^2 / f^2\right)^{-1/2}$ and $c\left(s^{-2} - f_m^2 / f^2\right)^{-1/2}$ of the m-th mode [48]. Here f and $f_m = (2m-1)/4H$ are sound frequency and cutoff frequency of the mode outside the cylinder. An acoustic normal mode is evanescent and does not carry energy to the far field at frequencies below its cutoff.

Because of mode orthogonality, the power radiated by the source is the sum of power fluxes carried by individual normal modes. Above the cutoff, the effect of the cylinder on acoustic power flux in an individual normal mode is given by equations derived for the infinite cylinder. Figure 16b illustrates radiation suppression of modal power fluxes at low frequencies. (Details of the frequency dependence of I/I_0 at $f \to f_m$ are not shown in the figure because the limiting behavior of the phase speed, $c_m \to \infty$, in the waveguide with a rigid bottom is not representative of waveguides with a fluid or solid bottom.) The results for radiation suppression by a cylinder in the waveguide are qualitatively similar to

radiation suppression by a sphere in an unbounded fluid (Figure 15b), including "anti-resonance" and broadband suppression. However, stronger frequency dependence is encountered in the waveguide due to modal dispersion. At a given frequency, broadband radiation suppression is better for higher-order modes. Narrow resonance peaks of frequency dependence of the radiated power, which are seen in Figure 16b around 100 Hz for mode 1 and 110 Hz for mode 2, have exactly the same origin but are not as strong as previously discussed peaks in the case of a sphere (Figure 15b). With their width being a fraction of Hertz, the peaks have a negligible effect on suppression of broadband noise.

To calculate the power radiated by a given source, one needs to know excitation coefficients of all propagating normal modes. For a point source at depth z_0, mode amplitudes ψ_m in Eq. (4.11) are proportional to $P_m(z_0)$. The frequency-dependent ratio I/I_0 of the power radiated by the source with and without the cylinder present becomes a function of the source depth at frequencies $f > f_2$, when there are at least two propagating normal modes in the waveguide. Depending on sound frequency, radiation suppression may increase or decrease with source depth (Figure 16c), but remains bounded at each frequency by the minimum and maximum modal values of I/I_0 for the excited modes. Figure 16c indicates that, in the example considered, passive suppression of low-frequency noise by at least 12 dB is achieved in a 3 octave-wide frequency band by using a simple fluid obstacle with realistic parameters. The suppression takes advantage of sound diffraction rather than dissipation.

E. DISCUSSION

We have studied four basic sound propagation scenarios to illustrate and quantify the possibility of using diffraction (scattering) to passively suppress unwanted sound radiation. Broadband noise suppression in free space is achieved by placing a highly compliant object in the near field of a compact sound source provided that the size of the object is comparable to its distance from the source and small compared to the acoustic wavelength. Multiple nearby sources can be suppressed simultaneously by the same object. It has been shown that the proposed approach allows strong suppression of acoustic radiation by compact sources near boundaries and in waveguides. The approach is most

efficient at low frequencies where alternative, absorption- and reflection-based mechanisms of noise mitigation become impractical. Diffractive suppression of sound radiation requires materials with high dynamic compliance. The ratio of compliances of the object and surrounding fluid controls the width of the frequency band, within which the radiation suppression takes place. To avoid resonance scattering, it is preferable to achieve high compliance by having small density of the object rather than small sound speed. In shallow water, encapsulated gas bubbles offer suitable physical properties. Deep-water applications would benefit from acoustic metamaterials with high dynamic compliance, such as metal foams [79].

Acoustic energy radiated by a transient source can be calculated as an integral over frequency of the power radiated by monochromatic components of the signal. Therefore, transient noise sources will be suppressed by diffraction on compliant objects, as discussed above for monochromatic sources, as long as the source spectrum is within the frequency range of the broadband noise suppression.

This chapter considered radiation suppression only by obstacles of a few of the simplest shapes. Apparently, superior results can be achieved by optimizing the shape. Shape optimization may in fact be necessary when dealing with real-world noise sources rather than omnidirectional point sources. Other important issues to be addressed in future research include the effects of encapsulating membranes or shells on noise suppression by diffraction on gas-filled objects and the role of multiple scattering when dealing with finite-size noise sources.

V. AN ANALYTIC AND NUMERICALLY EFFICIENT MODEL FOR LOW-FREQUENCY SOUND SCATTERING BY AN INFINITE CYLINDER NEAR AN INTERFACE

This chapter is in preparation to be submitted as: Alexander B. Baynes and Oleg A. Godin, "An analytic and numerically efficient model for low-frequency sound scattering by an infinite cylinder," *Journal of Theoretical and Computational Acoustics*.

A. INTRODUCTION

Rayleigh scattering of sound by a target can be described as a wave radiated by virtual point sources inside the target [1], [3], [32], [33]. When a target is located close to the ocean surface or another reflecting boundary, reflections of the incident and single-scattered waves from the boundary lead to multiple scattering from the target, with the target being insonified by nearby virtual sources. At low frequencies and for shallow targets, the distance from a virtual source to the target is not necessarily large compared to the acoustic wavelength or the target's dimensions. Solutions to this problem are generally solved using numerical methods [19], [22], [37]. This chapter takes advantage of the virtual source concept and recently derived explicit analytic representations of 2-D acoustic Green's functions in unbounded fluids with inclusions of a circular cross-section [1], [3] to develop a simple and numerically efficient model of multiple scattering. Scattering from soft, hard, and fluid objects is considered. The model is used to study the acoustic field in the vicinity of targets near a pressure release surface or a hard bottom, examine conditions of applicability of the single-scattering approximation, and take advantage of the analytic form of the approximate solution to investigate relevant acoustic quantities.

This chapter is organized as follows. In Section V.B, a background on cylindrical wave scattering by an infinite cylinder in free space and in the presence of a boundary is discussed. We establish, specific to the Rayleigh scattering regime, a semi-analytic method to approach the latter problem in Section V.C. In Section V.D, the geometry of multiple

scattering of infinite cylinders near interfaces is investigated. Accuracy of the developed solution is numerically compared to the single scattering approximation and a near-exact least square solution in Section V.E. In Section V.F, the analytic approximate solution is employed to explore important scalar and vector scattering characteristics for the acoustic field in the vicinity of a target near a boundary. Lastly, Section V.G provides a summary of our conclusions.

B. THEORETICAL BACKGROUND

Here, we review the necessary theoretical building blocks to form an approach to solving the problem of cylindrical wave diffraction by an infinite cylinder in a homogenous medium in the presence of an interface. Our approach is based on the solution to the problem of scattering by a cylinder in free space. We first discuss the exact solution to this problem and then the recently derived approximate solutions that are valid specifically in the Rayleigh scattering regime [1], [3]. Lastly, we discuss the complexities that arise with introduction of the interface due to the physical process of multiple scattering.

1. Scattering by a Cylinder in Free Space

a. Exact Solution

In this scattering problem and throughout, we consider monochromatic incident cylindrical waves of frequency ω originating from an infinite line source. The cylindrical waves are incident upon and diffracted by an infinite circular cylinder. The cylinder has constant radius *a*, and its axis runs parallel to the linear source. Wave scattering by acoustically soft, hard, and fluid targets is considered. The cylinder and source are embedded in a homogenous fluid with sound speed *c*, acoustic wave number $k = \omega/c$, and density ρ.

For the problem described, the acoustic pressure field is independent of the *z*-coordinate along the axis of the cylinder. As a result, we can reduce the complexity of this problem by equivalently representing it as a two-dimensional problem. For simplicity, the polar coordinate system consisting of the coordinates (r,θ) will be used. Cartesian

coordinates are defined by the relationships $x = r\cos\theta$ and $y = r\sin\theta$. The origin of the coordinate system is located at the center of the cylindrical body.

The complex acoustic pressure field due to an incident cylindrical wave can be expressed as [14]

$$p_{in} = H_0^{(1)}\left(kR\left(x_0, y_0\right)\right),\ R\left(x_0, y_0\right) = \sqrt{\left(x - x_0\right)^2 + \left(y - y_0\right)^2},\ b = \sqrt{x_0^2 + y_0^2}\,. \qquad (5.1)$$

Here, and throughout, $\exp\left(-\mathrm{i}\omega t\right)$ time dependence is assumed and suppressed. The sum of the incident $\left(p_{in}\right)$ and resultant scattered $\left(p_{sc}\right)$ pressure fields form the total acoustic $\left(p\right)$ pressure field. The geometry of the problem is shown in Figure 17, where the source is located at the coordinates $\left(x_0, y_0\right)$ a distance $b > a$ from the center of the cylinder, and $R\left(x_0, y_0\right)$ is the distance from the source to any point $\left(x, y\right)$. Additionally, $H_0^{(1)}\left(q\right)$ is the Hankel function of the first kind of 0^{th} order, that are expressed for any order n as $H_n^{(1)}\left(q\right) = J_n\left(q\right) + \mathrm{i}Y_n\left(q\right)$. $J_n\left(q\right)$ is the Bessel function and $Y_n\left(q\right)$ is the Neumann function [49].

In the surrounding fluid, outside of the cylinder, the scattered acoustic pressure $\left(p_{sc}\right)$ satisfies the 2-D Helmholtz equation,

$$\nabla^2 p_{sc} + k^2 p_{sc} = 0,\ \ r > a\,. \qquad (5.2)$$

The incident and scattered acoustic pressure fields can be expressed as an infinite series of cylindrical functions as [14]

$$p_{in} = \sum_{n=0}^{\infty} \varepsilon_n H_n^{(1)}\left(kr_>\right) J_n\left(kr_<\right)\cos n\left(\theta - \theta_b\right),\ \ r_> = \max\left(r, b\right),\ \ r_< = \min\left(r, b\right) \qquad (5.3)$$

$$p_{sc} = -\sum_{n=0}^{\infty} \varepsilon_n A_n H_n^{(1)}\left(kb\right) H_n^{(1)}\left(kr\right)\cos n\left(\theta - \theta_b\right),\ \ r \ge a \qquad (5.4)$$

where ε_n is the Neumann symbol ($\varepsilon_0 = 1;\ \varepsilon_n = 2$ for $n \ge 1$), r is distance from origin to observation field point (x, y), and the angles θ and θ_b are depicted in Figure 17. The A_n coefficients are currently undetermined. The coefficients represent the scattering amplitudes for individual partial waves. They are determined by the boundary conditions at the surface of the cylinder, where $r = a$.

For the fluid scatterer, let p_F be the total pressure within the cylinder $r < a$. The scatterer is composed of a homogenous inviscid fluid with mass density $\rho_F = M_F \rho$, sound speed $c_1 = sc$, and acoustic wave number $k_1 = \omega / c_1$. The acoustic (compressional) wave within the scatterer satisfies the 2-D homogeneous Helmholtz equation,

$$\nabla^2 p_F + k_1^{\,2} p_F = 0, \quad r < a \ . \tag{5.5}$$

The acoustic pressure field within the scatterer can be expressed as an infinite series of cylindrical functions as [14],

$$p_F = \sum_{n=0}^{\infty} \varepsilon_n D_n^{(F)} H_n^{(1)}(kb) J_n(k_1 r) \cos n(\theta - \theta_b), \quad r \le a \,, \tag{5.6}$$

where the $D_n^{(F)}$ coefficients represent undetermined complex amplitudes of partial waves.

The acoustic boundary conditions for acoustically soft (*S*), hard (*H*), and fluid (*F*) cylinders, respectively, are [61]

$$p_{in} + p_{sc}^{(S)} = 0, \quad r = a \,, \tag{5.7}$$

$$\frac{\partial p_{in}}{\partial r} + \frac{\partial p_{sc}^{(H)}}{\partial r} = 0, \quad r = a \,, \tag{5.8}$$

$$p_F = p_{in} + p_{sc}^{(F)}, \quad \frac{\partial p_F}{\partial r} = M_F \left(\frac{\partial p_{in}}{\partial r} + \frac{\partial p_{sc}^{(F)}}{\partial r} \right), \quad r = a \,. \tag{5.9}$$

The individual scattering amplitudes are easily solved through direct substitution of the exact expressions for the fields in Eqs. (5.3), (5.4), and (5.6) and their respective radial derivatives into the boundary conditions in Eqs. (5.7)-(5.9). The individual partial wave scattering amplitudes due to soft (*S*), hard (*H*), and fluid (*F*) cylinders are

$$A_n^{(S)} = J_n(ka) \big/ H_n^{(1)}(ka) \,, \tag{5.10}$$

$$A_n^{(H)} = J_n'(ka) \big/ H_n^{(1)\prime}(ka) \,, \tag{5.11}$$

$$A_n^{(F)} = \frac{M_F s J_n'(ka) J_n(k_1 a) - J_n(ka) J_n'(k_1 a)}{M_F s H_n^{(1)\prime}(ka) J_n(k_1 a) - H_n^{(1)}(ka) J_n'(k_1 a)} \,, \tag{5.12}$$

$$D_n^{(F)} = \frac{2\mathrm{i} M_F s / (\pi ka)}{M_F s H_n^{(1)\prime}(ka) J_n(k_1 a) - H_n^{(1)}(ka) J_n'(k_1 a)} \,. \tag{5.13}$$

Substitution of Eqs. (5.10)–(5.12) into Eq. (5.4) yields the exact solution to the free-space problem of cylindrical wave diffraction by an infinite cylinder. Substitution of Eq. (5.13) into Eq. (5.6) yields the exact solution for the acoustic field within the fluid cylinder.

b. Low-Frequency Uniform Asymptotic Solution

We limit this chapter only to a scattering problem where the wavelength is large compared to the physical dimensions of the scatterer, i.e., the Rayleigh scattering regime. We do this by imposing the following constraint for the soft and hard targets,

$$ka << 1, \tag{5.14}$$

and for the fluid target,

$$ka << 1, \;\; k_1 a << 1. \tag{5.15}$$

Under condition (5.14), for the Rayleigh scattering regime, it was shown in [1] that the scattered acoustic field due to soft and hard cylinders can be compactly and accurately approximated. The approximate field can be represented as the sum of fields pertaining to simple monopole sources located within the cylinder, i.e.,

$$\begin{aligned}
\tilde{P} &= \tilde{B}_0 H_0^{(1)}(kr) + \tilde{B}_1 H_0^{(1)}\left(kR\left(a^2/b\right)\right) + \tilde{B}_2 H_0^{(1)}\left(kR\left(-a^2/2b\right)\right), \\
\tilde{B}_0 &= -A_0 H_0^{(1)}(kb) - \tilde{B}_1 J_0\left(ka^2/b\right) - \tilde{B}_2 J_0\left(ka^2/2b\right), \\
\tilde{B}_1 &= -\frac{A_1 H_1^{(1)}(kb) J_2\left(ka^2/2b\right) + A_2 H_2^{(1)}(kb) J_1\left(ka^2/2b\right)}{J_1\left(ka^2/b\right) J_2\left(ka^2/2b\right) + J_2\left(ka^2/b\right) J_1\left(ka^2/2b\right)}, \\
\tilde{B}_2 &= \frac{A_1 H_1^{(1)}(kb) J_2\left(ka^2/b\right) - A_2 H_2^{(1)}(kb) J_1\left(ka^2/b\right)}{J_1\left(ka^2/2b\right) J_2\left(ka^2/b\right) + J_2\left(ka^2/2b\right) J_1\left(ka^2/b\right)}.
\end{aligned} \tag{5.16}$$

Equation (5.16) reduces the exact scattered pressure field in Eq. (5.4) represented by an infinite sum to the compact sum of fields due to three line sources located within the cylinder at the polar coordinates $(0, \theta_b)$, $\left(a^2/b, \theta_b\right)$, and $\left(-a^2/2b, \theta_b\right)$ for a source located at (b, θ_b) (see Figure 17).

Later, it was shown again under conditions (5.14) and (5.15) in [3] that the scattered field due to soft, hard, and fluid targets can be expressed somewhat more accurately in terms of monopole and dipole sources, i.e.,

$$P = B_0 H_0^{(1)}(kr) + B_1 H_0^{(1)}\left(kR\left(a^2/b\right)\right) + B_2 H_1^{(1)}(kr)\cos\theta,$$

$$B_0 = -A_0 H_0^{(1)}(kb) + A_2 \frac{H_2^{(1)}(kb)}{J_2\left(ka^2/b\right)} J_0\left(ka^2/b\right), \tag{5.17}$$

$$B_1 = -A_2 \frac{H_2^{(1)}(kb)}{J_2\left(ka^2/b\right)},\ B_2 = -2A_1 H_1^{(1)}(kb) + 2A_2 \frac{H_2^{(1)}(kb)}{J_2\left(ka^2/b\right)} J_1\left(ka^2/b\right).$$

Equation (5.17) reduces the exact scattered field in Eq. (5.4) to the sum of fields due to simple linear sources located inside the cylinder with a monopole and dipole source co-located at the center of the cylinder (0, 0) and a monopole source located at $\left(a^2/b, \theta_b\right)$.

In both Eqs. (5.16) and (5.17), the $\tilde{B}_i$ and B_i coefficients are in terms of the A_n coefficients defined in Eqs. (5.10)–(5.12) for the soft, hard, and fluid targets, respectively. The accuracy of the uniform asymptotic solutions was explored in Refs. [1] and [3]. They have second order accuracy or greater with respect to the dimensionless radius of the cylinder, *ka*, and are valid over the entire domain outside the cylinder, $r, b \geq a$. Explicit comparison of the two uniform asymptotic solutions for soft and hard targets is shown in Fig. C.1 and C.2, respectively, of [3].

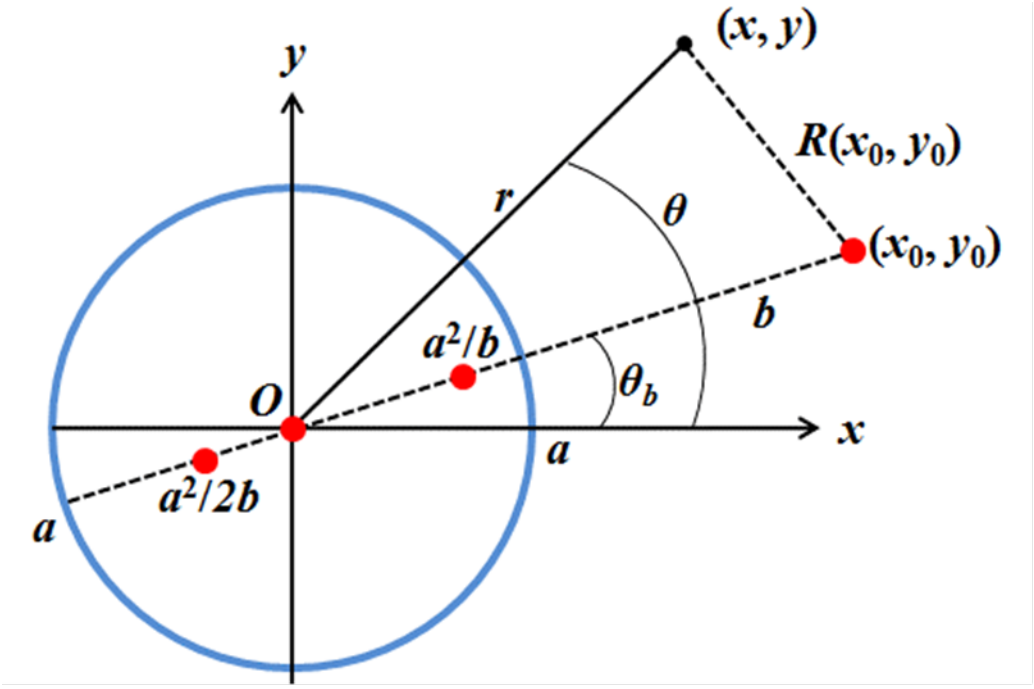

Figure 17. Two-dimensional cross-section of the geometry of scattering of low-frequency sound by a cylindrical target in free space. Depicted is the acoustic pressure line source located at the coordinates (x_0, y_0) outside of an infinite cylindrical scatterer of radius a and axis at (0, 0). The field observation point is located at (x, y). Additionally shown are the coordinates of three image acoustic line sources located within the cylinder at the polar coordinates $(0,\theta_b)$, $(a^2/b,\theta_b)$, and $(-a^2/2b,\theta_b)$. The distance R is formally defined in Eq. (5.1) and employed from Eq. (5.16) onward.

2. Scattering by an Object Near a Boundary

Consider the cylindrical wave source and cylinder previously described (see Figure 17). Now, introduce to the free space scattering problem an acoustic reflective boundary located a vertical distance D above the center of the scatterer (0, 0). The interface is described by the plane $(x,y,z)=(x,D,z)$ (see Figure 18). We will consider only acoustically soft and hard interfaces subject to the following boundary conditions at the interface-for the soft interface [61],

$$p_{in} + p_{sc} = 0, \quad y = D, \tag{5.18}$$

and for the hard interface [61],

$$\frac{\partial p_{in}}{\partial y} + \frac{\partial p_{sc}}{\partial y} = 0, \quad y = D\,. \tag{5.19}$$

These equations are analogous physically to that for the boundary conditions at the surface of the cylinder in Eqs. (5.7) and (5.8), respectively. The exact and approximate free space Green's functions that describe the total acoustic field no longer satisfy either of the boundary conditions at the interface.

3. Single Scattering Approximation (SSA)

The SSA is a first-order approximation to solving problems that involve multiple-scattering. Multiple scattering arises from the introduction of the boundary and the SSA model has appeared in the literature [19], [22]. The method allows for only single scattering from the target while strictly enforcing the boundary condition at the interface. Single scattering implies that sound is only incident upon the cylinder by a direct and single indirect path. The direct path is the same as for in free space. The indirect path allows for sound to first reflect off of the interface and then to be incident upon and diffracted by the cylinder. The resultant scattered field is the single-scatter field.

In the context of image sources, the formulation of this approximation is geometrically and intuitively constructed in terms of simple linear sources within the Rayleigh regime using either of the uniform asymptotic solutions expressed in Eqs. (5.16) and (5.17) coupled with the method of images. The construction is simple; the original source will generate a respective image source satisfying the boundary condition at the interface. Next, both monopole sources generate cylindrical waves that are incident upon and diffracted by the cylinder. Then, the total scattered acoustic field can be represented approximately as the field due to the sum of fields due to simple sources located within the scatterer. Lastly, to meet the boundary condition at the interface, these newly generated sources have respective image sources.

The total field is then the sum of fields due to the original incident field source, its respective image source, the image sources as a result of single-scattering by the cylinder, and their respective image sources in order to satisfy the boundary condition at the surface. Figure 18 depicts the SSA solution using the free space Green's function composed of three

monopole sources as expressed in Eq. (5.16). The image source coordinates and amplitudes are determined by the boundary condition at the interface. For perfect (hard or pressure release) plane boundaries, the images sources will be mirrored about the line $y = D$. The respective amplitudes of the image sources will be the same as the original sources, but may change sign. Specifically, for the soft interface an image monopole and image dipole's *x*-component of amplitude changes sign, and for the hard interface an image dipole's *y*-component of amplitude changes sign.

Interestingly, the same source geometry exists for all scatterers and boundaries considered, and only differ in their amplitudes. The Green's function describing the total field is the sum of fields due to the same sources at the same coordinates only with differing complex amplitudes. The approximate solution exactly satisfies the 2-D Helmholtz equation (5.2) and is valid everywhere on and outside the surface of the scatterer within the lower half-plane described by the interface, $r \geq a,\ y \leq D$. The approximation satisfies the boundary condition exactly at the interface $y = D$, but through its construction is not forced to and so only approximately satisfies the boundary at the surface of the cylinder, $r = a$.

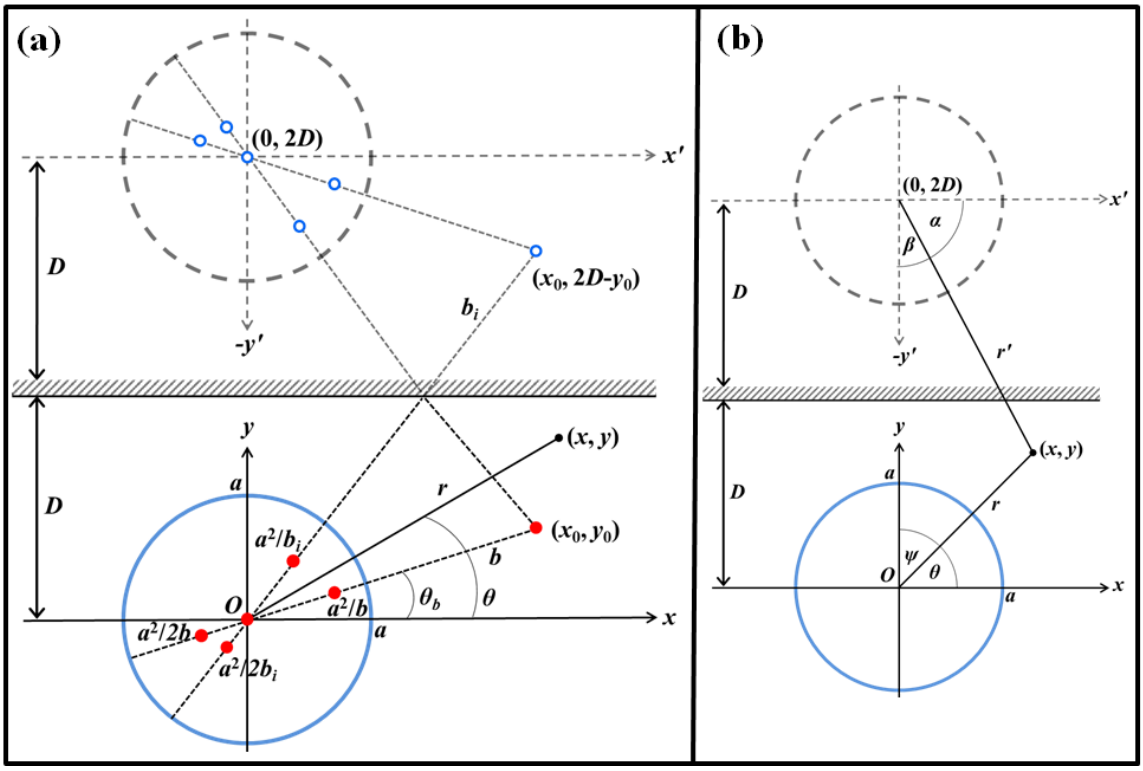

Figure 18. Geometry of single scattering of low-frequency sound by a cylindrical target near a boundary. Plot (a) depicts the entire single scattering geometry including incident wave source, its respective image, and the resulting image sources. Plot (b) depicts the angles used in developing single scattering and iterative solutions.

4. Multiple Scattering

Single scattering of sound is only the first approximation to the scattering problem described in V.B.2. In reality, the resultant single scattered sound field propagates towards and reflects off of the interface and is reincident upon and diffracted by the scatterer a second time. The resulting scattered field solution after satisfying the boundary condition at the interface can be described as the double-scattering approximation. Moreover, this physical process continues indefinitely and describes the physical process of multiple scattering. The total field is then due to an infinite sum of infinitely many scatterings and reflections. The accuracy of the SSA solution is a measure of how relatively significant the contribution of these later multiple scatterings are individually or in summation when compared to the single-scattered field.

C. IMAGE SCATTERING MODEL (ISM)

Generally, multiple-scattering problems are solved numerically without much physical insight into the complex scatterer-interface interactions that occur [37]. Other approaches involve solving an infinite set of equations for the amplitudes of individual partial waves. However, here, through the use of the known free-space scattered field expression (5.16), one can geometrically visualize the resulting successive multiple-scattering interactions occurring for this problem. The depiction of the resulting SSA model in Figure 18 and its description of construction can be iteratively repeated to construct higher-order multiple-scattering approximations simply by continuously using Eq. (5.16) coupled with the method of images.

It is important to realize that the uniform asymptotic solution in the form of Eq. (5.17) was appropriate for the SSA method outlined in V.B.3, however, it does not apply here in the same way because multiple scattering would require dipole source-target scattering interactions which we have not defined previously.

1. Generalized Method

In the Rayleigh scattering regime, the scattered acoustic field due to sound from a monopole source incident upon a soft, hard, or fluid cylinder can be described approximately as the field due to three monopole sources [1], [3]. In this respect, physically every source-target scattering interaction "creates" three new monopole sources within the target approximately satisfying the boundary condition at the surface of the cylinder, $r = a$. Subsequently, each new monopole source created from scattering, in turn, creates an image source to exactly satisfy the boundary condition at the interface, $y = D$. It follows that a solution to the problem for low-frequency cylindrical wave diffraction by a cylinder near an interface can be constructed entirely geometrically through iteration. We will refer to this geometrically constructed solution as the Image Scattering Model (ISM).

The ISM's resulting Green's function as the sum of fields due to a collection of simple sources describes an analytic multiple-scattering solution to the problem of low-frequency scattering of sound by a soft, hard, and fluid cylinder near a soft or hard interface. The solution is the sum of fields due only to monopole cylindrical sources of the form in

(5.1). The solution exactly satisfies the 2-D Helmholtz equation (5.2) and is valid everywhere on and outside the surface of the scatterer within the lower half-plane described by the interface, $r \geq a,\ y \leq D$. It satisfies the acoustic boundary condition exactly at the interface $y = D$, and unlike for the SSA model, through iteration, it additionally satisfies the boundary condition at the surface of the cylinder, $r = a$.

Some geometries and scattering scenarios (type of scatterer, interface, *ka* values, etc.) required significantly more iterations to acceptably satisfy the boundary condition at the surface of the cylinder, $r = a$. A specific example would be the scattering problem of a soft target near a hard interface when $D = O(a)$. A linear increase in the number of iterations requires an exponential increase in the number of sources required due to multiple scattering. Additionally, and computationally expensively, multiple-scattering yields to the continual generation of sources not collocated at the axes of the real and image cylinder.

2. Dipole Correction

In seeking to develop a more numerically efficient algorithm, we modified the previous approach to take advantage of the more accurate uniform asymptotic solution from Eq. (5.17). Equation (5.17), beyond being shown to be more accurate than Eq. (5.16) [3], additionally and more importantly contains two sources at the origin as a result of every monopole source-target scattering interaction. However, this solution requires dipole scattering by cylinders.

To use the known solution (5.17), the previous algorithm may still be employed by making two modification within the previously described approach. First, every new dipole resulting from monopole source-target interaction can be written in terms of its amplitude components in the *x* and *y* directions, thereby allowing summation and collapse of all the generated dipoles into only two dipoles at the center of the scatterer $(0,0)$ and also at the center of the image cylinder $(0,2D)$. And second, the dipole source-target scattering interactions that arise every iteration from the two new image dipoles at the center of the

image scatterer can be approximated using Graf's addition theorem [49] by rewriting the dipoles in terms of monopoles. Using Graf's addition theorem [49]

$$H_0^{(1)}\left(kR\left(d\right)\right)=\sum_{m=-\infty}^{\infty}J_m\left(kd\right)H_m^{(1)}\left(kr\right)\cos m\theta\,, \tag{5.20}$$

and under the condition that we select *d* specifically so that $kd << ka << 1$, then writing out the first few terms yields,

$$\begin{aligned}H_0^{(1)}\left(kR\left(\pm d\right)\right)&=J_0\left(kd\right)H_0^{(1)}\left(kr\right)\pm 2J_1\left(kd\right)H_1^{(1)}\left(kr\right)\cos\theta\\&+2J_2\left(kd\right)H_2^{(1)}\left(kr\right)\cos 2\theta+O\left(\left(d/r\right)^3+\left(kd\right)^3/\sqrt{kr}\right).\end{aligned} \tag{5.21}$$

The error in the approximation can be reduced with appropriate selection of *d*. Manipulation of (5.21) for plus and minus *d*, and in terms of the angles shown in Figure 18b, results in

$$H_1^{(1)}\left(kr\right)\cos\alpha\approx\frac{H_0^{(1)}\left(kR\left(d,0\right)\right)-H_0^{(1)}\left(kR\left(-d,0\right)\right)}{4J_1\left(kd\right)}, \tag{5.22}$$

$$H_1^{(1)}\left(kr\right)\sin\alpha\approx\frac{H_0^{(1)}\left(kR\left(0,d\right)\right)-H_0^{(1)}\left(kR\left(0,-d\right)\right)}{4J_1\left(kd\right)}. \tag{5.23}$$

These equations represent a general expression for writing the two new image dipoles at the center of the image cylinder at the beginning of each iteration in terms of two image monopoles each, respectively. Thus, approximate dipole scattering by cylinders is achieved and, ultimately, an algorithm for which there is a significant numerical savings due to the consolidation of sources is allowed. Both algorithms were shown to converge to the boundary conditions at the surface of the cylinder, $r = a$, at roughly the same rate per loop, however, the latter had the practical significant computational efficiency due to the reduction of sources in the iterative solution.

3. Metrics for Error Comparison

An exact, general, and known analytic solution to this problem does not exist for all geometries and parameters compare to as was done for the free-space scattering solution error analysis [1], [3]. This problem is readily solved in various ways using numerical methods. However, this was not the approach used to quantify error since we desired to develop a way to quantify the accuracy of the solution within the algorithm per iteration.

This task could have been very difficult to generalize without solving an entirely different numerical problem which was not the desire nor, most likely, numerically efficient.

Due to the iterative nature of the solution, at the completion of every iteration is an approximate solution that models the n^{th} multiple scattering. The solution exactly satisfies the boundary condition at the boundary through construction. At every iteration completion, the approximate solution is the field due to the set of sources that have been geometrically generated thus far. Since the scattered field exactly satisfies the 2-D Helmhotlz equation (5.2) and the interface boundary condition, and is valid everywhere within the domain $r \geq a,\ y \leq D$, all that is required for a solution is to satisfy the boundary condition at the surface of the cylinder. As a result, the error discrepancy in satisfying the latter is a metric for the convergence of the method after every iteration.

Based on the total field as represented by the sum of simple (however, many) sources, both the pressure and radial derivative of the acoustic pressure field can be easily calculated at a set number of points uniformly distributed along the surface of the cylinder at each iteration. As per comparison, the SSA is the solution after the first iteration, and this computation can be done prior to the algorithm for the separate cases of the free-space solution (in the absence of the scatterer and the interface) and for the free-space scattering solution (in the absence of the interface). The metrics then take the form of the geometric norms

$$L^{(S)} = \sum_{m=0}^{M-1} \left| p_{in} + p_{sc}^{(S)} \right|^2_{r=a,\ \theta=2\pi m/M} , \tag{5.24}$$

$$L^{(H)} = \sum_{m=0}^{M-1} \left| \frac{\partial p_{in}}{\partial r} + \frac{\partial p_{sc}^{(H)}}{\partial r} \right|^2_{r=a,\ \theta=2\pi m/M} , \tag{5.25}$$

where (*S*) and (*H*) represent metrics for the soft and hard cylinders, respectively, and the quantities within the absolute values are the boundary conditions in Eqs. (5.7) and (5.8). Thereby, these sums should decrease per iteration in order to show convergence of the algorithm.

For the fluid cylinder (*F*) the boundary conditions represented in Eq. (5.9) require knowledge of the field inside the cylinder, p_F. The ISM described thus far only describes

an approximate solution for the total field outside of the cylinder and is valid only over the domain $r \geq a,\ y \leq D$. Therefore, we cannot simply implement a direct-boundary condition computation as a metric, as was done for the soft and hard scatterers. Here, we instead exploit the periodic nature of both the acoustic pressure field and its radial derivative inside and outside the scatterer with respect to the angle θ. The metric for fluid then can be developed through the evaluation and matching term by term the respective theoretical and calculated Fourier coefficients for each individual partial wave.

As before, the total pressure and its radial derivative are analytically calculated uniformly over the surface of the cylinder. Then, due to the periodicity of these data sets over [0, 2π], we may take the discrete Fourier transform of both computed data sets denoting them as F_n and $\tilde{F}_n$, respectively. Following from Eq. (5.6), we can rewrite the following general forms of the acoustic pressure field and its radial derivative within the fluid, evaluated at the surface of the cylinder as

$$p_F\big|_{r=a} = \sum_n Q_n J_n\left(k_1 a\right) e^{in\theta}, \quad \left.\frac{\partial p_F}{\partial r}\right|_{r=a} = k_1 \sum_n Q_n J_n'\left(k_1 a\right) e^{in\theta}, \tag{5.26}$$

where Q_n here serves as an undetermined (and unimportant) coefficient. Then the metric for the fluid can be formed by analyzing the calculated Fourier coefficients (F_n and $\tilde{F}_n$) and the theoretically predicted ones that simply arise from Eq. (5.26). Additionally, we have chosen to weight lower order coefficients more importantly. The final metric for fluid becomes

$$L^{(F)} = \sum_n \left| \frac{\tilde{F}_n}{F_n} - \frac{k_1}{M_F} \frac{J_n'\left(k_1 a\right)}{J_n\left(k_1 a\right)} \right|^2 \left| \frac{F_n}{F_0} \right|^2 . \tag{5.27}$$

4. Least Square Correction

Now that we have developed metrics to quantify error in the iterative solution, we can additionally use these metrics to improve our solution and ultimately ascertain a near-exact solution. The latter helps to quantify the accuracy of the strictly geometric approximations formed in the previous sections. At the completion of each iteration and after computation of the metric for the current state, the current solution, $p = p_{in} + p_{sc}$, is

the field due to the set of sources generated thus far geometrically. However, we can assume that there exists a more accurate solution of the form, $p_{LS} = p + \hat{p}$, where $\hat{p}$ represents a correction, and is the field due to additional sources and harmonics with unknown amplitudes located at the center of the scatterer and their respective images located at the center of the image cylinder.

By representing the field $\hat{p}$ in this way allows the interface boundary condition to be satisfied exactly. We then can form a system of linear independent equations using the quantities within the absolute values of Eqs. (5.24), (5.25), and (5.27), however replacing p in these expressions with p_{LS}. One can then form analytically a least square problem to solve for the respective complex amplitudes of these new simple sources and thereby develop a more accurate p_{LS} solution to the problem. Based on the formation of the least square solution, the resulting field p_{LS} is still an analytic solution in terms of simple sources that exactly satisfies the 2-D Helmholtz equation and is valid over the same domain, $r \geq a,\ y \leq D$.

D. GEOMETRY OF MULTIPLE SCATTERING

The resulting Green's function for all scatterer and interface types is the sum of fields due to a set of monopole and dipole sources of cylindrical waves. The locations of the specific sources are the same for all scatterer and interface types and only differ by their complex amplitudes. Here, we explore the geometry of multiple scattering by a cylinder near a boundary.

Figure 19 shows the set of real and image cylindrical wave sources (marker 'o') for the iterative solution of a scattering problem in various levels of magnification. Also shown are two prominent source clustering points at $x = 0$, $y = a^2/2D$ (marker '+') and $x = 0$, $y = D-(D^2-a^2)^{0.5}$ (marker '×'), both of which can be geometrically determined (not derived here). Figure 19a shows the entire scattering geometry, which includes the physical source ($x = 1.5a$, $y = -1.5a$), source image ($x = 1.5a$, $y = 4.5a$), the acoustic boundary (x, $y = 1.5a$), scattering cylinder with axis at $x = 0$, $y = 0$, and image cylinder with axis at $x = 0$, $y = 3a$.

Inherent to the iterative nature of the solution, there will be an exponential increase in the number of image sources with respect to iterations (n). The image sources cluster around points. This is not very apparent from inspection of Figure 19a due to the scale of the figure. Figure 19b represents an expanded view of the highlighted square (red) in Figure 19a. This allows more image sources located within the scatterer to become visible. The structure of the sources relative to the two previously mentioned cluster points is further revealed through comparison of the expanded view of Figure 19b (seen in Figure 19c) to that of Figure 19d. In comparison of these two figures, we see a repeating structure inherent in the set of points that make up the solution. Interestingly (not shown) is that one could continually expand Figure 19d in the same manner and reveal the same pattern of nested image sources. This pattern of points surrounding the '×' marker is determined by the initial scattering geometry. And the number of nested points is determined by the number of iterations that make up the solution. Significant consolidation of the sources in the highlighted square into single clustering points was determined to reduce the accuracy of the solution.

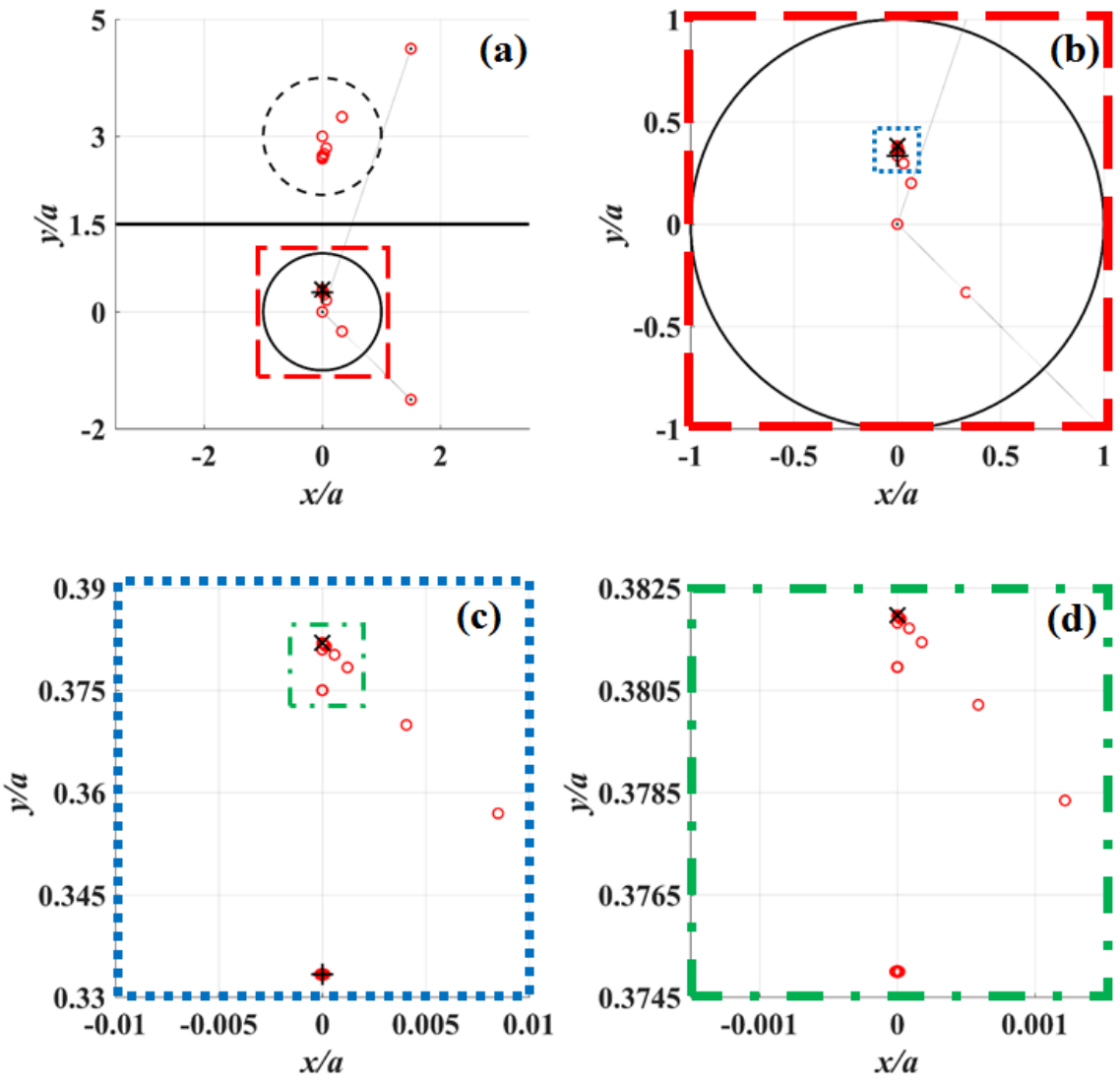

Figure 19. Geometry of multiple scattering due to cylinder near a boundary. Plots show the set of real and image cylindrical wave sources (marker 'o') for a convergent solution of the image scattering model. Also shown are two prominent source collection points at $x = 0$, $y = a^2/2D$ (marker '+') and $x = 0$, $y = D-(D^2-a^2)^{0.5}$ (marker '×'). Plot (a) shows the entire scattering geometry, which includes the physical source ($x = 1.5a$, $y = -1.5a$), source image ($x = 1.5a$, $y = 4.5a$), the acoustic boundary (x, $y = 1.5a$), scattering cylinder with axis at $x = 0$, $y = 0$, and image cylinder with axis at $x = 0$, $y = 3a$. Plot (b) is an expanded view of the highlighted square in plot (a). Similarly, (c) is an expanded view of the highlighted square in (b), and (d) is an expanded view of the highlighted square in (c).

E. CONVERGENCE OF THE ITERATIVE SOLUTION

The accuracy of the ISM model was numerically evaluated through the use of MATLAB (MathWorks, Natick, MA) by comparing it to a near-exact numerical solution of the problem that was obtained by adding cylindrical harmonics up to the third order with unknown amplitudes to the iterative solution. The amplitudes of the harmonics were determined from a least square correction to the total field as discussed in Section V.C.4.

Figure 20 shows the accuracy of the total pressure field due to a cylinder near a boundary. Plots show the convergence metric relative to free space scattering by a cylinder as a function of iterations (n). Convergence metrics are shown for solutions of the problem of scattering by soft, hard, and fluid (M = 0.375, s = 1.5) cylinders near pressure release (soft) and rigid (hard) boundaries a distance $D = 1.5a$ above the cylinder for a cylindrical wave source located at $x = 2a$, $y = 0$. All plots in this figure show exponential increase in accuracy with iterations until reaching a converged solution. Interestingly, in some cases the least square correction allows for improvement relative to the free space scattering of a cylinder. We see that the soft scatterer requires more iterations to reach a converged solution relative to the hard and fluid scatterers. This is because the scattered field due to a soft scatterer is relatively much stronger.

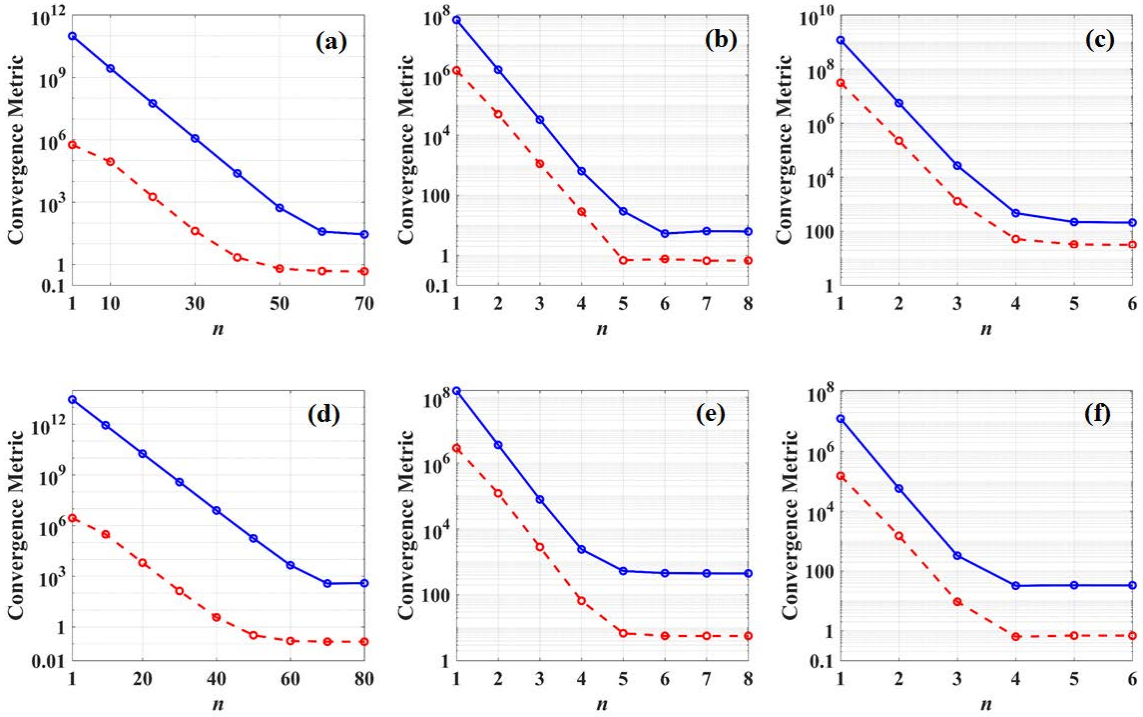

Figure 20. Accuracy of the total pressure field due to a cylinder near a boundary. Plots show the convergence metric relative to free space scattering by a cylinder as a function of iterations (n). Solutions are shown for the image scattering model (solid curves) and the solution with least-square correction (dashed curves) for soft (a), (d), hard (b), (e), and fluid (M = 0.375, s = 1.5) (c), (f) cylinders with dimensionless radius ka = 0.01 near pressure release (soft) (a), (b), and (c) and rigid (hard) (d), (e), and (f) boundaries a distance $D = 1.5a$ above the cylinder for a cylindrical wave source located at $x = 2a$, $y = 0$.

Figure 21 presents convergence rates for the total pressure field due to scattering by a soft cylinder near a pressure release boundary much like Figure 20a. Here, we compare geometric parameters that characterize the scattering problem. As the distance from the boundary to the scatterer increased overall, the model requires less iterations (cf. Figure 20a and Figure 21a). This result is expected since ultimately the free-space scattering solution should be approximated as D gets large relative to a and the wavelength. In this limit we expect multiple scattering to become less significant. Additionally, as frequency decreases while a remains fixed, we see that more iterations are required for a solution (cf. Figure 20a and Figure 21b). This result is attributed to the free space scattering uniform asymptotic increase in accuracy since its error is proportional to $O(k^2a^2)$.

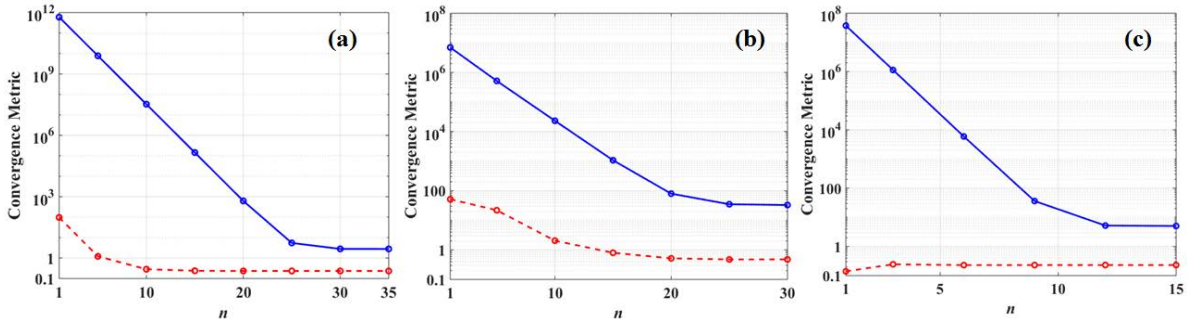

Figure 21. Convergence rates for the total pressure field due to scattering by a soft cylinder near a pressure release boundary. Plots show the convergence metric relative to free space scattering by a cylinder as a function of iterations (n). Solutions are shown for the image scattering model (solid curves) and the solution with least-square correction (dashed curves) for the following geometric parameters (boundary distance D and dimensionless radius of the cylinder ka) to characterize the scattering problem: $D = 5a$, $ka = 0.01$ (a), $D = 1.5$a, $ka = 0.1$ (b), $D = 5a$, $ka = 0.1$ (c). The source of cylindrical waves is located at $x = 2a$, $y = 0$.

F. ENERGY STREAMLINES

In this section, we illustrate the utility of the virtual source technique we developed for investigating multiple scattering problems and the physical insight into scattering that it provides. Using the ISM solution, we compute and present energy streamlines for the total acoustic field in proximity of the scatterer and the boundary where we expect the greatest distortion of the field. We consider the scattering by soft, hard, and fluid targets near pressure release (soft) and rigid boundaries (hard) for comparison. Because the solution for the total pressure field is expressed simply as the sum of monopole and dipole sources allows for convenient analytic development and calculation of expressions for the total pressure and the time-averaged power-flux density (**J**) (3.48) valid over the entire domain, $r, b \geq a$ and $y \leq D$. A physical description and discussion of **J** is presented in Chapter III.F and is not reproduced here.

The model parameters used will describe sound scattering by an underwater cylindrical target of radius a = 1 m with axis at $x = y = 0$. The target is submerged in seawater with constant sound speed c = 1500 ms^{-1} and density ρ = 1025 kgm^{-3}. A line source is parallel to the target's axis and emits monochromatic cylindrical waves at

frequency f = 23.87 Hz. The cylindrical wave source is located at $x \equiv b = 10a$, $y = 0$. For these parameters, ka = 0.1, which is within the Rayleigh scattering regime. Hence, the asymptotic error is small when using the free space scattering approximation and we expect a negligible error overall in calculating the energy streamlines.

Figure 22 presents the power flux streamlines using the solutions from the SSA and ISM models for scattering by soft cylinders near pressure release (soft) and rigid (hard) boundaries a distance D = 1.5a above the cylinder. The figures show clearly that the SSA and ISM model have very clear distinctions when the soft scatterer is relatively close to the boundary. Figure 22a shows the SSA model predicts non-zero power flux into the soft cylinder which is unphysical.

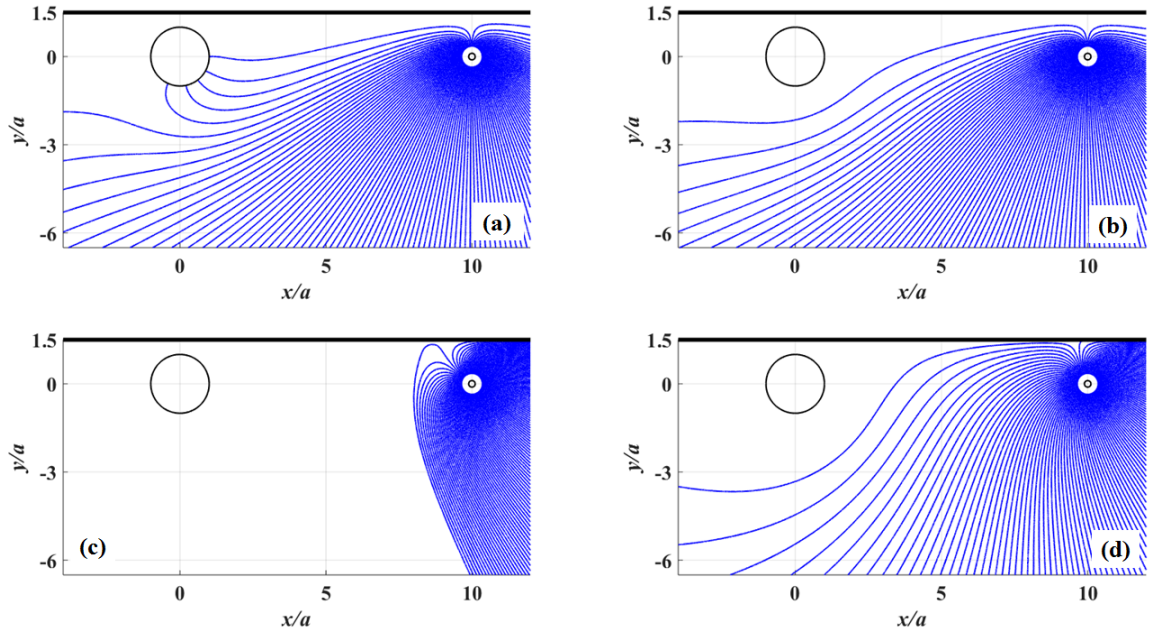

Figure 22. Power flux streamlines for soft cylinders near a boundary. Solutions are shown for the single scattering approximation (a), (c) and the image scattering model (b), (d) for soft cylinders with dimensionless radius ka = 0.1 near pressure release (soft) (a), (b) and rigid (hard) (c), (d) boundaries a distance D = 1.5a above the cylinder for a cylindrical wave source located at x = 0, y = 0.

Figure 23 presents a similar plot as shown in Figure 22. Here, all parameters are the same except $D = 5a$. The figures show that the SSA and ISM model again have very clear distinctions, as was previously seen in Figure 22. As before, the SSA model erroneously predicts non-zero power flux into the soft cylinder. Somewhat surprisingly, the differences between the SSA and ISM models persist for a larger distance D for the soft scatterer.

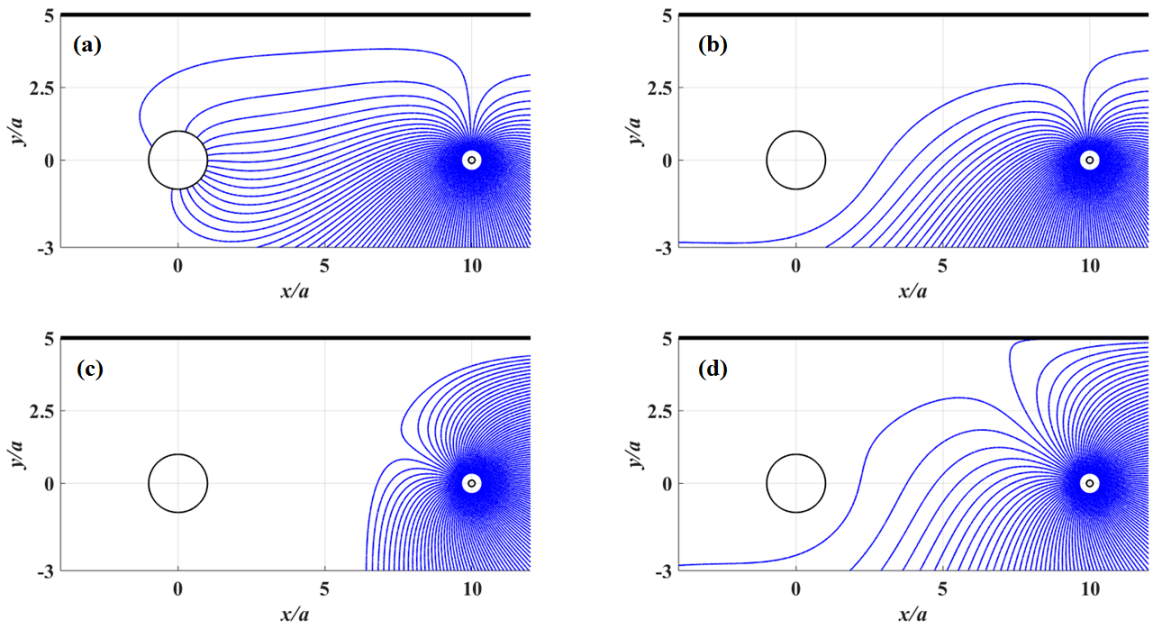

Figure 23. Power flux streamlines for soft cylinders near a boundary. All parameters are the same as in Figure 22 except $D = 5a$.

Figure 24 and Figure 25 present power flux streamlines using the ISM solution for scattering by hard and fluid ($M = 0.375$, $s = 1.5$) cylinders near pressure release (soft) and rigid boundaries a distance $D = 1.5a$ and $D = 5a$, respectively, above the target. The figures show that the pressure release boundary dominates the scattering problem and that the field is only strongly distorted in the immediate proximity of the scatterer. The SSA and ISM model solutions yielded similar results with respect to energy streamlines for the parameters chosen, therefore only ISM results are presented.

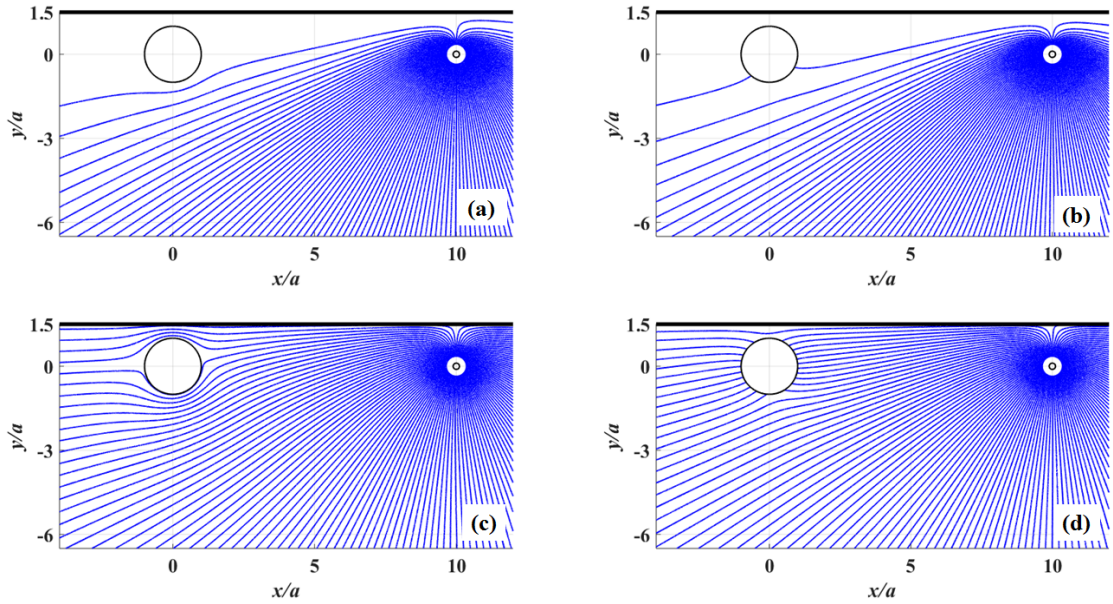

Figure 24. Power flux streamlines for hard and fluid cylinders near a boundary. Solutions are shown for the image scattering model for hard (a), (c) and fluid (M = 0.375, s = 1.5) (b), (d) cylinders with dimensionless radius ka = 0.1 near pressure release (soft) (a), (b) and rigid (hard) (c), (d) boundaries a distance $D = 1.5a$ above the cylinder for a cylindrical wave source located at x = 0, y = 0.

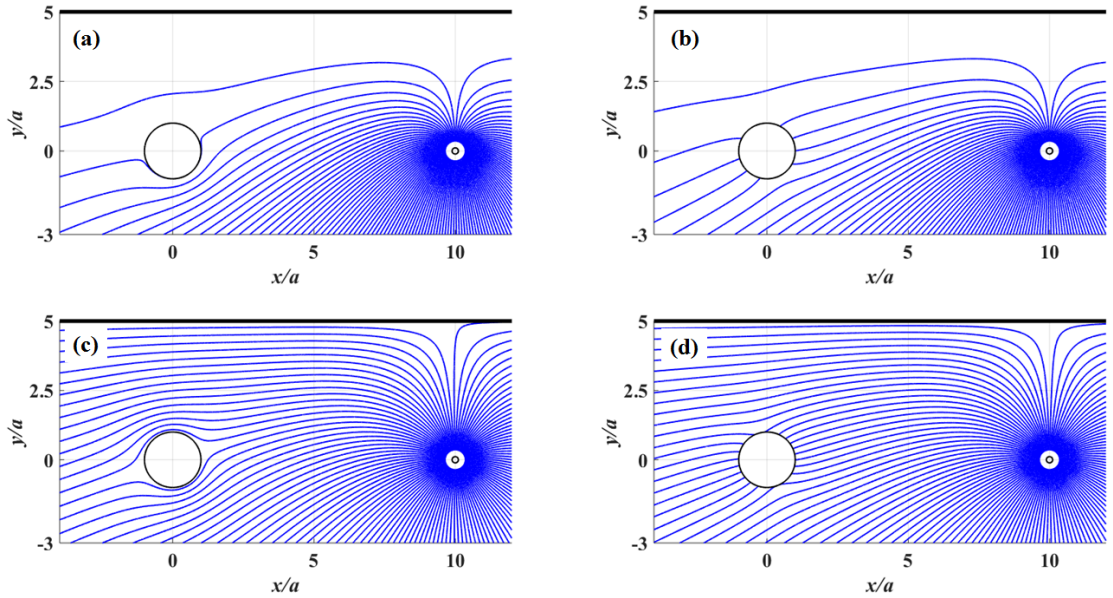

Figure 25. Power flux streamlines for hard and fluid cylinders near a boundary. All parameters are the same as in Figure 24 except $D = 5a$.

G. CONCLUSIONS

In this chapter, we have developed an efficient, semi-analytical approach to model multiple scattering of low-frequency sound by an object near a boundary. The approach builds on 2-D asymptotic solutions for scattering in an unbounded fluid [1], [3] in terms of image sources and has been implemented numerically for cylindrical scatterers. Convergence accuracy of the model has been confirmed through comparison with a near-exact numerical solution of the problem.

The model iteratively calculates single, double, and various subsequent orders of multiple scattering allowing physical insight into multiple scattering for this problem. The solution is valid within the Rayleigh scattering regime for soft, hard, and fluid cylinders in proximity of pressure release and rigid boundaries. The resulting Green's function for all scatterer and interface types is the sum of fields due to a set of monopole and dipole sources of cylindrical waves. The locations of the specific sources are the same for all scatterer and interface types and only differ by their complex amplitudes. Image source geometry was explored and shown to contain a pattern to its structure. The solution exactly satisfies the 2-D Helmholtz equation and is valid for arbitrary positions of the source and receiver relative to the cylinder and the interface. It satisfies the acoustic boundary condition at the interface and at the surface of the cylinder.

Because the solution is a set of simple linear sources, it allows for analytic computation of various acoustic quantities. Time-averaged power-flux density was calculated and presented as energy streamlines for soft, hard, and fluid targets near pressure release and rigid interfaces to provide insights into the total field distortion due to scattering by various objects.

The established semi-analytic solution as composed of only image sources suggest a mathematically convenient path forward in a number of multiple scattering problems where analytic solutions are not readily available. The methods in this chapter can be extended and applied to a number of multiple scattering problems. These results can be extended to model normal mode representation, scattering of two targets, and to 3-D problems including low-frequency scattering of sound by a sphere near a plane interface.

Another application would be the extension to electromagnetic waves for Rayleigh scattering applications.

VI. CONCLUSION

This dissertation is a collection of four peer-reviewed journal articles in various stages of publication [1]–[4]. The focus of the study pertains to the acoustic wave scattering by objects when the scattering object's dimensions are small compared to the wavelength, i.e., the Rayleigh scattering regime. Rayleigh scattering is generally studied assuming plane incident waves [10]–[14]. However, in a multitude of problems, the plane wave solution is not sufficient. In general, when knowledge of the full Green's functions, rather than the plane-wave and far-field approximations, becomes necessary, then numerical methods are used in the development of solutions [15]–[22]. In this dissertation we develop compact analytic and semi-analytic solutions for sound scattering by a cylinder and illustrate the solution to several problems in underwater acoustics.

In Chapter II, the method of matched asymptotic solutions that was developed for spherical targets [32], [33] is extended to wave scattering by an infinite cylinder with a radius that is small compared to the wavelength. Scattering of cylindrical waves by acoustically soft and hard cylinders within a homogenous medium has well known solutions [14] in terms of infinite sums. In this chapter, uniform asymptotic solutions within the Rayleigh regime have been found for acoustically soft, hard, and impedance cylinders. The solutions are valid over the entire domain outside the cylinder to second order accuracy or greater with respect to *ka*, the dimensionless radius of the cylinder. The uniform asymptotic solutions of the scattered wave satisfy the Helmholtz equation exactly and have a rather simple and intuitive form as the field due to three image line sources located at the center of the cylinder $(0,0)$, and at the points $\left(a^2/b,0\right)$ and $\left(-a^2/2b,0\right)$ [1].

In Chapter III, the techniques previously applied to the sphere [32], [33] and to the soft, hard, and impedance cylinder [1] are applied to the more complex and realistic fluid and solid scatterers. The classic problem of cylindrical wave scattering by fluid and solid cylinders has well known solutions [28], [29]. The solutions are described in terms of an infinite sum of partial waves. The partial wave scattering amplitudes are determined by the boundary conditions at the surface of the cylinder. In this chapter, uniform asymptotic

solutions for the scattered field have been derived through the method of matched asymptotic expansions for fluid and solid cylinders. Additionally, these asymptotic solutions provide a further improvement of the solution derived in Chapter II for acoustically soft, hard, and impedance cylinders. The established solutions have second order accuracy or greater with respect to the dimensionless radius of the cylinder, *ka*, and are valid over the entire domain outside the cylinder. The uniform asymptotic solution represents solutions for fluid, solid, soft, hard, and impedance boundary conditions in one compact expression that exactly satisfies the Helmholtz equation. The locations of the sources are the same for all scattering targets and are independent of sound frequency. The uniform asymptotic solution is the field due to three linear sources-a monopole and a dipole source both located at the axis $(0,0)$ of the cylinder and a monopole source located at $\left(a^2/b,0\right)$ [3].

The developed uniform asymptotic solutions of Chapters II and III offer a physically intuitive form and mathematically simple representation of the scattered wave as a field due to a few image sources that suggest a possible path forward in a number of low-frequency diffraction and scattering problems. Compact analytic solutions can also provide physical insights leading to new applications. Two applications of these solutions are discussed in Chapters IV and V.

In Chapter IV, the acoustic Green's functions for cylindrical scatterers [1], [3], which are derived in Chapters II and III, and spherical scatterers [32], [33] are used to develop an approach to underwater noise mitigation. Analytic solutions for sound diffraction on cylinders and spheres streamline the necessary analysis. In this chapter, we have studied four basic sound propagation scenarios to illustrate and quantify the possibility of using diffraction (scattering) to passively suppress unwanted sound radiation. Broadband noise suppression in free space is achieved by placing a highly compliant object in the near field of a compact sound source provided that the size of the object is comparable to its distance from the source and small compared to the acoustic wavelength. Multiple nearby sources can be suppressed simultaneously by the same object. It has been shown that the proposed approach allows strong suppression of acoustic radiation by

compact sources near boundaries and in waveguides. The approach is most efficient at low frequencies where alternative absorption- and reflection-based mechanisms of noise mitigation become impractical [2].

Lastly, in Chapter V, we developed an efficient, semi-analytical approach to model multiple scattering of low-frequency sound by an object near a boundary. The approach builds on asymptotic solutions in terms of image sources and has been implemented numerically for cylindrical scatterers. The model iteratively calculates single, double, and various subsequent orders of multiple scattering. The solution is valid within the Rayleigh scattering regime for soft, hard, and fluid cylinders for soft and hard interfaces. The resulting Green's function for all scatterer and interface types is the sum of fields due to a set of monopole and dipole sources of cylindrical waves. The locations of the specific sources are the same for all scatterer and interface types and only differ by their complex amplitudes. The solution exactly satisfies the 2-D Helmholtz equation and is valid for arbitrary positions of the source and receiver relative to the cylinder and the interface. It satisfies the acoustic boundary condition at the interface and at the surface of the cylinder.

The methods in this dissertation can be extended and applied to a number of multiple scattering problems of current interest. These results can be extended to model normal mode representation of the scattered field, scattering of two nearby objects, and to 3-D problems including scattering of sound by a sphere near an interface. Another direction would be the extension to electromagnetic waves for Rayleigh scattering applications. And, additionally, comparison with the experimental work by Barton, Smith et al. [80]–[86] on acoustic intensity scattering by a hard finite cylinder and other simple shapes.

THIS PAGE INTENTIONALLY LEFT BLANK

APPENDIX A. SCATTERING AMPLITUDES FOR AN ELASTIC CYLINDER

Waves inside the elastic medium satisfy the equation of motion for the displacement **u** given in Eq. (3.11). Taking the divergence and curl of both sides of Eq. (3.11), it can be reduced to two vector differential equations for the compressional and shear waves, respectively,

$$\nabla^2\left(\nabla\cdot\mathbf{u}\right)=-\omega^2\frac{\rho_{ES}}{\lambda+2\mu}\left(\nabla\cdot\mathbf{u}\right),\quad \nabla^2\left(\nabla\times\mathbf{u}\right)=-\omega^2\frac{\rho_{ES}}{\mu}\left(\nabla\times\mathbf{u}\right), \tag{A.1}$$

such that they define the wave numbers and wave speeds. For the longitudinal (compressional) waves,

$$k_1=\omega\sqrt{\rho_{ES}/\left(\lambda+2\mu\right)},\ \ c_1=\sqrt{\left(\lambda+2\mu\right)/\rho_{ES}}\ , \tag{A.2}$$

and for the transverse (shear) waves,

$$k_2=\omega\sqrt{\rho_{ES}/\mu},\ \ c_2=\sqrt{\mu/\rho_{ES}}\ . \tag{A.3}$$

Following the same analysis as [29], except using cylindrical basis functions, the displacement within the cylinder, can be determined by expressing it as the sum of a scalar and vector potential,

$$\mathbf{u}=-\nabla\Psi+\nabla\times\mathbf{A}\,, \tag{A.4}$$

with

$$\Psi=\sum_{n=0}^{\infty}\varepsilon_n a_n H_n^{(1)}\left(kb\right)J_n\left(k_1 r\right)\cos n\theta\,, \tag{A.5}$$

$$A_r=0,\quad A_\theta=0,\quad A_z=\sum_{n=0}^{\infty}\varepsilon_n b_n H_n^{(1)}\left(kb\right)J_n\left(k_2 r\right)\sin n\theta\,, \tag{A.6}$$

where a_n and b_n are undetermined coefficients. Substitution of Eqs. (A.5) and (A.6) into (A.4) ultimately yields equations for the polar components of the displacement within the cylinder,

$$u_r=\sum_{n=0}^{\infty}\varepsilon_n H_n^{(1)}\left(kb\right)\left[\frac{nb_n}{r}J_n\left(k_2 r\right)-a_n\frac{\partial}{\partial r}J_n\left(k_1 r\right)\right]\cos n\theta\,, \tag{A.7}$$

$$u_\theta=\sum_{n=0}^{\infty}\varepsilon_n H_n^{(1)}\left(kb\right)\left[\frac{na_n}{r}J_n\left(k_1 r\right)-b_n\frac{\partial}{\partial r}J_n\left(k_2 r\right)\right]\sin n\theta\,. \tag{A.8}$$

Also, $u_z = 0$, i.e., there is no displacement in the *z*-direction. The boundary conditions for the fluid-solid interface at $r = a$, as formalized previously in Section III.B.2 are

$$p_{in} + p_{sc}^{(ES)} = -\sigma_{rr}, \quad r = a, \tag{A.9}$$

$$u_{in,\,r} + u_{sc,\,r}^{(ES)} = u_r, \quad r = a, \tag{A.10}$$

$$\sigma_{r\theta} = \sigma_{rz} = 0, \quad r = a. \tag{A.11}$$

Where the displacement in the surrounding fluid can be computed through the use of Eq. (3.49), i.e., $\mathbf{u} = \left(1/\omega^2\rho\right)\nabla p$, σ_{rr} is the normal component of stress, $\sigma_{r\theta}$ and σ_{rz} are the tangential components of the shearing stress, which in cylindrical coordinates are defined by [29],

$$\begin{aligned} \sigma_{rr} &= \lambda\nabla\cdot\mathbf{u} + 2\mu\,\partial u_r/\partial r, \\ \sigma_{r\theta} &= \mu\left[\left(1/r\right)\partial u_r/\partial\theta + r\,\partial/\partial r\left(u_\theta/r\right)\right], \\ \sigma_{rz} &= \mu\left[\partial u_r/\partial z + \partial u_z/\partial r\right]. \end{aligned} \tag{A.12}$$

We immediately recognize that $\sigma_{rz} = 0$ since $u_z = 0$ and $u_r = u_r\left(r,\theta\right)$. The remaining stresses (σ_{rr} and $\sigma_{r\theta}$) in Eq. (A.12) can be calculated analytically given the series expressions for u_r (A.7) and u_θ (A.8). Given the exact incident p_{in} and scattered $p_{sc}^{(ES)}$ fields, their radial displacements are readily calculable using Eq. (3.49). Substitution of all of the resulting expressions into the boundary conditions Eqs. (A.9)-(A.11), yields a system of 3 linear algebraic equations with 3 unknowns: $A_n^{(ES)}$, a_n, and b_n. Only the resulting equations for the $A_n^{(ES)}$ coefficients is needed for the scattered wave in Eq. (3.5); $A_n^{(ES)}$ is given by Eq. (3.13) in Section III.B.2.

APPENDIX B. RAYLEIGH REGIME DEGENERATE CASES

In the main body of the text, for the A_n scattering amplitudes, we derived generic expressions valid in the Rayleigh regime. The scattering amplitudes are represented by the leading order term with respect to the dimensionless radius *ka*. Specific degenerate cases for the coefficients in Eqs. (3.20)–(3.23) and (3.24)–(3.29) for the fluid and solid targets, respectively, were not explored previously. From Section III.C.2, it follows that the leading order terms for the fluid and solid targets are proportional to the following dimensionless quantities: $A_0^{(F)} \propto M_F s^2 - 1$, $A_n^{(F)} \propto M_F - 1$, $A_0^{(ES)} \propto M_{ES}\left(s_1^2 - s_2^2\right) - 1$, and $A_1^{(ES)} \propto M_{ES} - 1$. The degenerate cases considered here allow for the leading order term in the scattering amplitudes previously defined to vanish. For these specific degenerate cases the second-lowest order (first non-degenerate) term will then represent the dominant scattering amplitude and leading order term. In this appendix, we present the substitutive scattering amplitude expressions for these degenerate cases and comment on the resulting scattered field wave physics.

A. FLUID CYLINDER

In the degenerate case of matched compressibility when $M_F s^2 = 1$ and $M_F \neq 1$, since $A_0^{(F)} \propto M_F s^2 - 1$, only the leading order term for the $n = 0$ coefficients shown in Eqs. (3.20) and (3.22) are affected. Under condition (3.14), substitution of Eqs. (3.16) and (3.18) into (3.9), the expression for the leading order term for the scattering amplitude becomes

$$A_0^{(F)} = -\frac{i\pi}{2}\left(M_F - 1\right)\left(\frac{ka}{2}\right)^4\left[1 - \frac{k^2a^2}{4}\left(M_F + i\pi\left(1 + \frac{2i}{\pi}\left(\ln\left(\frac{ka}{2}\right) + \gamma\right)\right)\right)\right]^{-1} \times \left[1 + O\left(k_1^2a^2 + \kappa^2\left(ka\right)\right)\right]. \tag{B.1}$$

For this degenerate case, Eq. (B.1) must be substituted for Eqs. (3.20) and (3.22) for an accurate solution. Now, the respective orders of magnitude of the first three coefficients with respect to *ka* are $A_0^{(F)}, A_2^{(F)} = O\left(k^4a^4\right)$ and $A_1^{(F)} = O\left(k^2a^2\right)$. Hence, this degenerate

case does not change the overall order of magnitude with respect to *ka* for the amplitude of the scattered field. However, now the $A_1^{(F)}$ term will be the sole dominant term for the scattered field. In the Rayleigh regime, matched compressibility between two fluids causes a fluid target to have the directivity of that due to a dipole source. Similar results are seen for the small fluid sphere through inspection of Eqs. 27, 29, and 30 in [33]. However, the leading order term for the scattering amplitude for the fluid sphere is proportional to k^3a^3 vs. k^2a^2 for the fluid cylinder.

In the degenerate case of matched densities when $M_F = 1$ and $M_F s^2 \neq 1$, since $A_n^{(F)} \propto M_F - 1$, only the leading order term for the $n \geq 1$ coefficients in Eq. (3.23) are affected. Substitution of Eqs. (3.17) and (3.19) into (3.9) yields the expression for the dominant term for the scattering amplitudes

$$A_n^{(F)} = i\pi \frac{1-s^{-2}}{n!(n+1)!}\left(\frac{ka}{2}\right)^{2n+2}\left[1+O\left(k_1^2a^2+\kappa^2(ka)\right)\right], \quad n \geq 1. \tag{B.2}$$

For this degenerate case, Eq. (B.2) must be substituted for Eq. (3.23) for an accurate solution. Now, the respective orders of magnitude of the first three coefficients with respect to *ka* are $A_0^{(F)} = O\left(k^2a^2\right)$, $A_1^{(F)} = O\left(k^4a^4\right)$, and $A_2^{(F)} = O\left(k^6a^6\right)$. Thus, like the previous case, this degenerate case also does not change the overall order of magnitude with respect to *ka* for the amplitude of the scattered field. Unlike before, now the $A_0^{(F)}$ term will be the sole dominant term for the scattered field. In the Rayleigh regime, matched densities between two fluids causes a fluid target to have the directivity of that due to a monopole source. The small fluid sphere exhibited similar results through inspection of Eqs. 27, 29, and 30 in [33]. And, as in the previous degenerate case, the magnitude of the scattering amplitude for the fluid sphere and cylinder is proportional to k^3a^3 and k^2a^2, respectively. As previously noted, Eq. (B.2) differs by a constant factor of ½ from the equation for Z_n on p. 573 in [52].

B. SOLID CYLINDER

In the degenerate case when $M_{ES}\left(s_1^2 - s_2^2\right) = 1$ and $M_{ES} \neq 1$, since $A_0^{(ES)} \propto M_{ES}\left(s_1^2 - s_2^2\right) - 1$, only the leading order term for the $n = 0$ coefficients shown in Eqs. (3.24) and (3.26) are affected. The expression for the leading order term for the scattering amplitude, under condition (3.15), with substitution of Eqs. (3.16) and (3.18) into (3.13), becomes

$$A_0^{(ES)} = -\frac{i\pi}{2}\left(M_{ES} - 1\right)\left(\frac{ka}{2}\right)^4 \left[1 - i\pi\frac{k^2a^2}{4}\left(1 + \frac{2i}{\pi}\left(\ln\left(\frac{ka}{2}\right) + \gamma\right)\right)\right]^{-1} \times \left[1 + O\left(k_1^2a^2 + \kappa^2\left(ka\right)\right)\right]. \tag{B.3}$$

For this degenerate case, Eq. (B.3) must be replaced with for Eqs. (3.24) and (3.26) for an accurate solution. Now, the respective orders of magnitude of the first three coefficients with respect to *ka* are $A_0^{(ES)}, A_2^{(ES)} = O\left(k^4a^4\right)$ and $A_1^{(ES)} = O\left(k^2a^2\right)$. As a result, the findings are completely analogous to the fluid cylinder in the degenerate case when $M_F s^2 = 1$ and $M_F \neq 1$, and so are not reproduced here.

In the degenerate case when $M_{ES} = 1$ and $M_{ES}\left(s_1^2 - s_2^2\right) \neq 1$, since

$A_1^{(ES)} \propto M_{ES} - 1$, only the leading order term for the $n = 1$ coefficient in Eqs. (3.27) and (3.29) are affected, unlike for the fluid. Substitution of Eqs. (3.17) and (3.19) into (3.13) yields the expression for the dominant term for the scattering amplitude

$$A_1^{(ES)} = i\pi\frac{1 - \left(s_1^2 - s_2^2\right)^{-1}}{2}\left(\frac{ka}{2}\right)^4 \left[1 + O\left(\left(k_1^2 + k_2^2\right)a^2 + \kappa^2\left(ka\right)\right)\right]. \tag{B.4}$$

For this degenerate case, Eq. (B.4) must be replaced for Eqs. (3.27) and (3.29) for an accurate solution. Now, the respective orders of magnitude of the first three coefficients with respect to *ka* are $A_0^{(ES)} = O\left(k^2a^2\right)$ and $A_1^{(ES)}, A_2^{(ES)} = O\left(k^4a^4\right)$. As a result, the findings are completely analogous to the fluid cylinder in the degenerate case when $M_F = 1$, and $M_F s^2 \neq 1$, and so are not reproduced here.

THIS PAGE INTENTIONALLY LEFT BLANK

APPENDIX C. IMPROVED UNIFORM ASYMPTOTICS FOR SOFT AND HARD CYLINDERS

In [1], we derived a uniform asymptotic solution $\tilde{P}$ for the scattered field for soft, hard, and impedance targets,

$$\begin{aligned}
\tilde{P} &= \tilde{B}_0 H_0^{(1)}(kr) + \tilde{B}_1 H_0^{(1)}\left(kR\left(a^2/b\right)\right) + \tilde{B}_2 H_0^{(1)}\left(kR\left(-a^2/2b\right)\right), \\
\tilde{B}_0 &= -A_0 H_0^{(1)}(kb) - \tilde{B}_1 J_0\left(ka^2/b\right) - \tilde{B}_2 J_0\left(ka^2/2b\right), \\
\tilde{B}_1 &= -\frac{A_1 H_1^{(1)}(kb) J_2\left(ka^2/2b\right) + A_2 H_2^{(1)}(kb) J_1\left(ka^2/2b\right)}{J_1\left(ka^2/b\right) J_2\left(ka^2/2b\right) + J_2\left(ka^2/b\right) J_1\left(ka^2/2b\right)}, \\
\tilde{B}_2 &= \frac{A_1 H_1^{(1)}(kb) J_2\left(ka^2/b\right) - A_2 H_2^{(1)}(kb) J_1\left(ka^2/b\right)}{J_1\left(ka^2/2b\right) J_2\left(ka^2/b\right) + J_2\left(ka^2/2b\right) J_1\left(ka^2/b\right)}.
\end{aligned} \tag{B.5}$$

The scattered wave is expressed as the field generated by the sum of fields due to three image line sources located at $(0,0)$, $\left(a^2/b,0\right)$, and $\left(-a^2/2b,0\right)$. The latter source was understood not to be unique but was necessary in the solution to provide second-order accuracy over the entire domain with respect to the dimensionless radius *ka*.

In Chapter III, we developed a uniform asymptotic solution *P* (3.41) for fluid and solid targets. The scattered wave is expressed as the field generated by the sum of three image sources, a line and a dipole source collocated at the point $(0,0)$ and a line source located at $\left(a^2/b,0\right)$. The solution *P* (3.41) contains similar structure to the previous results $\tilde{P}$, and, under condition (3.31), it also contains the soft, hard, and impedance structure for the image sources in the inner solutions.

The new asymptotic solutions are of the same order of accuracy as the previous result with respect to *ka*. However, *P* offers the advantage of a single general expression for all target types considered. And, importantly, it proved to be more accurate than those previously derived in [1] for soft, hard, and impedance targets. Numerical accuracy of the new uniform asymptotic solution of the scattered field due to soft and hard targets for exact A_n scattering amplitudes compared to the previous results from [1] is presented in Figure 26 and Figure 27, respectively. For the soft target significant increase in accuracy is achieved

especially for $\alpha = O(1)$, as seen by the shifting downward of the respective curves in Figure 26. For the hard target case, significant increase in accuracy is achieved for a broad range of α values, as seen by the shifting downward of all the curves in Figure 27.

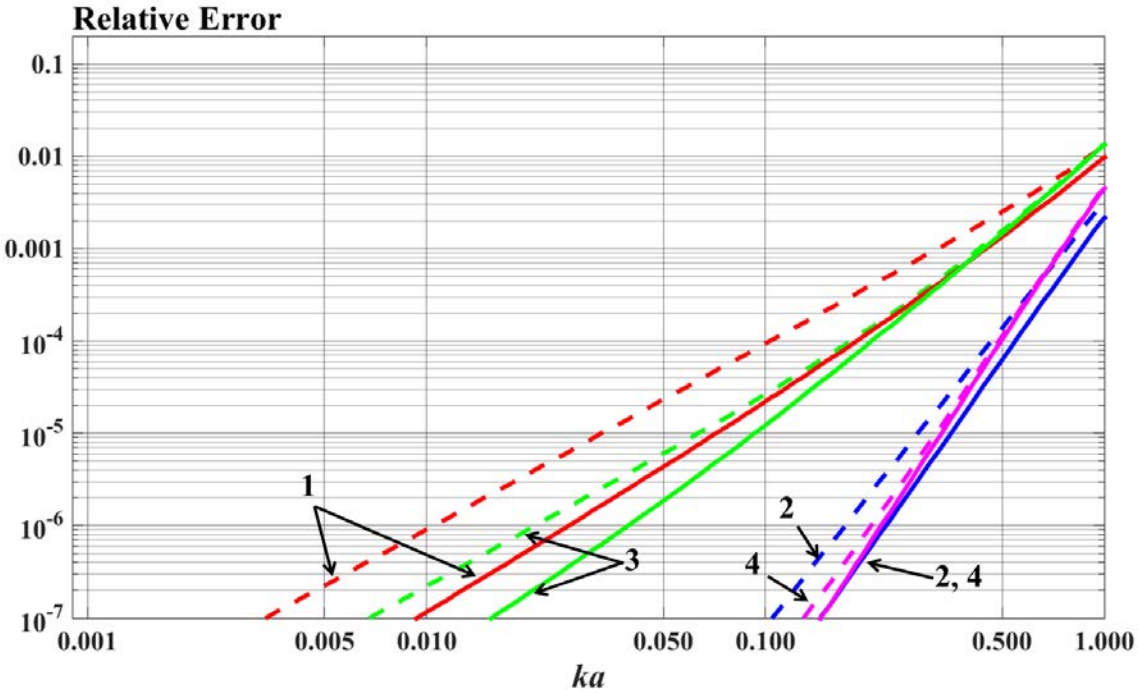

Figure 26. Improved accuracy of the uniform asymptotic solution for the scattered field due to soft cylinder. Relative error between the uniform asymptotic solutions and the exact scattered field is plotted as a function of *ka* for $\tilde{P}$ (dashed lines) and P (solid lines). The relative error is shown for the angle $\theta = \pi/4$ and the following sets of geometric parameters: $b = r = 1.5a$ (1), $b = 1.5a$, $r = 10^3 a$ (2), $b = 10a$, $r = 1.5a$ (3), and $b = 10a$, $r = 10^3 a$ (4).

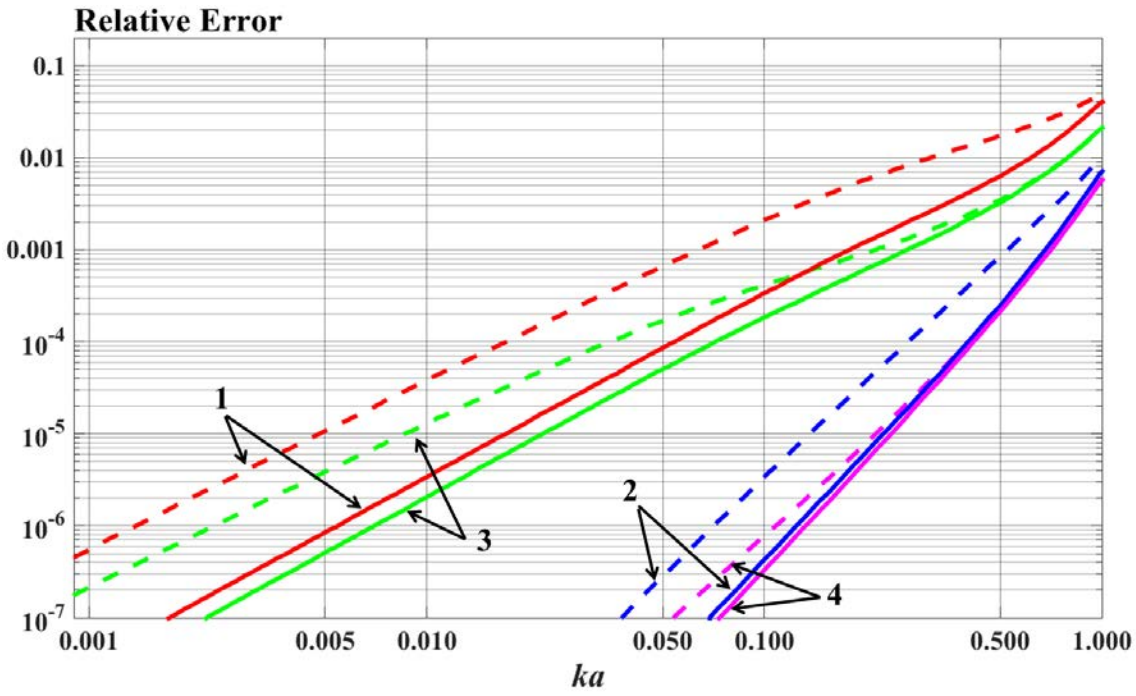

Figure 27. Improved accuracy of the uniform asymptotic solution for the scattered field due to hard cylinder. Relative error between the uniform asymptotic solutions and the exact scattered field is plotted as a function of ka for $\tilde{P}$ (dashed lines) and P (solid lines). The relative error is shown for the angle $\theta = \pi/4$ and the following sets of geometric parameters: $b = r = 1.5a$ (1), $b = 1.5a$, $r = 10^3 a$ (2), $b = 10a$, $r = 1.5a$ (3), and $b = 10a$, $r = 10^3 a$ (4).

THIS PAGE INTENTIONALLY LEFT BLANK

LIST OF REFERENCES

[1] A. B. Baynes and O.A. Godin, “Rayleigh scattering of a cylindrical sound wave by an infinite cylinder,” *J. Acoust. Soc. Am.*, vol. 142, no. 6, pp. 3613–3623, December 2017.

[2] O. A. Godin and A. B. Baynes, “Passive, broadband suppression of radiation of low-frequency sound,” *J. Acoust. Soc. Am.*, vol. 143, no. 2, pp. EL67–EL73, February 2018.

[3] A. B. Baynes and O. A. Godin, Scattering of low frequency sound by fluid and solid cylinders, *J. Sound Vib.* (Under review, 2018).

[4] A. B. Baynes and O.A. Godin, “Rayleigh scattering of a cylindrical sound wave by an infinite cylinder,” *J. Acoust. Soc. Am.*, vol. 141, no. 5, pp. 4047–4047, May 2017.

[5] A. B. Baynes and O.A. Godin, “Scattering of low-frequency sound by infinite fluid and solid cylinders,” *J. Acoust. Soc. Am.*, vol. 143, no. 3, pp. 1874–1874, March 2018.

[6] A. B. Baynes and O.A. Godin, “Scattering of low-frequency sound by shallow underwater targets,” *J. Acoust. Soc. Am.*, vol. 143, no. 3, pp. 1874–1874, March 2018.

[7] J. W. Strutt (Lord Rayleigh), “XXXIV. On the transmission of light through an atmosphere containing small particles in suspension, and on the origin of the blue of the sky,” *Philos. Mag.*, vol. 47, no. 287, pp. 375–384, 1899.

[8] J. E. Gubernatis and E. Domany, “Rayleigh scattering of elastic waves from cracks,” *J. Appl. Phys.*, vol. 50, no. 2, pp. 818–824, February 1979.

[9] A. T. Young, “Rayleigh scattering,” *App. Opt.*, vol. 20, no. 4, pp. 533–535, February 1981.

[10] J. W. Strutt (Lord Rayleigh), *Theory of Sound*. New York, NY, USA: Dover, 1945.

[11] J. W. Strutt (Lord Rayleigh), “V. On the incidence of aerial and electric waves upon small obstacles in the form of ellipsoids or elliptic cylinders, and on the passage of electric waves through a circular aperture in a conducting screen,” *Philos. Mag.*, vol. 44, no. 266, pp. 28–52, 1897.

[12] J. W. Strutt (Lord Rayleigh), “XXX. On the light dispersed from fine lines ruled upon reflecting surfaces or transmitted by very narrow slits,” *Philos. Mag.*, vol. 14, no. 81, pp. 350–359, 1907.

[13] J. J. Thomson, *Notes on Recent Researches in Electricity and Magnetism*. Oxford, UK: Clarendon Press, 1893.

[14] J. S. Asvestas, *Electromagnetic and Acoustic Scattering by Simple Shapes*, J. J. Bowman, T. B. A. Senior, and P. L. E. Uslenghi, Eds. New York, NY, USA: Wiley, 1969.

[15] R. H. Hackman and G. S. Sammelmann, "Multiple-scattering analysis for a target in an oceanic waveguide," *J. Acoust. Soc. Am.*, vol. 84, no. 5, pp. 1813–1825, November 1988.

[16] P. Gabrielli and M. Mercier-Finidori, "Acoustic scattering by two spheres: multiple scattering and symmetry considerations," *J. Sound Vib.*, vol. 241, no. 3, pp. 423–439, March 2001.

[17] G. C. Gaunaurd and H. Huang, "Acoustic scattering by a spherical body near a plane boundary," *J. Acoust. Soc. Am.*, vol. 96, no. 4, pp. 2526–2536, October 1994.

[18] G. C. Gaunaurd, H. Huang, and H. C. Strifors, "Acoustic scattering by a pair of spheres," *J. Acoust. Soc. Am.*, vol. 98, no. 1, pp. 495–507, July 1995.

[19] J. A. Fawcett, "Scattering from a finite cylinder near an interface," *J. Acoust. Soc. Am.*, vol. 136, no. 2, pp. 485–493, August 2014.

[20] M. Zampolli, A. Tesei, F. B. Jensen, N. Malm, and J. B. Blottman III, "A computationally efficient finite element model with perfectly matched layers applied to scattering from axially symmetric objects," *J. Acoust. Soc. Am.*, vol. 122, no. 3, pp. 1472–1485, September 2007.

[21] K. L. Williams, S. G. Kargl, E. Thorsos, D. Burnett, J. Lopes, M. Zampolli, and P. Marston, "Acoustic scattering from a solid aluminum cylinder in contact with a sand sediment: Measurements, modeling, and interpretation," *J. Acoust. Soc. Am.*, vol. 127, no. 6, pp. 3356–3371, June 2010.

[22] J. A. Fawcett, W. L. J. Fox, and A. Maguer, "Modeling of scattering by objects on the seabed," *J. Acoust. Soc. Am.*, vol. 104, no. 6, pp. 3296–3304, December 1998.

[23] J. M. Jech, J. K. Horne, D. Chu, D. A. Demer, D. T. Francis, N. Gorska, B. Jones, A. C. Lavery, T. K. Stanton, G. J. Macaulay, D. B. Reeder, and K. Sawada, "Comparisons among ten models of acoustic backscattering used in aquatic ecosystem research," *J. Acoust. Soc. Am.*, vol. 138, no. 6, pp. 3742–3764, December 2015.

[24] G. C. Eastland and P. L. Marston, "Enhanced backscattering in water by partially exposed cylinders at free surfaces associated with an acoustic Franz wave," *J. Acoust. Soc. Am.*, vol. 135, no. 5, pp. 2489–2492, May 2014.

[25] W. K. Lui and K. M. Li, “The scattering of sound by a long cylinder above an impedance boundary,” *J. Acoust. Soc. Am.*, vol. 127, no. 2, pp. 664–674, February 2010.

[26] K. L. Williams, S. G. Kargl, E. I. Thorsos, D. S. Burnett, J. L. Lopes, M. Zampolli, and P. L. Marston, “Acoustic scattering from an aluminum cylinder in contact with a sand sediment: Measurements, modeling, and interpretation,” *J. Acoust. Soc. Am.*, vol. 127, no. 6, pp. 3356–3371, June 2010.

[27] M. Zampolli, A. Tesei, G. Canepa, and O. A. Godin, “Computing the far field scattered or radiated by objects inside layered fluid media using approximate Green’s functions,” *J. Acoust. Soc. Am.*, vol. 123, no. 6, pp. 4051–4058, June 2008.

[28] A. Lowan, P. Morse, H. Feshbach, and M. Lax, “Scattering and radiation from circular cylinders and spheres, tables of amplitudes and phase angles,” Mathematical Tables Project (U.S.), U.S. Navy Dept., Arlington, VA, USA, 1946.

[29] J. J. Faran, “Sound scattering by solid cylinders and spheres,” *J. Acoust. Soc. Am.*, vol. 23, no. 4, pp. 405–418, July 1951.

[30] P. M. Morse, *Vibration and Sound*, vol. II, MacMillan, London, 1948.

[31] J. W. Strutt (Lord Rayleigh), “Investigation of the disturbance produced by a spherical obstacle on the waves of sound,” *Proc. London Math. Soc.*, vol. 4, no. 1, pp. 253–283, November 1871.

[32] O. A. Godin, “Scattering of a spherical wave by a small sphere: An elementary solution,” *J. Acoust. Soc. Am.*, vol. 130, no. 4, pp. EL135–EL141, October 2011.

[33] O. A. Godin, “Rayleigh scattering of a spherical sound wave,” *J. Acoust. Soc. Am.*, vol. 133, no. 2, pp. 709–720, February 2013.

[34] W. Thomson (Lord Kelvin), *Papers on Electrostatics and Magnetism*, 2nd ed. London, UK: MacMillan, 1884.

[35] J. Vanderlinde, *Classical Electromagnetic Theory*, 2nd ed. Dordrecht, Netherlands: Kluwer Academic Publishers, 2004.

[36] Q. G. Lin, “Theoretical development of the image method for a general magnetic source in the presence of a superconducting sphere or a long superconducting cylinder,” *Phys. Rev. B.*, vol. 74, no. 2, pp. 024510-1–024510-12, July 2006.

[37] A. Coatanhay and J. M. Conoir, “Scattering near a plane interface using a generalized method of images approach,” *J. Comput. Acoust.*, vol. 12, no. 2, pp. 233–256, 2004.

[38] A. M. Gunderson, A. L. España, P. L. Marston, “Spectral analysis of bistatic scattering from underwater elastic cylinders and spheres,” *J. Acoust. Soc. Am.*, vol. 142, no. 1, pp. 110–115, July 2017.

[39] E. Ogam, Z. E. A Fellah, and P. Baki, “The inverse problem of acoustic wave scattering by an air-saturated poroelastic cylinder,” *J. Acoust. Soc. Am.*, vol. 133, no. 3, pp. 1443–1457, March 2013.

[40] A. L. España, K. L. Williams, D. S. Plotnick, and P. L. Marston, “Acoustic scattering from a water-filled cylindrical shell: Measurements, modeling, and interpretation,” *J. Acoust. Soc. Am.*, vol. 136, no. 1, pp. 109–121, July 2014.

[41] C. Feuillade, “Superspheroidal modeling of resonance scattering from elongated air bubbles and fish swim bladders,” *J. Acoust. Soc. Am.*, vol. 131, no. 1, pp. 146–155, January 2012.

[42] E. M. Fischell and H. Schmidt, “Classification of underwater targets from autonomous underwater vehicle sampled bistatic acoustic scattered fields,” *J. Acoust. Soc. Am.*, vol. 138, no. 6, pp. 3773–3784, December 2015.

[43] K. G. Sabra, S. Conti, P. Roux, T. Akal, W. A. Kurperman, J. M. Stevenson, A. Tesei, and P. Guerrini, “Experimental demonstration of a high-frequency forward scattering acoustic barrier in a dynamic coastal environment,” *J. Acoust. Soc. Am.*, vol. 127, no. 6, pp. 3430–3439, June 2010.

[44] D. Chu, G. L. Lawson, and P. H. Wiebe, “Estimation of biological parameters of marine organisms using linear and nonlinear acoustic scattering model-based inversion methods,” *J. Acoust. Soc. Am.*, vol. 139, no. 5, pp. 2885–2895, May 2016.

[45] P. A. Lepper and G. L. D’spain, “Measurement and modeling of the acoustic field near an underwater vehicle and implications for acoustic source localization,” *J. Acoust. Soc. Am.*, vol. 122, no. 2, pp. 892–905, August 2007.

[46] C. Cho, W. Yang, S. Lee, and J. Park, “Flexural wave cloaking via embedded cylinders with systematically varying thicknesses,” *J. Acoust. Soc. Am.*, vol. 139, no. 6, pp. 3320–3324, June 2016.

[47] J. E. Boisvert, C. L. Scandrett, and T. R. Howarth, “Scattering reduction of an acoustically hard cylinder covered with layered pentamode metamaterials,” *J. Acoust. Soc. Am.*, vol. 139, no. 6, pp. 3404–3411, June 2016.

[48] L. M. Brekhovskikh and O. A. Godin, *Acoustics of Layered Medium. 2: Point Sources and Bounded Beams*, 2nd ed. Berlin, Germany: Springer, 1999.

[49] M. Abramovitz and I. A. Stegun, Eds. *Handbook of Mathematical Functions with Formulas, Graphs, and Tables* (Applied Mathematics Series 55). New York, NY, USA: Dover Publications, 1972.

[50] R. Fitzpatrick, "Two-dimensional potential flow," Fluid Mechanics, March 31, 2016. [Online]. Available: http://http://farside.ph.utexas.edu/teaching/336L/Fluidhtml/Fluidhtml.html

[51] M. A. Moline, S. M. Blackwell, C. V. Alt, B. Allen, T. Austin, J. Case, N. Forrester, R. Goldsborough, M. Purcell, and R. Stokey, "Remote environmental monitoring units: An autonomous vehicle for characterizing coastal environments," *J. Atmos. Oceanic Technol.*, vol. 22, no. 11, pp. 1797–1808, November 2005.

[52] P. A. Martin, A. Maurel, and W. J. Parnell, "Estimating the dynamic effective mass density of random composites," *J. Acoust. Soc. Am.*, vol. 128, no. 2, pp. 571–577, August 2010.

[53] C. Boutin, "Rayleigh scattering of acoustic waves in rigid porous media," *J. Acous. Soc. Am.*, vol. 122, no. 4, pp. 1888–1905, October 2007.

[54] F. J. Sabina and V. M. Babich, "Low-frequency scattering of acoustic waves by a bounded rough surface in a half-plane," *J. Acoust. Soc. Am.*, vol. 109, no. 3, pp. 878–885, March 2001.

[55] D. R. Palmer, "Rayleigh scattering from nonspherical particles," *J. Acoust. Soc. Am.*, vol. 99, no. 4, pp. 1901–1912, April 1996.

[56] R. A. Roy, W. Carey, M. Nicholas, J. Schindall, and L. A. Crum, "Low-frequency scattering from submerged bubble clouds," *J. Acoust. Soc. Am.*, vol. 92, no. 5, pp. 2993–2996, November 1992.

[57] C. Feuillade, R. W. Nero, and R. H. Love, "Modeling low frequency scattering from small schools of fish," *J. Acoust. Soc. Am.*, vol. 97, no.5, pp. 3423, May 1995.

[58] W. R. Smythe, *Static and Dynamic Electricity*, 3rd ed. New York, NY, USA: McGraw-Hill, 1968.

[59] I. V. Lindell and K. I. Nikoskinen, "Two-dimensional image method for time-harmonic line current in front of a PEC cylinder," *Microwave Optical Techn. Lett.*, vol. 21, no. 3, pp. 217–222, May 1999.

[60] I. V. Lindell and K. I. Nikoskinen, "Two-dimensional image method for time-harmonic line current in front of a material cylinder," *Electrical Engineering*, vol. 81, no. 6, pp. 357–362, April 1999.

[61] L. M. Brekhovskikh and O. A. Godin, *Acoustics of Layered Medium I: Plane and Quasi-Plane Waves*, 2nd ed. New York, NY, USA: Springer, 1998.

[62] A. E. H. Love, *A Treatise on the Mathematical Theory of Elasticity*, 4th ed. New York, NY, USA: Dover, 1944.

[63] O. A. Godin, "Rayleigh scattering of sound by spherically symmetric bodies," in *Proc. Mtgs. Acoust.*, vol. 19, no. 1, June 2013. [Online]. doi:10.1121/1.4799769

[64] O. A. Godin, "Wave refraction at an interface: Snell's law versus Chapman's law," *J. Acoust. Soc. Am.*, vol. 125, no. 4, pp. EL117–EL122, April 2009.

[65] W. J. Richardson, C. R. Greene, Jr., C. I. Malme, and D. H. Thomson, *Marine Mammals and Noise*. San Diego, CA, USA: Academic Press, 2013.

[66] A. N. Popper, "Effects of anthropogenic sounds on fishes," *Fisheries*, vol. 28, no. 10, pp. 24–31, October 2003.

[67] N. D. Merchant, M. J. Witt, P. Blondel, B. J. Godley, and G. H. Smith, "Assessing sound exposure from shipping in coastal waters using a single hydrophone and Automatic Identification System (AIS) data," *Marine Pollution Bulletin*, vol. 64, no. 7, pp. 1320–1329, July 2012.

[68] G. Frisk, "Noiseonomics: The relationship between ambient noise levels in the sea and global economic trends," *Scientific Reports*, vol. 2, no. 437, 2012. [Online]. doi:10.1038/srep00437

[69] M. J. Khan, G. Bhuyan, M. T. Iqbal, and J. E. Quaicoe "Hydrokinetic energy conversion systems and assessment of horizontal and vertical axis turbines for river and tidal applications: A technology status review," *Appl. Energy*, vol. 86, no. 10, pp. 1823–1835, October 2009.

[70] B. Würsig, C. R. Greene, Jr., and T. A. Jefferson, "Development of an air bubble curtain to reduce underwater noise of percussive piling," *Mar. Environ. Res.*, vol. 49, no. 1, pp. 79–93, February 2000.

[71] P. H. Dahl and D. R. Dall'Osto, "On the underwater sound field from impact pile driving: Arrival structure, precursor arrivals, and energy streamlines," *J. Acoust. Soc. Am.*, vol. 142, no. 2, pp. 1141–1155, August 2017.

[72] K. Lucke, P. A. Lepper, M.-A. Blanchet, and U. Siebert, "The use of an air bubble curtain to reduce the received sound levels for harbor porpoises (Phocoena phocoena)," *J. Acoust. Soc. Am.*, vol. 130, no. 5, pp. 3406–3412, November 2011.

[73] K. M. Lee, K. T. Hinojosa, M. S. Wochner, T. F. Argo, P. S. Wilson, and R. S. Mercier, “Sound propagation in water containing large tethered spherical encapsulated gas bubbles with resonance frequencies in the 50 Hz to 100 Hz range,” *J. Acoust. Soc. Am.*, vol. 130, no. 5, pp. 3325–3332, November 2011.

[74] K. M. Lee, P. S. Wilson, and M. S. Wochner, “Attenuation of standing waves in a large water tank using arrays of large tethered encapsulated bubbles,” *J. Acoust. Soc. Am.*, vol. 135, no. 4, pp. 1700–1708, April 2014.

[75] O. A. Godin, “Anomalous transparency of water-air interface for low-frequency sound,” *Phys. Rev. Lett*, vol. 97, no. 16, pp. 164301, October 2006.

[76] O. A. Godin, “Transmission of low-frequency sound through the water-to-air interface,” *Acoust. Phys.*, vol. 53, no. 3, pp. 305–312, May 2007.

[77] D. C. Calvo, M. Nicholas, and G. J. Orris, “Experimental verification of enhanced sound transmission from water to air at low frequencies,” *J. Acoust. Soc. Am.*, vol. 134, no. 5, pp. 3403–3408, November 2013.

[78] J. H. Lee, K. J. Lee, J. H. Kim, and B. K. Kim, “Sea-trial verification of air-filled rubber membrane for mitigation of propeller cavitation induced hull excitation,” *Ocean Engineering*, vol. 110, pp. 314–324, December 2015.

[79] M. F. Ashby and T. Lu, “Metal foams: A survey,” *Sc. China Ser. B-Chem.*, vol. 46, no. 6, pp. 521–532, December 2003.

[80] R. J. Barton, K. B. Smith, and H. T. Vincent, “Characterization of scattered acoustic intensity fields in the resonance region of a motionless rigid sphere,” *J. Acoust. Soc. Am.*, vol. 127, no. 6, pp. EL240-EL245, June 2010.

[81] R. J. Barton, K. B. Smith, and H. T. Vincent, “A characterization of the scattered acoustic intensity field in the resonance rigion for simple spheres,” *J. Acoust. Soc. Am.*, vol. 129, no. 5, pp. 2772-2784, May 2011.

[82] R. J. Barton, G. R. Moss, and K. B. Smith, “Characterization of scattered acoustic intensity fields of finite cylinders in the resonance region,” *J. Acoust. Soc. Am.*, vol. 130, no. 4, pp. 2332-2332, April 2011.

[83] R. J. Barton and K. B. Smith, “A characterization of scattered acoustic intesity fields in the resonance region,” *J. Acoust. Soc. Am.*, vol. 127, no. 3, p. 1857, March 2010.

[84] R. J. Barton and K. B. Smith, “Characterization of the near scattered acoustic vector field,” *J. Acoust. Soc. Am.*, vol. 124, no. 4, pp. 2583–2583, October 2008.

[85] R. J. Barton and K. B. Smith, “Characterization of the near scattered acoustic vector field,” *J. Acoust. Soc. Am.*, vol. 123, no. 5, pp. 3439–3439, May 2008.

[86] R. J. Barton, G. R. Moss, B. K. Amaral, G. Dossot, and K. B. Smith, “Underwater techniques to characterize the near scattered acoustic vector field,” *J. Acoust. Soc. Am.*, vol. 135, no. 4, pp. 2362–2362, April 2014.

INITIAL DISTRIBUTION LIST

1. Defense Technical Information Center
   Ft. Belvoir, Virginia

2. Dudley Knox Library
   Naval Postgraduate School
   Monterey, California